Landslide Legacies:
The cascading impacts of landslides on hazards and landscape evolution

Paul Monroe Morgan

A dissertation

submitted in partial fulfillment of the

requirements for the degree of

Doctor of Philosophy

University of Washington

2026

Reading Committee:

Alison R. Duvall, Chair

alex r.r. grant

David R. Montgomery

Program Authorized to Offer Degree:

Earth and Space Sciences

University of Washington

Abstract

Landslide Legacies:

The cascading impacts of landslides on hazards and landscape evolution

Paul Monroe Morgan

Chair of the Supervisory Committee:
Alison R. Duvall
Earth and Space Science

In this dissertation I explore the cascading impacts of landslides on both hazards and landscape evolution. For hazards, one of the worst case impacts of a landslide is that it dams a river and leads to a catastrophic outburst flood. In Chapter 1, I develop a new method for estimating where this may occur, called the damability function, validate it in the Oregon Coast Range, and generate the first landslide dam hazard assessment for anywhere in the United States. I find that high landslide dam susceptibility is widespread, so this hazard should be considered in the Pacific Northwest. I also find that in only a handful of large rivers would landslide dams possibly

lead to large catastrophic floods. For landscape evolution, landslides work in tandem with downhill soil creep to move sediment from hillslope to rivers as part of the geomorphic landscape system, but when and how shallow landslides fit into this system remain unclear, despite their abundance. In Chapter 2, I develop a new model to simulate shallow landslides that only displace the surface soil layer, called SoilLandslider, that is capable of running in simulations that are long enough for landscapes to reach steady-state. In Chapter 3, I add the SoilLandslider module to sets of numerical experiments that explore what landscape conditions favor persistent shallow landsliding. I find that at low slopes the amount of shallow landsliding is limited by the slope, and the emergent slope angles of the model are set by the ratio between uplift and erosional efficiency of soil creep and fluvial erosion. For models with high slopes landslide erosion is limited by the soil depth, and soil depth is determined by the ratio between uplift and soil production. The ratio between uplift and soil production determines whether a landscape is in a slope-limited landslide domain, or a soil-limited landslide domain. Through landscape evolution modelling I further establish the importance of soil landsliding to landscape evolution, and the importance of soil depth on moderating soil mantled landscapes.

TABLE OF CONTENTS

0. **INTRODUCTION**

Landslides are among the most dramatic processes that shape the surface of the earth. During a landslide, thousands to tens of millions of cubic meters of rock and soil can crash down mountainsides at speeds of 60 kilometers per hour or more. This catastrophic movement can destroy roads, buildings, and kill those people unfortunate enough to be in the wrong place at the wrong time. Appropriately, most research into landslides has focused on identifying those "wrong places", through susceptibility analyses, and defining when it is the "wrong time", through precipitation or seismic trigger analyses. However, a landslide doesn't just disappear once it has failed and slid down the mountain; rather, this marks the starting point for a whole set of cascading impacts. In this dissertation, I explore what happens next: *what are the landslide legacies?*

In Chapter 1, I explore the cascading hazards triggered by landslides on short timescales (days to months). Specifically, I address the worst-case cascading impact from landslides: a catastrophic outburst flood from a landslide-dammed lake. I develop a probabilistic framework to assess landslide dam susceptibility at regional scales. In Chapters 2 and 3, I explore how landslides shape landscape evolution on longer timescales (thousands to millions of years). In **Chapter 2,** I develop SoilLandslider, a model simulating discrete soil landslide events at geomorphic timescales. In **Chapter 3,** I employ this model to explore the landscape conditions where landsliding occurs, and the limits of shallow landslide erosion. I reveal the relationships and feedback between soil production, uplift, diffusion, soil depth, and landscape slopes.

0.1 Landslide dam hazards

Landslide dams create an impounded lake that may submerge upstream roads or buildings. However, the larger danger lies in the possibility that the lake can break through or overtop the dam in a sudden outburst, draining rapidly and possibly catastrophically. Catastrophic outburst floods have caused extensive destruction and death; the deadliest outburst floods caused thousands of fatalities (Costa & Schuster, 1991; Dai et al., 2021; Zeng et al., 2022).

Dozens of historically recorded landslide dams have occurred in the US alone. The landslide failures have had a variety of triggers, including: (1) lone events not triggered by extreme rainfall or earthquakes, such as the Gros Ventre landslide flood, which killed 6 people (Costa & Schuster, 1988), (2) Extreme precipitation events such as recorded in the Oregon coast and Sierras (Struble et al., 2020; Wieczorek, 2002), and (3) Earthquakes, such as the 1952 Mw 7.2 Hebgen Lake earthquake (created Quake Lake), the 1989 Mw 6.9 Loma Prieta earthquake (5 landslide dams with 2 removed by engineers (Keefer, D.K., Manson, 1998), and the 2001 Mw 6.8 Nisqually earthquake (Cedar River landslide, which required excavation). Considering this clear history of past landslide dams, we should expect and prepare for landslides to dam rivers in the future, especially as part of the hazard cascade from future large earthquakes and ever-increasing extreme precipitation events.

Timely information can help government agencies respond and ideally prevent landslide dams from turning into humanitarian disasters. Evacuation orders can get people out of the flood path before the dam overtops; for example, during the Tangjiashan emergency in China 2008, over 250,000 people were evacuated before the dam breach (Cui et al., 2012), and during the recent 2024 Chilcotin, British Columbia landslide dam, an evacuation order covered 73 km^2. Perhaps more important than evacuation, engineers can excavate a spillway into the landslide dam, both decreasing the volume of the dammed lake, and stabilizing the spillway to prevent runaway erosion and lake outburst. This was the case at Quake Lake, Montana, where the Army Corps of Engineers excavated a spillway in weeks. It is imperative that landslide dams be found quickly post-event to expedite response, because landslide dam lakes are often short-lived, with 50% failing in 10 days or less (Costa & Schuster, 1988).

Despite the possible severe consequences and the necessity for swift response and to the best of my knowledge, prior to this dissertation work there was no published landslide dam formation susceptibility map for anywhere in the US. Landslide dam susceptibility maps can direct outreach, help government agencies with regional hazard planning, and, in the case of a widespread landslide event, guide the search for new dams that might require immediate attention.

In Chapter 1, I present a simple probabilistic approach to estimating landslide dam susceptibility from mapped landslide data and digital elevation models. I demonstrate the utility of this framework for estimating landslide dam susceptibility in the Oregon Coast Range (OCR), a region with extensive mapped landslide inventories, mapped landslide dam deposits and high hazard from atmospheric rivers and Cascadia earthquakes (Burns and Madin, 2009; Struble et al., 2020; Dettinger et al., 2018; Grant et al., 2022). To make landslide dam susceptibility estimations for the OCR, I built a new workflow, integrating disparate datasets into a single dam susceptibility value. I made a new algorithm to automate valley width measurements. To estimate landslide volumes I use a large database of mapped landslide deposits within the study area to fit a single empirical log-normal distribution of landslide volumes to use across the study area. I also explored the utility of location-specific landslide volume estimates using multivariate regression, however, was unable to make satisfactory predictions.

I found that approximately one-third of the rivers in the OCR could be dammed by the average landslide. High damability values correlate with river headwaters, high relief terrain, and more resistant lithologies. Fortunately, most river stretches with the highest potential for landslide dam formation may only impound relatively small lakes. However, a subset of the river sections could impound lakes of sufficient size to generate catastrophic outburst floods, which we highlight in our findings. These findings demonstrate that landslide dam hazards are regionally significant and warrant further assessment and preparations.

0.2 Landslides and landscape evolution

Landscape evolution models (LEMs) are numerical tools for studying the processes that shape landscapes and how these processes interact with each other over different temporal scales

(Campforts et al., 2020; Dietrich et al., 2003; Tucker and Hancock, 2010). Field studies have identified and calibrated several geomorphic transport functions inferred to govern how landscapes (especially soil-mantled landscapes) erode and transport material. However, the relationships, feedbacks, and limits on these processes are difficult to conceptualize on a real-world, three-dimensional landscape. This makes it difficult to generate mental models with which to draw hypotheses for further field testing to deepen our understanding of geomorphic processes. Numerical landscape evolution models allow the researcher to put together our theoretical understanding of geomorphic processes in order to explore how they may work together. In this way, I view landscape evolution models as a tool for hypothesis generation. By combining geomorphic transport functions, I can explore their numerical inevitabilities and implications for natural landscapes. These modelling results generate hypotheses about landscape evolution, that can be tested against field observations, used to identify limitations in existing transport functions, or motivate refinement of the process functions themselves.

Given their outsize role in mountainous landscape evolution, equations that simulate landslides should be included in LEMs. In practice, only a few models explicitly include landslides (Campforts et al., 2020; Claessens et al., 2007; Densmore et al., 1998; Istanbulluoglu and Bras, 2005; Keck, 2023; Tucker and Bras, 1998). Fewer still focus on shallow landslides (also referred to as ‘soil landslides’), which frequently occur in the Pacific Northwest. Shallow landslides are constrained to the uppermost unconsolidated layer of soil, colluvium, or mobile regolith, and are commonly triggered by rainfall and earthquakes. If we want to hypothesize how changing climate, or past earthquakes might leave their mark on the landscape, shallow landslides are the key link (Stoffel and Huggel, 2012). To investigate possible relationships among climate, earthquakes, soil landslides, and landscape form, we need a model which can be implemented at landscape spatial scales and at the millennial timescales necessary for geomorphic landform evolution to reach topographic steady state. To fill this gap, I developed SoilLandslider, a Landlab module to simulate discrete soil landslides at millennial to million-year timescales.

In Chapter 2, I describe the SoilLandslider module in detail and clarify a set of parameters for the module to function within a landscape evolution model. I validate the model against mapped landslides. I demonstrate the model’s utility and inform its use through numerical experiments. I show that shallow landsliding can generate landscape forms comparable to those produced by non-linear diffusion, suggesting that discrete landslides may be the primary mechanism driving non-linear transport on steep slopes. I also show how hydrologic assumptions affect long-term landscape evolution. The SoilLandslider module enables more process grounded landscape evolution modelling by integrating discrete stochastic events into long timescale simulations, which advances understandings of how driving mechanisms form landscapes.

In Chapter 3, I systematically explore the landscape conditions where soil landsliding is most prominent, and where it is limited. Numerical modelling experiments reveal how uplift, soil production, hillslope diffusion, fluvial erosion, and soil landsliding interact to contribute to steady state landscapes where soil landslide erosion is persistent over millions of years.

My results reveal two domains with different controls on soil landslide erosion: a slope-limited domain and a soil-limited domain. In the slope-limited domain, simulated landscapes are defined by relatively gentle slopes, and thick soil layers. The amount of landslide erosion is limited by the lack of steep slopes where landslides can initiate. In the soil-limited domain, landscapes are defined by steep slopes and minimal to no hillslope soil cover. Here, landsliding is limited by the soil depth.

I introduce two dimensionless parameters to characterize these domains: the slope number (N_{SLP}) which scales with the relationship of uplift with the erosive efficiency of hillslopes and rivers, and the soil number (N_{SD}) which scales with the prediction for steady state soil thickness derived from uplift and soil production. When uplift equals the maximum soil production rate (i.e., $N_{SD}=0$) a soil depth inflection point is reached, defining the transition point between the slope-limited and soil-limited landsliding domains. N_{SD} sets the model domain position, and N_{SLP} sets the magnitude of landslide erosion.

Soil landslides are not possible without sufficient soil depth. I identify the first order importance of soil depth in governing the evolution of soil mantled landscapes. Soil depth modulates our current best estimate geomorphic transport functions defining soil creep, soil production, and soil landsliding. I clarify two key feedbacks related to soil depth: (1) The mean soil depth on hillslope cells is set by the balance between uplift and depth-dependent soil production as defined by the soil number, and (2) soil-depth-driven steepening, where depth-dependent diffusion evolves steeper slopes at low soil depths to maintain steady state soil fluxes. These feedbacks are numerical inevitabilities of the geomorphic transport functions in the models, and match some field observations, but deserve further targeted study within natural landscapes.

I also further confirm the importance of the N_{SD} zero point, a landscape inflection point where uplift exceeds the maximum soil production rate. This point defines the transition between transport-limited and weathering-limited hillslopes (Bierman & Montgomery 2014), which are also referred to as transport-limited and strength-limited hillslopes (Schlunegger, Norton, & Caduff, 2013). Soil landslides are not able to effectively erode weathering- or strength-limited hillslopes because they are supply limited.

1. **Chapter 1**: The damability function: A probabilistic approach to regional landslide dam susceptibility analysis applied to the Oregon Coast Range, US

A version of this paper is published in *Natural Hazards and Earth System Sciences*, and is cited as:
Morgan, P. M., grant, a., Struble, W., LaHusen, S., & Duvall, A. (2026). The damability function: a probabilistic approach to regional landslide dam susceptibility analysis applied to the Oregon Coast Range, USA. *Natural Hazards and Earth System Sciences*, *26*(4), 1745-1766. https://doi.org/10.5194/nhess-26-1745-2026

[Abstract]
Landslides can dam rivers and require rapid response to mitigate catastrophic outburst floods. Here, we present a workflow to map landslide dam formation susceptibility at a regional scale. We define a probabilistic function that combines river valley width and landslide volume to efficiently determine the likelihood of a landslide dam or 'damability'. We combine damability values with landslide susceptibility to estimate landslide dam susceptibility. The valley width measurements are automated using a new elevation threshold-based algorithm. Landslide volume is represented as a statistical distribution from mapped landslides. We validate and apply our approach to the Oregon Coast Range, USA and find that 36% of river stretches exceed a dam potential threshold; these are in river headwaters and steeper terrain, which in this case correlate with more resistant lithologies. We also estimate volumes of the potential dammed lakes and find that most rivers with high dam susceptibility are less likely to impound large lakes because they have low drainage areas. However, widespread susceptibility, and the potential impacts from exceptionally large landslides, suggest that this hazard should be considered in the Pacific Northwest. The damability function workflow can ingest new data and be applied more broadly to assess future landslide dam hazards.

[**Short non-technical summary**]
When landslides dam rivers, the impacts can include catastrophic outburst flooding. This work defines a function that combines river valley widths and landslide volumes to find the likelihood that a river will be dammed by a potential landslide or 'damability'. We apply the method to the Oregon Coast Range and find widespread high damability especially where rivers flow through steep mountains with strong rocks. Our new workflow is flexible and can be applied more broadly to other regions.

1.1 Introduction

Landslides are a widespread and destructive hazard (Froude and Petley, 2018) with impacts that can cascade from slope failure to flooding when landslides intersect river valleys (Yanites et al., 2025). Landslides can dam the flow of water and create a lake upstream of the slide deposit which may gradually flood roads or infrastructure. However, the greater danger lies in the possibility that the lake can break through the dam in a sudden outburst, draining rapidly and possibly catastrophically (Costa and Schuster, 1988; Fan et al., 2019; Korup and Tweed, 2007). Many historic landslide dam outburst floods have led to widespread destruction and casualties (Costa and Schuster, 1991; Dai et al., 2005, 2021; Sattar and Konagai, 2012; Xu et al., 2009; Zeng et al., 2022). Landslide dams are potential hazards anywhere that steep slopes abut rivers, especially in mountainous regions prone to landsliding (Costa and Schuster, 1988, 1991; Fan et al., 2020).

After a landslide dams a river, human intervention can prevent the rising lake waters from breaching the dam in an outburst flood. The most straightforward method to prevent a large flood is the excavation of a spillway into the landslide dam (Sattar and Konagai, 2012), a technique that has been in practice for at least 500 years (Bonnard, 2011). Spillway excavation can decrease the volume of the impounded lake, and thus the potential flood volume when the dam is overtopped, and can stabilize that flow, decreasing the peak breach discharge (Yan et al., 2022). Timely coordinated landslide dam responses by government agencies have averted disaster around the world (Bonnard, 2011; Duncan et al., 1986; Fan et al., 2020; Yang et al., 2010). However, most landslide dams fail within a short time after they form, with 50% failing within 10 days or less (Peng and Zhang 2012; Costa and Schuster 1988; Ermini and Casagli 2003). The combination of the importance of a response, and the short window for it, necessitates pre-planning as a mitigation technique. The first steps are knowing which river stretches are susceptible to landslide dams, and where dams would be the most dangerous.

The review by Fan et al. (2020) summarizes and tests several metrics used to predict landslide dam formation. These metrics include: the 'annual constriction ratio'(ACR), which concerns the ratio between landslide velocity and valley width (Swanson et al., 1986), the 'Dimensionless Morpho-Invasion Index'(DMI), which is a more complex formulation of the ACR incorporating more physical parameters of the landslide like velocity, density, volume, and hydraulic level (Dal Sasso et al., 2014), the 'Dimensionless Constriction Index' (DCI) that includes parameters of the landslide like geometry, velocity, and grain size, as well as the width of the valley (Ermini and Casagli, 2003), and the 'Morphological Obstruction Index'(MOI), which concerns the ratio between log valley width and landslide volume (Tacconi Stefanelli et al., 2016). The ACR, DMI, and DCI require estimates of landslide velocity, which is difficult to measure for a known landslide, and even more difficult to estimate for ancient or future landslides across a landscape. The MOI (Tacconi Stefanelli et al., 2016) is the simplest and the easiest to implement at landscape scales for susceptibility analysis where the properties of a future landslide must be inferred.

Three methodologies have been used to generate landslide dam susceptibility maps and all roughly follow the format of the MOI taking into account landslide volume and valley or channel width. Tacconi Stefanelli et al. (2020) introduced a semi-automated workflow to estimate susceptibility across the Arno river basin in Italy and used landform classification to measure valley width, and a spatially variable power law fit to a large landslide inventory to estimate landslide sizes. McMeckin (2022) used a somewhat similar technique in the West Coast region of New Zealand and used relative relief as a proxy for landslide size. Wu et al. (2024) developed a globally applicable methodology using a coarse global river dataset of river widths and slope unit area as a proxy for landslide size.

Within the MOI framework (Equation 1), dam formation or non-formation can be inferred from only two parameters: landslide volume and valley width as:

$$MOI = log\ (V/W_V) \tag{1.1}$$

Where V is landslide volume (m^3), and W_V is valley width (m) and MOI is treated as an index for likelihood of dam formation. Conceptually, large landslides impacting narrow valleys form landslide dams and, conversely, small landslides impacting wide valleys do not form landslide dams. A function we refer to as the damability function can estimate which landslide volume/valley width combinations are likely to result in dam formation for a specific region. This function is a modification of the formation volume and non-formation volume equations from Tacconi Stefanelli et al. (2020). Damability functions can satisfactorily separate dam forming and non-forming landslides from a large historical database (Tacconi Stefanelli et al., 2015) and have been used to assess damming predisposition in Italy and Central Asia (Tacconi Stefanelli et al., 2020, 2023). However, the methods for calibrating or fitting a damability function to a new regional dataset are undefined and more widespread applicability of the damability approach remains to be demonstrated.

Here we present a simple probabilistic approach to estimating landslide dam susceptibility from mapped landslide data and digital elevation models. Mapped landslides with and without formed dams are used to quantitatively define a logistic damability function that depends on landslide volume and valley width. Landslide dam formation likelihood is then estimated for the entire study region by combining measured valley widths, empirical volume estimates, and a model of landslide susceptibility.

We demonstrate the utility of this framework for estimating landslide dam susceptibility in the Oregon Coast Range (OCR), United States of America. Tens of thousands of landslides have been mapped in the OCR (Burns and Madin, 2009), including 238 landslide dams (Struble et al., 2020, 2021). Additionally, the OCR is subject to atmospheric rivers and intense precipitation events as well as strong shaking from Cascadia subduction zone earthquakes, all of which compound landslide and landslide dam hazards (Dettinger et al., 2018; Grant et al., 2022). We estimate landslide dam susceptibility by implementing a workflow based on a damability function, which we fit to a local landslide dam inventory. We use a new algorithm to automate valley width measurements. To estimate landslide volumes we use a large database of mapped landslide deposits within the study area to fit a single empirical log-normal distribution of landslide volumes to use across the study area. We also explore the utility of location-specific landslide volume estimates using multivariate regression, however, we are unable to make satisfactory predictions. Using the damability function, we estimate the geometric predisposition to damming, that is, the damability, of a valley. Then, we combine damability values with estimates of landslide susceptibility to find landslide dam susceptibility values. Landslide dam susceptibility maps may be useful to planners (e.g. governmental emergency managers or transportation agencies) to identify places both prone to failure and damming. Finally, we estimate possible lake volumes for all potential dams to provide planners and other end users more information about the scale of potential impacts of future landslide dams. Our results provide a map of the landslide dam formation susceptibility and severity within the OCR. We find that landslide dams are most likely to form in river headwaters, high relief terrain, and more resistant lithologies. Most river stretches with the highest potential for landslide dam formation may only impound relatively small lakes. However, the mapped widespread susceptibility and potential for the largest landslides to form large hazardous lakes that may require prompt mitigation show that landslide dam hazards should not be overlooked across a broader region. We also discuss the damability function method, why it works, its flexibility, and its effectiveness for future evaluations globally.

1.2 The study area: Oregon Coast Range (OCR), USA

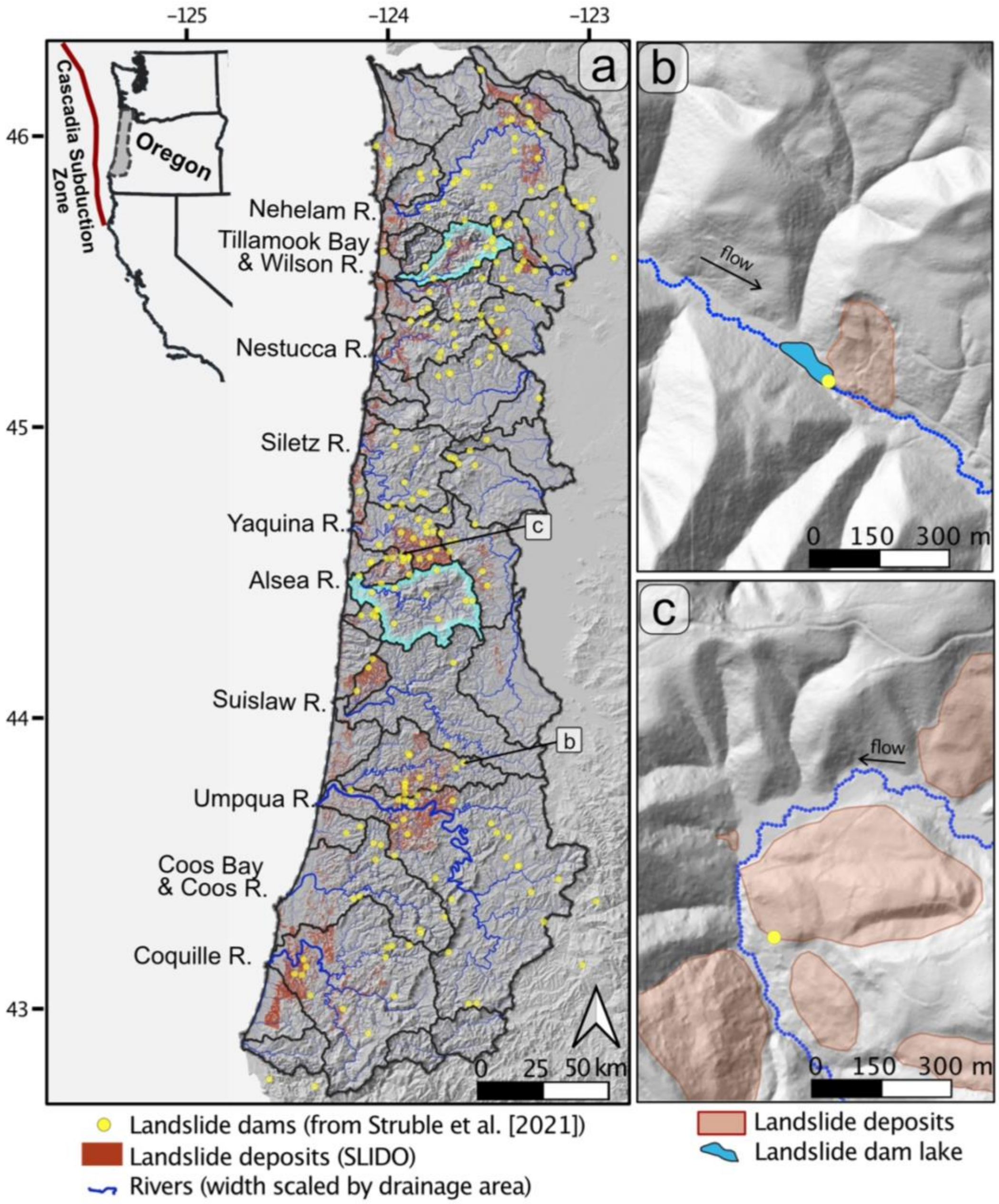

Figure 1.1 a) overview of the Oregon Coast Range study area as a hillshade, derived river network, and landslide inventories. Oregon state-wide landslide Inventory (SLIDO, Franczyk et al. 2020) as red polygons, and Struble et al. (2021) landslide dam inventory as yellow dots. River drainage basins are delineated by black lines, with the Wilson and Alsea basins highlighted in light blue because they are discussed later (Figure 1.8, 1.9). b) and c) depict example landslides of different sizes from the SLIDO inventory, and mapped landslide dam locations from Struble et al., (2021).

The OCR is a roughly 60 km long mountain range along Oregon's Pacific coast, stretching from the mouth of the Columbia River in the north to the Klamath Ranges in the south

(Fig. 1.1). These mountains are unglaciated and reach elevations of ~1200 m. The bedrock of the range is mostly Eocene accreted volcanic terrains and marine sedimentary rocks, predominantly the siltstone and sandstone Tyee Formation in the central and southern areas (Lane, 1987; Roering et al., 2005; Wells et al., 2014). Lithologic variance has been shown to impact geomorphology, with notable units such as the Tillamook Volcanics (North-central study area, Wilson river catchment Fig. 1.1) exhibiting sharper hilltop curvature than neighboring sedimentary units (Struble et al., 2024). Conifer forests cover the landscape, which experiences annual rainfall of 1.6 to 5.1 m (65-200 in.), most of which during the winter and often in the form of atmospheric rivers (Taylor, 1993).

Landslides are common in the OCR. During major winter storms, hundreds of shallow landslides, which often mobilize into debris flows, have been observed (Robinson et al., 1999). Widespread evidence of deep-seated landslides exists across these hillslopes as well (LaHusen et al., 2020). Shallow and deep landslides have been studied and inventoried in detail, including in the Oregon statewide landslide inventory, or SLIDO (Franczyk et al. 2020 red polygons in Fig. 1.1). Landslide patterns within the study area are known to be controlled by sub geologic unit lithologic properties such as the dip or bedding thicknesses within the Tyee Formation (Roering et al., 2005; LaHusen and Grant, 2024).

The SLIDO database is a compilation of landslides that appear on published maps. Many of these landslides were mapped on LIDAR (light detection and ranging) generated digital elevation models following a protocol defined by "Special Paper 42" (Burns and Madin, 2002) which require the mapper to measure, estimate, or calculate additional parameters of the landslide such as volume. We use landslides that were mapped using the Special Paper 42 protocol found in SLIDO version 4.5 directly to estimate landslide volumes in this study. Landslides within the SLIDO database range in landslide type, from shallow soil landslides to deep-seated bedrock landslides, and from debris flows to earth flows to rotational and complex landslides.

Landslide dams have been documented in the area by Struble et al. (2021), who published an inventory of 238 landslide dams (yellow dots in Fig. 1.1). These dams were primarily caused by deep-seated translational or rotational slides. They found that preserved landslide dams are overrepresented in drainage areas of ~1.5 to 13 km^2 and valley widths of ~25-80 m. Despite the proximity of the Cascadia Subduction Zone, few dated landslide deposits or landslide dams can be correlated to earthquakes (Grant, Struble, & LaHusen, 2022; Struble et al., 2021; LaHusen et al., 2020). We use this landslide dam inventory (with additions) to fit the damability function for the OCR.

1.3 Methods

Our approach to estimate landslide dam susceptibility is outlined in Fig. 1.2 and described in detail in the subsections below. First, we provide background on the damability function (1.3.1). We measured valley widths across the study area using a new algorithm based on elevation thresholds (1.3.2). We characterized the future landslide volumes using a log-normal distribution of mapped landslide volumes (1.3.3.1). We also explored using multiple regression to identify a spatially variable way to predict landslide volumes, though ultimately this was not implemented (1.3.3.2). We created a new dam/non-dam landslide dataset to calibrate a damability function (1.3.4.1). Then we fit this data to generate the OCR specific damability function (*Damability$_{OCR}$*), and integrate across the regional log-normal landslide volume distribution to get the equation for dam formation likelihood (*Dam formation likelihood$_{OCR}$*) used in this study (1.3.4.2). Lastly, we calculated landslide dam susceptibility and quantified the magnitude of potential impacts by estimating the volume of landslide dam lakes through a proxy (1.3.5).

Our methods require the input of data from a DEM, a general landslide inventory, a landslide dam/non-dam inventory (an inventory of landslides that intersect river valleys that states whether or not the landslide formed a dam), and a landslide susceptibility map (Fig. 1.2). We used a Lidar DEM from Oregon Department of Geology and Mineral Industries (DOGAMI) Lidar Program Data. The SLIDO landslide inventory records mapped landslide deposit polygons within select study areas throughout Oregon (Franczyk et al., 2020). We used all mapped landslides in our study area following the 'Special Paper 42' (Burns and Madin, 2009) mapping protocols (n>19,000) to estimate landslide volume. The landslide dam inventory of Struble et al. (2021) records points where landslide deposits have dammed or currently dam rivers. We generated a new landslide dam/non-dam inventory by incorporating remapped landslide deposits corresponding to the Struble et al. (2021) points and by assessing a random selection of the SLIDO landslide polygons. We then incorporated the Oregon State-wide landslide susceptibility map, which was generated primarily using the SLIDO landslide inventory, DEM data, and geologic data (Burns et al., 2016).

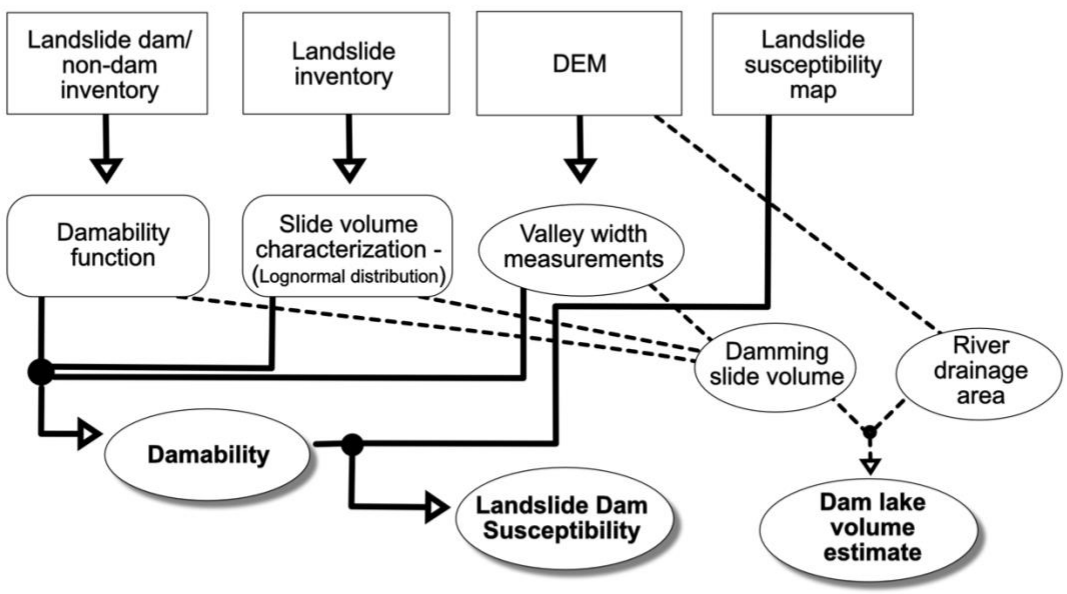

Figure 1.2: Flow chart illustrating path from input datasets (square boxes) to interim results (rounded rectangles and ovals), to outputs (ovals with drop shadows). Rounded rectangles are values/equations that are constant across the study area, while ovals have unique values for each river point. Dashed lines represent the workflow for dam lake volume estimates, while solid lines represent the workflow towards landslide dam susceptibility.

1.3.1 Damability function background

Landslide dam formation is a complex process that inherits all the geologic and environmental uncertainties of landslide initiation and runout, as well as the discharge, erosive power, and channel size or location uncertainties of river valleys. It is difficult to know which hillslopes will fail in landslides, how large the landslides will be, and if the rivers will quickly transport the sediment or become (at least temporarily) impounded. We opt to use a MOI based damability function approach to balance simplicity, predictability, and data availability. Several other metrics require estimates of landslide velocity, which is difficult to measure for a known landslide, and even more difficult to estimate for an ancient or future landslide (Dal Sasso et al., 2014; Ermini and Casagli, 2003; Fan et al., 2020). The methodology of McMeckin (2022), uses a regional proxy for landslide size which does not hold in our study area (section 1.4.1). The global scale landslide dam formation susceptibility evaluation of Wu et al. (2024) bypasses landslide velocity or size. However, it relies on global river datasets that do not include rivers with sufficiently small drainage areas to capture and calibrate with mapped landslide dams in the OCR.

Damability functions require only landslide volume and valley width, simplifying physically derived equations and complexity to two easily modeled terms that can be estimated and measured at landscape scales. Damability functions were introduced by Tacconi Stefanelli et al. (2016) using a large historical dataset including dam forming and dam non-forming landslides from throughout Italy (Tacconi Stefanelli et al., 2015).

They plotted their landslide dam/non-dam inventory in bi-logarithmic volume (m^3) and valley width (m) space on a plot we refer to as the volume-valley width plot (Figure 1.3), then manually placed two functions on the plot to separate landslides into three domains (the formation, non-formation, and uncertain domains), which they named Formation Volume and Non-Formation Volume equations (Fig. 1.3b). These damability functions define landslide volume (V) as a function of valley width (Wv) raised to a power, expressing how large a landslide needs to be to dam a river of a given valley width (Fig. 1.3 b,c red and blue dashed lines respectively). This approach can make analysis of landslide dam likelihoods difficult to present in map view, requiring maps based on both the minimum volume above which a dam is possible to form and the maximum volume above which a dam is unlikely to form, and does not provide any additional uncertainty values other than a domain position. To reflect the uncertainty of landslide dam formation for all volume-valley width pairs in a landscape, we instead define a single damability function surface as a logistic function. For all combinations of volume and valley width, damability is a continuous estimate from 0 - 1 (grey shading in Fig. 1.3a) reflecting the scatter in the empirical data of a specific region. For binary classification of landslide dam formation or not, a single threshold can be adopted (e.g., a damability function at 0.5 likelihood in Fig. 1.3a).

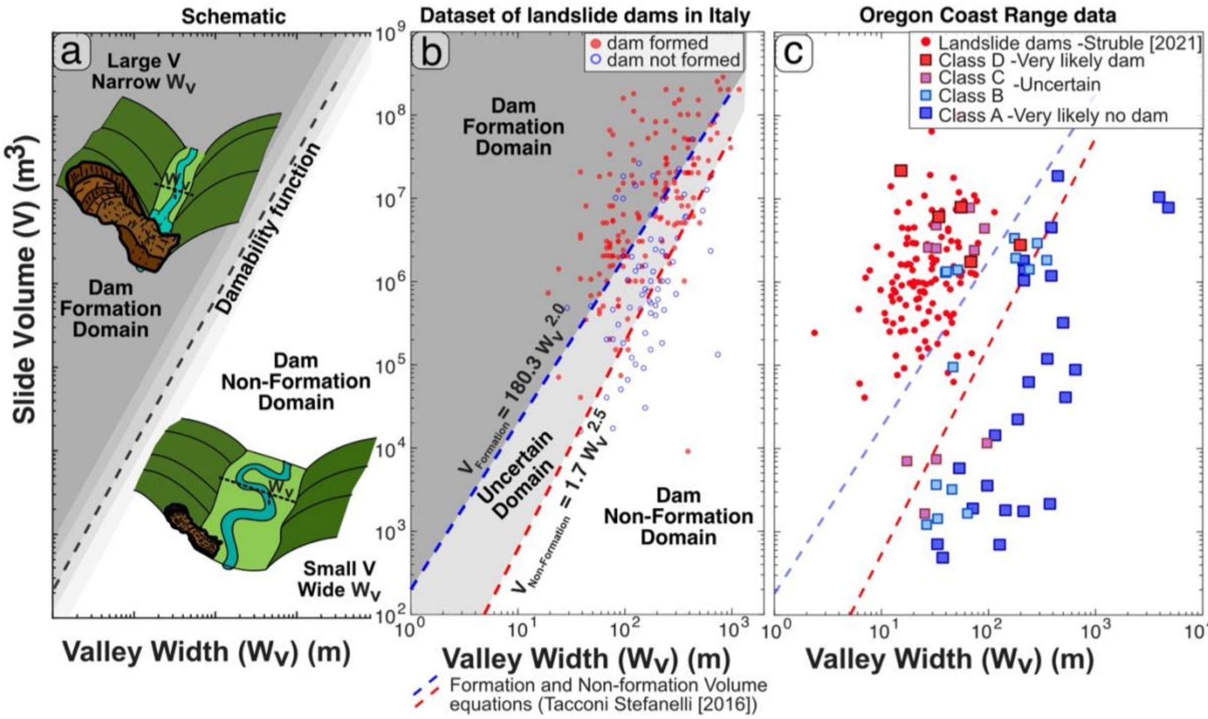

Figure 1.3: The volume-valley width plot showing the damability functions for landslides in log-log valley width and landslide volume space. a) Schematic diagram illustrating the form of the damability function. b) Reproduction of the dataset and functions presented by Tacconi Stefanelli et al. (2016). The formation volume domain function, in the blue dashed line is defined by the lack of slides that didn't form dams above it. The non-formation volume domain function, in the red dashed line, is defined by lack of dam-formed slides below it. c) The dam/non-dam inventory for the Oregon Coast Range (described in section 1.3.4.1.) Known landslide dams from Struble et al. (2021) are plotted as small red dots, and the SLIDO (Franczyk et al., 2020) landslide subset in dark blue squares (very likely no dam), dark red squares (very likely dam) and light blue squares and light purple squares for slides with less certainty. Functions plotted in b) are plotted again in c).

1.3.2 Automated valley width measurement

Several algorithms have been used to calculate river valley width, including landform mapping (Tacconi Stefanelli et al., 2020), topographic position index mapping (McMeckin, 2022), curvature wavelengths (Hilley et al., 2020), and threshold slope and elevation approaches (Clubb et al., 2022). A threshold approach involving the elevation of valley walls above the river has the most physical connection to the pooling of water from river-flow impoundment. We implemented a novel threshold-elevation based approach to calculate valley width using TopoToolbox functions (Schwanghart and Scherler, 2014), which we outline in Fig. 1.4. The advantages of our approach when compared to other methods include: repeatability in the TopoToolbox coding infrastructure (rather than difficult to automate GIS workflows), simplicity of the geometric calculations with no required complex landform classification, and the ease of use in comparison to Python-based codes available (e.g., Clubb et al., 2022).

Our workflow starts with identifying rivers using a flow routing algorithm imposed on a lidar DEM of the study area which is publicly available from the Oregon Department of Geological and Mineral Industries. We down sampled the DEM to 2m resolution (from the original ~1m resolution) for computational feasibility in this study, however the valley width algorithm performs well on DEMs with resolutions from 1m to 10m. We demarcated rivers based on a minimum drainage area cutoff of 2.25 km^2, which balances computational feasibility while capturing the prominent drainage area positions of the mapped landslide dams in the study area (Struble et al., 2021).

Our algorithm (*ElevationThresholdValleyWidth*, Morgan, 2026) categorizes a pixel as part of the valley if its elevation is less than a defined threshold elevation above the nearest river pixel along a flow path. Profiles are taken perpendicular to the river (Using TopoToolbox's swath profile extraction) to measure the distance that is within the valley. When the river does not flow parallel to the valley centerline, this results in profiles that record widths that are too large, but when the river flows parallel to the valley, the recorded width will be correct and the minimum possible recorded width. Our algorithm captures the minimum value along a moving window (100 m radius in this study) that exceeds river's meander wavelength, which is generally <150 m. While the elevation threshold choice alters the magnitude of the valley width measurements, it does not affect the relative spatial distributions (Supp. Fig. S1.1). A threshold elevation of 10 m was found to match valley widths previously hand measured in a catchment within the study area (May et al., 2013) (Supp. Fig. S1.2). Using this approach, valley width measurements were extracted from the river network every 100 meters for input into the landslide dam susceptibility analysis.

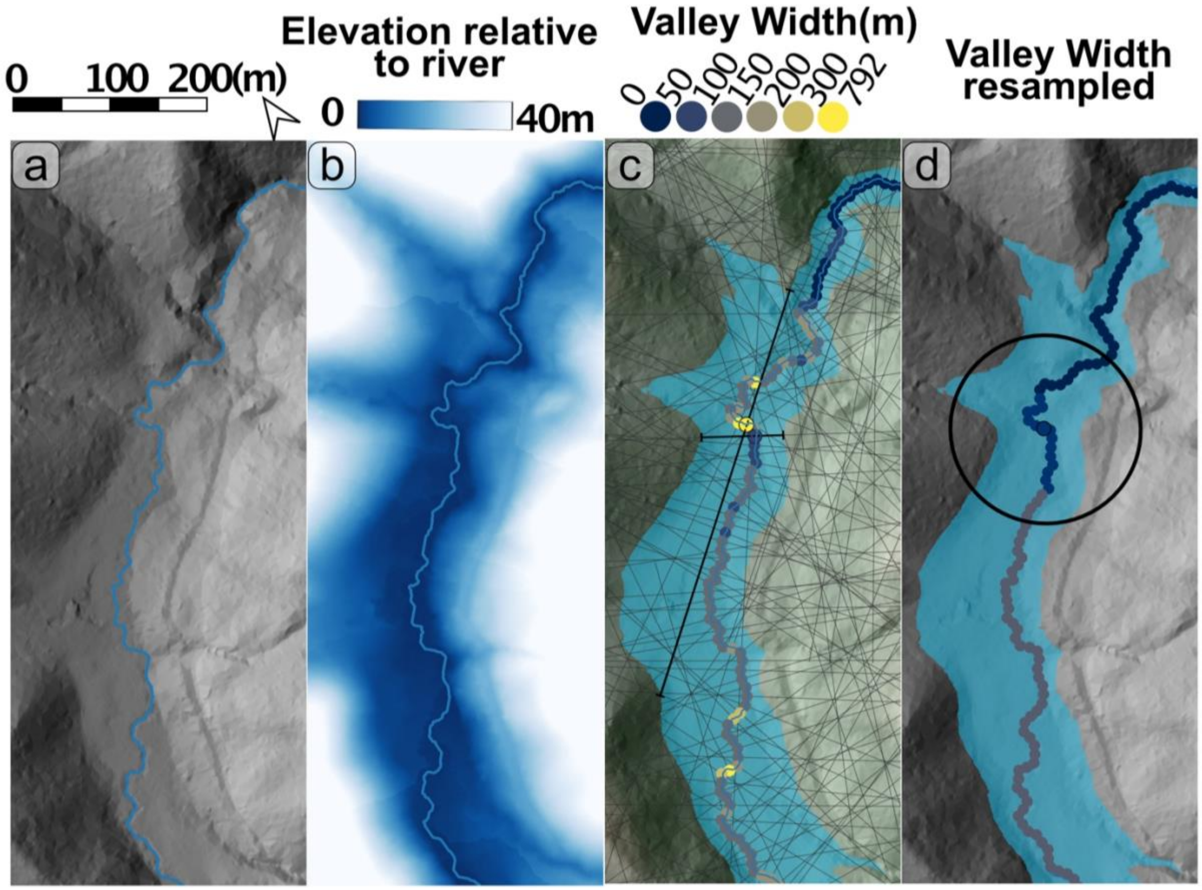

Figure 1.4: Overview of valley width methods. a) hillshade of a sample valley, with the extracted river plotted, b) white to blue colour scale representing elevation above the river, along a flow path, c) valley extraction plotted as a blue polygon, light grey lines represent profile lines perpendicular to the river path, and river points are coloured by how much of their profile line lies in the valley. Two black profile lines and outlined river points, illustrate anomalously high values where the river path is perpendicular to the valley, and accurate low values where the river is parallel to the valley. d) final valley width result, which is the minimum value within a 100 m radius moving window, the size of which is plotted as a black circle and the same colour scale as c.

1.3.3 Landslide Volume Modeling

1.3.3.1 **Estimates of landslide volume**

The size of future landslides can be estimated numerically based on physically derived simulations of slope failure on the terrain (Bellugi et al., 2021), or empirically by using existing volume or area distributions from landslide inventories (Lombardo et al., 2021). We developed an empirical volume distribution for mapped landslides that we then used to estimate landslide dam formation likelihood. We opted for the empirical approach because 1) it is computationally expensive to simulate a landslide on every slope in our study area and 2) an empirical approach may be more likely to account for the wide range of possible landslide sizes observed in our study area. Whereas power law scaling (Tebbens, 2020) and similar alternative functions (Stark and Hovius, 2001) have been used to characterize landslide size distributions in the past, we choose a log-normal distribution. Medwedeff et al. (2020) demonstrated that log-normal probability distributions can adequately fit landslide size inventories, and that they capture absolute characteristic landslide sizes, while power laws only capture relative frequencies. The same power law (excluding cutoff size) could be fit to a set of landslides all under 10 m^3 in volume, as well as the 10^6 m^3 landslides in our inventory as long as the relative frequencies matched up. Log-normal functions are also advantageous for working with other statistical models that might require size estimates (Bryce et al., 2022; Lombardo et al., 2021; Moreno et al., 2022).

We treated landslide volume estimation as a constant single statistical distribution across the study. We used the normal distribution of the log (base 10) of the landslide volume distribution captured from the SLIDO inventory (Fig. 1.5). The distribution was fit using MATLAB's normfit function and has a mean (μ) of 4.44 (~log (28,000 m^3)) and standard deviation (σ) of 1.25. The volumes are estimated by the mapper following the 'Special Paper 42' landslide mapping protocols, (96% of inventory has volumes) where the mapper estimates or measures the slide depth and multiplies that by the slide area (Burns and Madin, 2009). A comparison of the log-normal fit and data distribution is visible in Fig. 1.5.

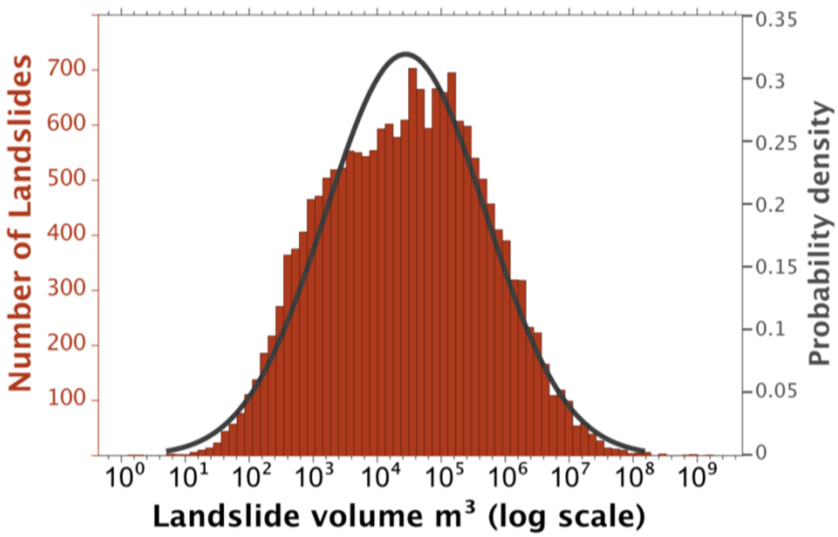

Figure 1.5: Histogram of the base 10 logarithm of landslide volumes from the SLIDO landslide inventory (Franczyk et al., 2020). The log-normal fit probability density function is plotted in grey.

1.3.3.2 Spatially variable estimation of landslide volume (not implemented in final workflow)

The characteristic size of landslides may not be constant across the OCR. Variations in local lithology and structure may impact the style or size of landsliding (LaHusen and Grant, 2024). With these concerns in mind, we attempted to make location/hillslope specific landslide volume predictions using statistical regressions. A few studies have demonstrated probabilistically that landslide deposit area may depend on local topographic morphology (Lombardo et al., 2021; Moreno et al., 2022; Qiu et al., 2018). Lombardo et al. (2021) and Moreno et al. (2022) implemented versions of a generalized additive model (GAM) to predict the maximum landslide surface area within a given slope unit using a set of predictor variables including: relief, slope, roughness, and earthquake shaking. Both studies trained the models with data from earthquake triggered landslide inventories and determined that their data-driven statistical modelling approaches are moderately effective at predicting landslide volumes. To consider if such relationships hold for the OCR, we used several methods to create a statistical model using local landscape parameters to estimate local landslide volume. We chose predictors shown to work in previous studies (Lombardo et al. 2021; Moreno et al. 2022), which included: relative relief, slope (mean and range), profile curvature (mean and range), vector ruggedness measure (mean and range)(Sappington et al., 2007), terrain ruggedness index (mean and range) (Riley et al., 1999), and geologic rock type. We extracted these variables using both a 500 m radius moving window, which is large enough to span from most rivers to hilltops in the study area, and slope unit delineations following the input parameters of Moreno et al. (2022) and the algorithm of Alvioli et al. (2016). We trained statistical models with volumes recorded from an 80% training dataset of the SLIDO inventory. The regression models include general linear models (GLM) using linear and quadratic n=4 functions for each predictor variable, to provide a simple and more complex but interpretable results and generalized additive models (GAM).

1.3.4 Region specific damability function fitting

1.3.4.1 **Function calibration data development**

To identify a region specific damability function that can be used within the OCR, we populated the volume-valley width plot (Fig. 1.3c) with local landslides that both formed and did not form landslide dams. We used an inventory of 239 landslide dams within the OCR from Struble et al. (2021) as our positive dataset of landslide dams. Identifying landslides that entered river valleys but did not form dams is less straightforward to assess without a long historical landslide dam inventory. To develop a set of null, or non-damming slides, we analyzed 100 landslides from a subset of the SLIDO inventory: 50 randomly sampled landslides and the 50 landslides with the largest surface area. None of these landslides currently dam rivers, so we assessed them for evidence of past dam formation. Signs of past dam formation include: an arcuate toe that extends well into river valley or is cut off before reaching other side of the valley, an inner gorge where the landslide intersects the river, and evidence of aggradation upstream of possible dam location [Struble et al. 2021]. Assessing past landslide dam formation is subjective, thus we categorized each landslide deposit with a four part (A-D) Past Dam Formation Assessment (PDFA) class, where a PDFA-class A landslide very likely did not form a dam, a PDFA-class D landslide very likely did form a dam, and PDFA-class B and PDFA-class C represent intermediate points where the inference of past dam formation is uncertain (Supp. Fig. S1.3). For each landslide used in the calibration, we remapped the surface area expression of the landslide, converted the area to volume using the area-volume scaling relationship of Larsen et al. (2010) for bedrock landslides, and manually mapped the valley width downstream of the landslide.

1.3.4.2 **Dam formation domain model fitting**

We modeled the likelihood of dam formation from observed dam and non-dam forming landslides as a modified logistic function (Eq. 1.2) using a modified version of MOI, as the predictor variable. Equation 1.2 is the generalized form of the damability function. During model development, we found improved fit if we modified MOI as MOI* = log(V)/log($a \cdot W_V$):

$$Damability = \frac{1}{1+e^{-k(MOI* - X_0)}} = \frac{1}{1+e^{-k(\frac{log(V)}{log(aW_V)} - X_0)}} \tag{1.2}$$

Where k, X_0, and a are fitted parameters related to curve steepness, the expected midpoint value, and scaling factor between valley width and volume, respectively. Predicted values of damability range from zero to one, reflecting the likelihood that a given combination of landslide volume and valley width would form a landslide dam. Log base 10 transformed values of valley width and landslide volume were used to better model landslides and landscapes over several orders of magnitude in scale with a consistent relationship. The damability function was fit using nonlinear least squares regression using the SciPy curve_fit regression tools for Python (Virtanen et al., 2020). When fitting the damability function, PDFA-class D landslides were assigned damability values of 1, class A were assigned zero, and the intermediate classes C and B were assigned 0.66 and 0.33, respectively. During model development, we considered alternative combinations of landslide volume and valley width to solve for a logistic damability function. While alternative models (e.g., linear combinations of volume and width) perform similarly to our preferred model (Eq 1.2), we selected this model for both its good performance and to build on previous work where MOI has been found to be a reliable estimator of landslide dam formation.

Once the local fitting parameters in Eq. 2 are found we can use it to estimate local damability. In this study we can measure local valley widths but must use a log-normal distribution for volume. So, for each valley width we integrated all the expected damability values across the entire lognormal distribution of possible volume values. This resulted in an equation for local Damability values only as a function of valley width which we call *Dam Formation Likelihood* that incorporates the full form of the locally fit Damability function and the landslide volume characterization.

1.3.5 Dam susceptibility, and dam lake volumes

To make our estimates of damability more useful to understand local hazard and risk, we incorporated estimates of landslide susceptibility to produce estimates of landslide dam susceptibility, and we estimated potential landslide dam lake volumes for all potential dams. Landslide dam susceptibility was computed as the product of damability and a landslide susceptibility value (or LSS_{val}) transformed from the categorical statewide map of landslide susceptibility (Burns et al., 2016)

$$Landslide\ dam\ susceptibility = Damability \cdot LSS_{val} \tag{1.3}$$

The statewide map breaks down susceptibility into 4 categories: 'low' (1), 'moderate' (2), 'high' (3), and 'very high' (4), where the category is determined by landslide inventory analysis, geology, and slope; except for the 'very high' category, which is determined by the location of mapped landslides. For our analysis we assign these qualitative classes values (LSS_{val}) of 1 for 'high' and 'very high' areas, 0.5 for 'moderate' areas, and 0.25 for 'low' areas. This quantification was chosen conservatively to reflect that landslides still occur in the low and moderate zones. In a validation test with a historical landslide inventory (Burns et al., 2016), 65% of landslides were in 'high' areas, 16% in 'moderate' and 5% in 'low'. Landslide dam susceptibility values range from 0 to 1.

To estimate the possible lake volume arising from a future landslide dam at each river point, we used a scaling relationship developed by Argentin et al. (2021) through simulated landslides on alpine rivers. This proxy relationship calculated from only landslide volume and river drainage area was found to account for 60% of the variation in modelled lake volumes (EQ. 7 in Argentin et al., 2021). At each river point we input the measured drainage area and a landslide volume corresponding to the minimum volume needed to likely dam a river of that width. The minimum dam forming landslide volume is calculated as the landslide volume where the damability value is 0.5 (V_{50}-Eq. 1.3). At present, we are limited to this relationship developed on Alpine rivers, though we welcome future studies extending the fit of such lake size proxy relationships across various landscape types.

1.4 Results

1.4.1 Landslide volume characterization

Figure 1.5 presents the normal fit to the log (base 10) transformed volumes from the >19,000 landslides in the SLIDO inventory (referred to hereafter as a lognormal). The goodness of fit was evaluated using a Kolmogorov-Smirnov with a K-S statistic of 0.03 indicating a good approximation. We use this distribution as an input for landslide volume estimates across the study area where we calculate damability.

We use the same volume distribution across the study area because the location specific estimates are unsuccessful. Figures S1.4 and S1.5 show our best fitting model predictions for landslide volume based on location properties (e.g., relief, slope, roughness, and lithology) compared to measured landslide volumes. In a successful statistical prediction, we would expect the points to extend along the 1:1 line without systematic errors. Instead, we find that predicted volume values are significantly different than observed volumes (Figures S1.4, S1.5). Model result errors are presented in Table S1.1. Based on these results for the SLIDO inventory, we are unable to justify using these statistical regression techniques to predict local landslide volume based on local hillslope properties in this case.

1.4.2 Damability function for the Oregon Coast Range

Through our logistic regression modelling, we solved for the damability function fit to the landslide dam/non-dam inventory for the Oregon Coast Range (*Damability$_{OCR}$*). The function is visible as shading in Fig. 1.6, and in the form of Eq. 1.2.

$$Damability_{OCR} = \frac{1}{1+e^{-2.5937\left(\frac{log(V)}{log(2.338\times W_V)} - 4.0168\right)}} \qquad (1.4)$$

where V is the landslide volume in m^3, and W_V is the valley width in m (all logarithms are base 10). Probabilities of dam formation given valley width and landslide volume are shown as gradational shades of grey from < 10% to > 90% likelihood in Fig. 1.6.

To solve for the minimum landslide volume needed to dam a given valley width, we use the 50% likelihood contour of the damability function, which can be expressed as a function of valley width as:

$$V_{50} = 0.004\, {W_V}^{3.861} \qquad (1.5)$$

V_{50} is also referred to as the minimum dam forming landslide volume because it matches the volume of slide, above which dams will most likely obstruct the valley.

1.4.2.1 **Landslide dam formation likelihood**

To estimate the potential for future landslide dam formation given some unknown landslide volume and uncertainty in the damability function, we combine valley width measurements, the empirical distribution of landslide volumes (1.4.1), and Eq 1.4. For all valley widths, landslide *Dam Formation Likelihood* (Fig. 1.6c) was computed as the sum of expected damability (Fig. 1. 6b) for the entire lognormal distribution of expected landslide volumes (Fig. 1.6a). For ease of use, we then fit the landslide dam formation likelihood values as a function of valley width as:

$$Dam\ formation\ likelihood_{OCR} = 1 - \frac{1}{1+e^{-4.575(W_V - 1.745)}} \qquad (1.6)$$

Where only valley width (Wv, m) is a required input.

Landslide *Dam Formation Likelihood* values computed using Eq. 1.6 range from zero to one, and reflect the likelihood a landslide forms a dam in a valley of a certain width, given the distribution of landslide volumes observed in the OCR and the uncertainty in the damability function. *Dam Formation Likelihood* values can be interchanged with damability values, for example in equation 1.3, and for brevity we interchange these terms when referring to our results for the OCR. For local studies where the expected distribution of landslide volumes is different, or case studies of known volumes, this integration of volume and damability could be repeated to reduce the uncertainty in predicted dam formation likelihood for known valley widths.

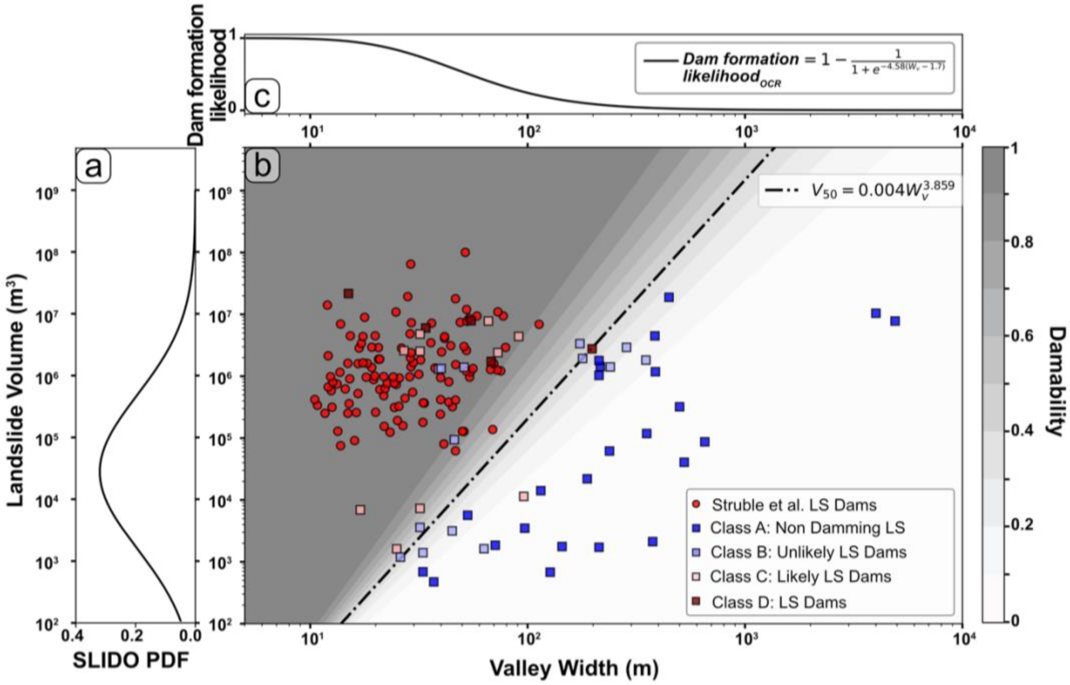

Figure 1.6 Landslide damability functions. a) distribution of landslide volumes in the Oregon Coast Range. b) The same data as plotted in Fig. 1.3c shading from grey to white shows the likelihood of a width-volume pair being in the formation domain. c) Integrated *Dam Formation Likelihood* values as a function of valley width that incorporates uncertainty in future landslide volume and the Damability function.

1.4.2.2 **Validation**

We used the dams mapped by Struble et al. (2021) (shown as yellow dots in Fig. 1.1) to explore the validity of this method. River stretches with mapped landslide dams have much larger damability and dam susceptibility values than the general population of all river stretches in the study area (Fig. 1.7a). Most of the previously mapped landslide dams lie on river stretches with dam susceptibility values greater than 0.5 (78% of landslide dams, vs 28% of all river points) (Fig. 1.7a). We acknowledge that this line of model validation is somewhat circular, as the dams were used to calibrate the damability function that sets the dam susceptibility values, and sometimes past dams can result in the narrowing of valleys where the river cuts through the dam deposit. We also randomly withheld 12.5% of the dam forming and dam non-forming landslides, fit a new damability function, and checked the withheld points to the new function. The new function does not deviate significantly from the fit to all data points and fits all the withheld datapoints (Supp. Fig. S1.7). We also note that the damability values are calculated with algorithm-extracted valley width values rather than the map measured valley widths used in the calibration.

To further test the performance of the method and to identify a threshold to separate river stretches with high dam-formation potential, we used a Receiver Operating Characteristic (ROC) curve. ROC curves relate fractions of positive results (river points with a dam) and negative results (river points without a dam) to decision boundaries. However, we do not have many mapped river stretches without dams so we substituted the entire population as "negative results", which we find reasonable considering that there are <300 mapped dams compared to the 185 thousand calculated river points. Though not ideal for area under the curve model verification (AUC=0.834), this simplification is appropriate to find the threshold to separate river points with dams from all river points. We found this threshold to be 0.35 by maximizing the "true positive rate" minus the "false positive rate." As a result, river stretches with landslide dam susceptibility values of 0.35 or greater are considered river stretches with *dam potential*.

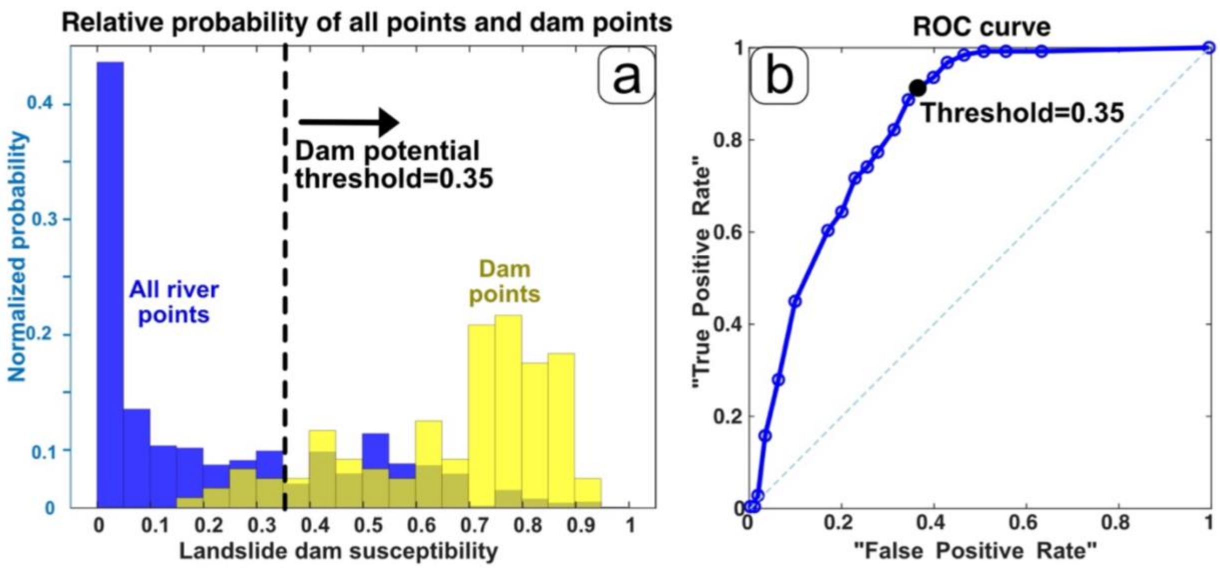

Figure 1.7: a) Normalized histogram of landslide dam susceptibility values for all river points (blue), and points closest to mapped dams (yellow). b) Receiver Operating Characteristic (ROC) curve for landslide dam susceptibility values comparing river stretches with mapped landslide dams and all river stretches.

1.4.3 Damability, dam susceptibility, and lake volume

Across the study area, 51% of the calculated damability values are under 0.25, 19% between 0.25 and 0.5, 20% between 0.5 and 0.75 and 10% greater than 0.75 (Supp. Fig. S1.6). Dam susceptibility values follow a similar distribution but are skewed lower, with 57% less than 0.25, 15% between 0.25 and 0.5, 18% between 0.5 and 0.75 and 10% greater than 0.75 (Fig. 1.8). 36% of the values are greater than the 0.35 dam potential threshold identified in section 4.2.2. Low values are prominent in large rivers, low elevation tributaries, and valleys draining to the east. High values are prominent in higher elevation rivers, most low drainage area tributaries, and the core of the mountainous areas (Fig. 1.8).

Figure 1.8 shows that notable large areas of higher dam potential are found in the mountains around Tillamook Bay, inland Siletz River catchment, and in the headwaters of the Coos and Coquille rivers. In general, catchments draining east have significantly lower landslide dam susceptibility values than those draining west. In addition, tributaries and more mountainous river stretches tend toward higher landslide dam susceptibility values, whereas coastal regions and the eastern edge of the study area record lower values.

To illustrate catchment scale patterns and differences in landslide dam susceptibility values across the OCR, we highlight two catchments, the Wilson and Alsea Rivers (Fig. 1.8 b and c). These drainage basins have similar drainage areas, and both drain west, but they also represent the variation in landslide dam susceptibility values across the OCR, making them useful to compare. Within the Wilson River catchment, nearly all the tributaries contain high landslide dam susceptibility and much of the main river stems have moderate to high landslide dam susceptibility. In contrast, within the Alsea River catchment, only some of the tributaries reach high dam susceptibility, and much of the main stem has relatively low dam susceptibility.

Using the relationship of Argentin et al. (2021), measured drainage areas, and estimated minimum damming landslide volumes (V_{50}) from Eq. 1.5, we estimated the possible impounded lake volumes at each river point. The lake volume estimates primarily correlate with river drainage area (Fig. 1.9). Lake volume estimates for every river point span 11 orders of magnitude, while the volume predictions at potential dam sites are significantly lower and peak at closer to 1000 m^3(Fig. 1.9). Within the Wilson River basin over 69% of the river stretches are above the potential dam threshold, and much of the main stem, with higher estimated lake volumes (>10^4 m^3). Within the Alsea basin only 40% of the river points are above the dam potential threshold. The Alsea River mainstem primarily does not have points above the potential dam threshold values (Fig. 1.9), meaning that most of the susceptible river stretches within the basin would hold relatively small lakes.

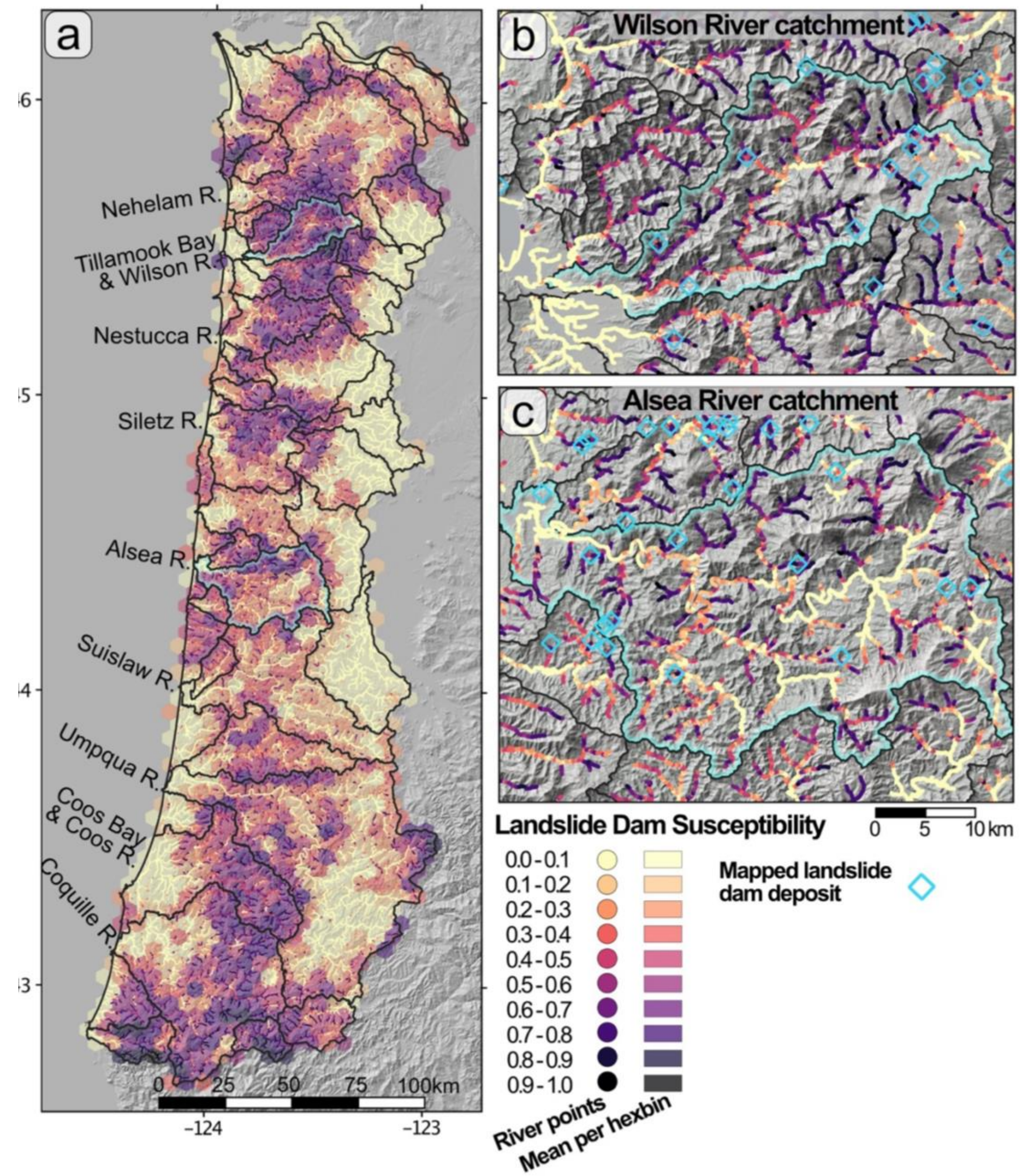

Figure 1.8: Landslide dam susceptibility estimates for the Oregon Coast Range. a) shown as averages over ~6 km across or ~30 km^2 area hexagons as well as for individual 100m long river stretches. b) Wilson and c) Alsea catchments. Mapped landslide dams shown as light blue diamonds.

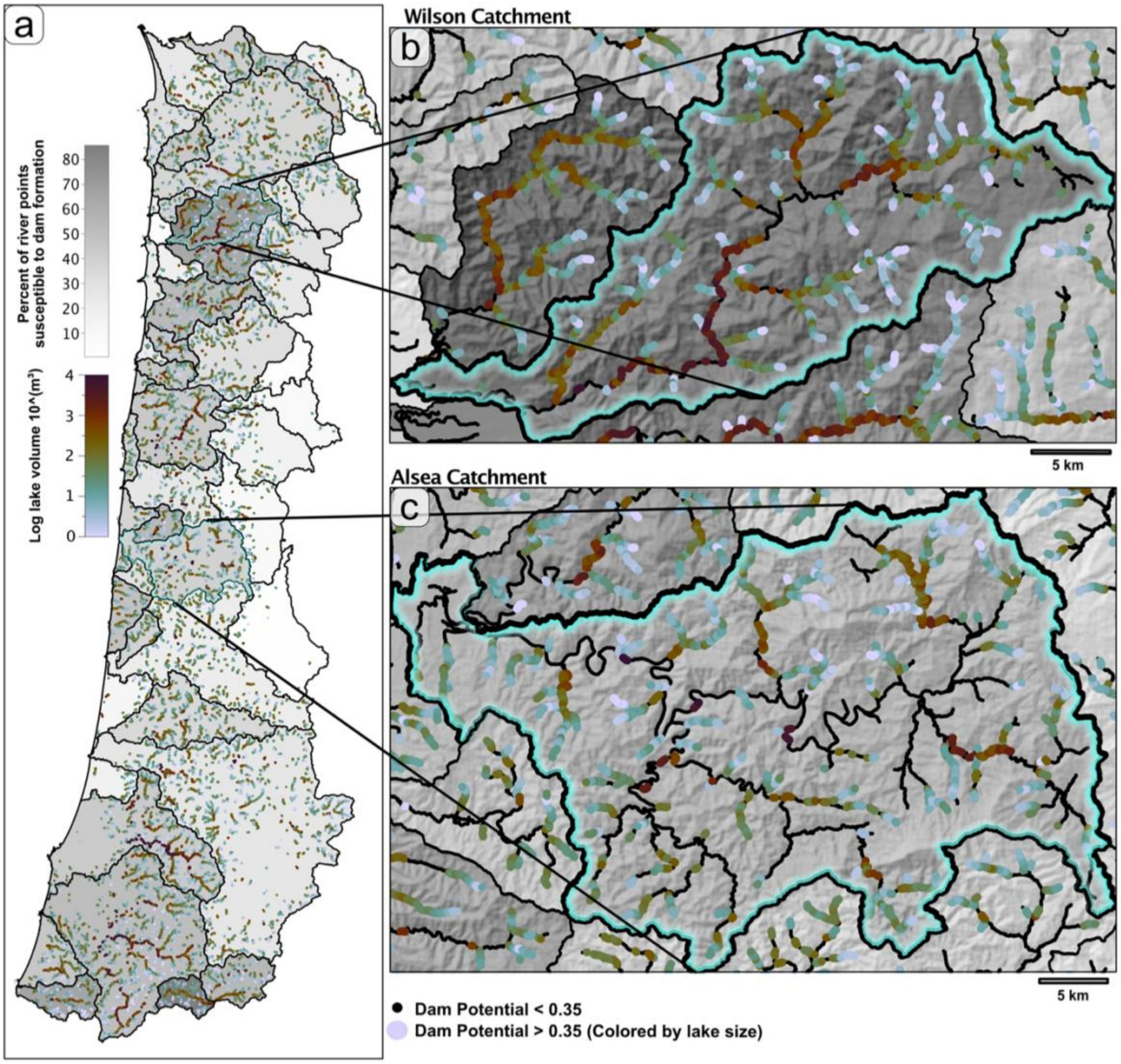

Figure 1.9: Representation of landslide dam potential across the study area. a) Drainage basins are colored along a greyscale by the percent of river stretches within the basin that have dam potential values above 0.35 the dam potential threshold. Only those potential dam river points are plotted as blue scale dots where the shade of blue is represented by the estimated dam lake volume that would form at that point. b) and c) depict the Wilson and Alsea catchments respectively. In insets river locations with dam potential values less than 0.3 are plotted as a black line.

1.5 Discussion

1.5.1 The Damability function

1.5.1.1 **Damability function form**

We present an approach to estimate landslide dam susceptibility using a logistic regression to find a probabilistic damability function. Past studies implementing damability functions, using datasets from Italy, (Tacconi Stefanelli et al., 2016), and the Cordillera Blanca in Peru (Tacconi Stefanelli et al., 2018), relied on manually placed lines separating formation, non-formation, and uncertain domains (Fig. 1.3b). The probabilistic approach to the damability function regression that we present here allows for a characterization of the uncertainty of dam formation. Additionally, the probabilistic approach collapses the damability result down to one dam formation likelihood value, rather than one of three domain positions, which makes adding other useful metrics (e.g,. landslide susceptibility, or estimated dam lake volume) more straightforward, and simplifies hazard visualizations.

The logistic regression methodology that defines the damability function is flexible and can be applied to any dam/non-dam landslide inventory. The damability function for the OCR used in this study is found using the new morphology-based landslide dam/non-dam inventory we generated. While we have fit the currently available inventory, new input can affect the damability function slope and uncertainty. Additional landslides, especially those corresponding to underrepresented valley widths or volumes, could alter the shape of the function (Supp. Fig. S1.8).

Conceptually, the form of the damability function represents how efficient a slide of a specific volume is at running out and damming a river valley. Studies have shown that, broadly, landslide runout scales as a function of landslide volume (Corominas, 1996; Pollock, 2020; Whittall et al., 2017). Pollock (2020) fit the largest dataset of landslide volumes and runout length data to find a function relating the two, which if rearranged into the form of Eq. 1.5 has an exponent 2.87, and coefficient of 0.0018 (dimensionless). The line representing this function in the volume-valley width plot has a slope between the Italian damability functions and the OCR damability function and is shifted towards larger lengths than both (Supp. Fig. S1.8). The shift towards larger lengths suggests that landslides of a given volume have a consistently larger runout length than the width of the valley that they can dam. The observation that landslide volume to runout length is broadly consistent across landscapes, suggests that new dam/non-dam landslide inventories from other regions are likely to be reasonably fit by a damability function. However, further work is needed to assess if it will be possible to move beyond the need for local calibration of regional damability functions.

In the two sites where we do have dam/non-dam inventories (Oregon and Italy) we find that distinct damability functions fit the two areas (Supp. Fig. S1.8). The Oregon damability function has a lower V threshold at W_V=1 suggesting small slides can dam larger valley widths. However, due to the lower slope of the Italian damability function (V_{50} exponent is 1.67 vs 3.8 for OCR), large landslides in Italy seem to dam larger valley widths than slides with a similar volume in the OCR. We speculate that small slides in Oregon may be dominated by long runout debris flows whereas large slides are dominated by rotational failures with less of a flow style / long runout compared to large Italian slides. Alternatively, differences in damability functional forms may be related to data gaps and outliers in the calibration slides. For example, there are a couple outlying very small damming landslides in the Italian inventory (Fig. S1.8-b) and our inventory has relatively few landslides with volumes from 10^5-10^6 m^3 and valley widths from 50-120 m (Fig. 1.6). The width of the decision boundary (uncertain areas where damability values are between 0 and 1), may also be related to data gaps. It is narrower for low volumes and widths than larger volumes, while this is less pronounced for our fit to the Italian inventory (Fig. S1.8-b), a similar trend exists and both inventories have few small ($< 10^5$ m^3) dam forming landslides, which makes it difficult to evaluate this trend.

Local geology, geomorphology, and climate all likely indirectly control the form of the damability function. Landslide dams occur in regions with drier or wetter climates, glacial or non-glacial geomorphic histories, and minimal or extreme relief. Regional differences in damability functions should be explored through the fitting of more dam/non-dam calibration landslides.

1.5.1.2 **Landslide volume characterization**

Using a damability function for susceptibility analysis requires study-area wide measurements of valley widths and landslide volume estimates. While we did not test various methods for valley width estimation in depth (See Supp. Fig. S1.1 and S1.2), we did explore multiple methods for landslide volume estimation.

There are reasons to suspect that landslide volume is not constant across the study area. For example, some areas within the Tyee formation are dominated by small shallow landslides, are characterized by steeper more planar slopes with high drainage densities and may have narrower valley widths. Alternatively, landscapes with high densities of large deep seated landslides are characterized by scalloped hillslopes and wider (or more variable) valley widths (LaHusen and Grant, 2024). As such, the narrow valleys where damability values are high may only be exposed to small volume shallow landslides; while the wider valleys, where damability values are low, may be more likely to see large volume deep seated landslides. If so, we may be underestimating the damability for the wide valleys because they may be more likely to experience a large volume landslide than the rest of the study area.

This concern motivated our unsuccessful attempt to estimate variable characteristic landslide volumes across the landscape. We used measurable (at the regional scale) properties of the landscape to find a regression model to predict landslide volume (Fig. S1.4 and S1.5). We did not satisfactorily predict the SLIDO landslide volumes. This is in contrast to the studies of Lombardo et al. (2021) and Moreno et al. (2022), who implemented versions of a generalized additive model (GAM) to predict the maximum landslide surface areas within a given slope unit.

Methodological differences may play a role in these conflicting results (See Supp. Fig. S1.4), though we suspect that the input landslide inventory used as the training dataset makes the largest difference. Both Lombardo et al. (2021) and Moreno et al. (2022) used datasets from earthquake triggered landslides. Earthquake triggered landslides may have different characteristics, including failure style, than precipitation triggered landslides (Densmore and Hovius, 2000; Meunier et al., 2008). Landslides triggered by the same earthquake shaking, on the same day, have a limited spatial extent and may also exhibit similar properties on similar slope types. The SLIDO inventory includes a wide range of failure styles, includes landslides which occurred at different times by different triggers on adjacent slopes, and was mapped by several different authors.

The volume of a landslide is controlled by many factors including: the height and width of the hillslope, the area of the unstable terrain, the distribution of frictional strength parameters, the depth and shape of the failure plane, the triggering forces, and the landslide type. The complex interplay of these parameters makes estimating the volume of a possible future landslide on any given slope difficult. Slide volumes may also be controlled by hyper local properties such as the meter scale variability in cohesion or groundwater recharge (Bellugi et al., 2021; Montgomery et al., 2009). A specific hillslope in our study area could fail in a variety of ways, meaning that the landslide volume is not necessarily predictable by the variables we can measure at regional scales.

These results suggest that it is not straightforward to use hillslope properties or geometry as a proxy for landslide volume in landslide dam susceptibility analyses. McMeckin (2022) used relative relief as a proxy for landslide size and Wu et al. (2024) used delineated slope unit area as a proxy for landslide size. It is possible and intuitive that these proxies match best the largest possible landslides a hillside could produce, which may be more important than the mean landslide size for landslide dam analyses. The benefits of slide size proxies, including the potential to eliminate the need for rare, detailed landslide inventories, should motivate future research exploring controls on landslide volumes, especially in the context of landslide dam susceptibility analysis.

Instead of site-specific landslide size proxies, we are forced to use a region wide empirical approach to landslide volume estimation based on the mapped landslides within the study area. Tacconi Stefanelli et al. (2020) also used mapped landslide inventories by implementing a spatially determined power law exponent to estimate landslide volumes. However, patchy spatial coverage of the SLIDO landslide inventory, inconsistent lower volume threshold recording, and the lack of spatial coherence in landslide volumes in places where the inventory is complete make this power law-based method less applicable than the overall log-normal volume distribution. Using a single distribution works well for dam susceptibility analysis in regions where landslide inventories exist. In this study we necessarily assume that landslide volume remains unpredictable, and proceeded with susceptibility estimates controlled by valley width (Eq. 1.6), which we justify by the predominantly narrow valley widths at the mapped landslide dam deposits (Fig. 1.7a) (Struble et al., 2021).

1.5.1.3 **Future applications**

We expect that the damability function methodology – as it is currently presented – will be applicable to other regions, especially neighbouring areas of the Pacific Northwest of the US, although it will always be limited by available data sources. Valley width estimations using our algorithm are only applicable in locations with a 10 m resolution or better DEM. A detailed landslide inventory is required to characterize the landslide volume distribution. Though inventory quality and completeness vary, the use of a lognormal distribution insulates the characterization from small changes in estimated landslide volumes. A landslide dam/non-dam inventory is needed to refine the local damability function. Lastly, landslide susceptibility information is also required and often defined using a combination of landslide inventories and geomorphic measurements. These requirements show the importance of detailed landslide deposit inventory mapping and suggest that including a valley connection term and dam/non-dam value would be a helpful addition to the list of data attached to landslides in inventories. The damability approach presented here can be modified to use different methods for measuring valley width and estimating landslide volume, and it can be recalibrated with new data from other regions. Future studies may successfully employ machine learning based methodologies for any of these parts of the workflow. Large-scale regional studies will have higher uncertainty because various landscapes with different lithologies, glacial and tectonic histories, fluvial erosion patterns, and climatic controls will be included. However, more large-scale studies are necessary to quantify landslide dam hazards and can be completed using the damability function approach.

1.5.2 What controls regions of higher landslide dam susceptibility?

Due to the nature of our approach, relative differences of dam susceptibility values across the study area are almost entirely driven by differences in valley width. The damability function and landslide volume characterization are constant across the study area. The landslide susceptibility factors only have a small effect on spatial trends in dam susceptibility estimates, as most locations with high damability also have high landslide susceptibility.

In general, valley width increases with increasing drainage area, which results in lower estimations of landslide dam susceptibility values at high drainage areas and at lower elevation and coastal regions (Fig. 1.10a). While local channel widths are modulated by contemporary fluvial properties including river slope, discharge, bank strength, and bed material (DiBiase and Whipple, 2011; Dunne and Jerolmack, 2020; Leopold and Maddock, 1953), valley widths reflect erosional and aggregational histories making them more difficult to predict (May et al., 2013). In much of the OCR, valley width is found to vary with the drainage area raised to a power (Supp. Fig. S1.2) (May et al., 2013). However, in drainage basins where deep seated landslide morphology is common, the valley width vs. drainage area relationship is more scattered, though the general trend persists (May et al., 2013). Across our study area, we observe that river headwaters, where drainage areas and measured valley widths are low, are more susceptible to landslide dam formation than downstream in high drainage area rivers.

Rivers that flow through more mountainous terrain have higher landslide dam susceptibility. Clear correlations are visible in the relationship between dam susceptibility values and area averaged slope and relief (Fig. 1.10b,c). In general, higher slope and relief correspond with river headwaters, but mainstem rivers flowing through mountains also have higher dam susceptibility values. In mountainous reaches, hillslope processes such as landsliding, valley wall armouring, and debris flow sediment input control valley width (Grant and Swanson, 1995; Shobe et al., 2021). Within the OCR, valley widths are generally depressed in basins correlated to landsliding, though it depends on the stream position relative to the landslide deposit (May et al., 2013). East of the study area, on the west side of the Oregon Cascades, mountain valley morphology was shown to be strongly controlled by bedrock exposure and hillslope and tributary processes, including landsliding (Grant and Swanson, 1995). Hillslope sediment delivery is proposed to control valley width (Tofelde et al., 2022), as found for terrace edged alluvial channels. Landsliding, bedrock exposure, and hillslope sediment supply all are expected to increase with increasing slope/relief, and possibly uplift, which may keep mountainous valleys narrower (e.g., Heimsath et al., 2012; Larsen and Montgomery, 2012; Roering et al., 1999). Indeed, the locations in the OCR where we observe the highest dam susceptibility (Fig. 1.8) spatially correspond with the highest uplift and erosion rates inferred from hilltop curvature (Struble et al., 2024).

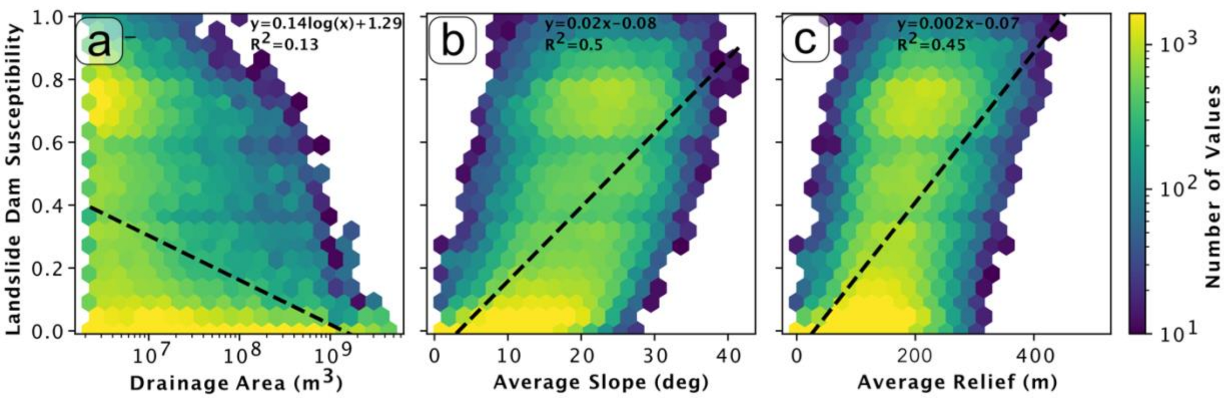

Figure 1.10: Trends of the landslide dam susceptibility values, plotted with a) river drainage area, b) average slope (mean value sampled from a 500m radius around the river point), and c) relative relief (also mean value sampled from a 500m radius around the river point). Color scale for all plots represents the number of river stretches with values corresponding to the hexbin.

Lithology also likely plays an important role in setting landscape morphology and, consequently, dam susceptibility. Figure 1.11 demonstrates a correspondence between volcanic rock and higher relief (and landslide dam susceptibility) within the northern section of the study area. This is most notably exemplified by the Tillamook Volcanics around the Wilson River basin when compared to neighbouring landscapes in marine sedimentary rocks. The high relief areas in the south of the study area do not always visually correlate with a distinct rock type, since both high and low relief regions lie in marine sedimentary rocks, though inter-rock type variations in grain size and possibly erodibility may control landsliding and relief (LaHusen and Grant, 2024). This is consistent with the findings of Schanz and Montgomery (2016) who compared basins just north of the OCR dominated by igneous bedrock, with the areas of the Nehelam river (Northern OCR Fig. 1.8) dominated by friable sedimentary rock. They found valley widths to be 2-3 times wider in the sedimentary basins and proposed that this was due to the ease of lateral erosion in those easily weathered rock types. In other regions rock type has not been identified as a primary control on valley width, for example, in the Himalaya uplift rate was found to be the largest control on valley width (Clubb et al., 2023). Uplift rates within the OCR span only a narrow range, which may allow the variations in rock type to play a key role in setting valley width, similar to their influence on hillslope form (Struble et al., 2024). For instance, more resistant lithology may inhibit lateral erosion in channels, thus promoting narrow rivers (Li et al., 2023) and also support greater landscape relief (Neely et al., 2019).

Volcanic rocks may host narrower rivers; however, they must also host large landslides to lead to the formation of landslide dams. While it may be intuitive to expect that lithology will control landslide size and that stronger rocks may form smaller landslides, in this study we find no evidence that landslides in volcanic rocks are smaller than those in other lithologies.

Lithology was included in our attempt to predict local landslide volumes with multivariate regression (Fig. S1.4 and S1.5). There are no large differences in the volume distributions of landslides based on lithology (Fig. S1.9). In fact, the lognormal mean volume for volcanic rocks (μ=4.6 in log m^3) is slightly higher than for the marine sedimentary rocks (μ=4.4 in log m^3) which make up most of the study area. It is possible that the landslide frequency varies across lithologies, however tackling this question is beyond the scope of this work (and capabilities of the incomplete inventories available). Our analysis indirectly accounts for relative frequency by using the state-wide landslide susceptibility map which incorporates lithology (Burns et al., 2016). This map and other susceptibility maps that incorporate lithology do not show a decrease in landslide susceptibility in regions of volcanic rocks (Burns et al., 2016; Sharifi-Mood et al., 2017). Further research could inform how geology controls possible dam forming landslides. For now, we conclude that (at a regional scale) lithology is not the primary control of landslide character but does likely act as an important control on valley widths, and consequently landslide dam susceptibility.

The distribution of landslide dam susceptibilities found in this study are generally similar to other landslide dam susceptibility studies. Studies in New Zealand's Southern Alps (McMeckin, 2022), Italy's Arno Basin (Tacconi Stefanelli et al., 2020), and Central Asia (Tacconi Stefanelli et al., 2023), generally predict a much higher percentage of river stretches with low landslide dam hazard than with intermediate or high hazard. McMeckin (2022) found roughly 28% of the points in the catchments they studied at risk, which is comparable to the 36% of points above dam potential of 0.35 in our study. In both the Arno Basin and Central Asia, around 30 to 40 percent of the rivers were associated with moderate, high, and very high damming susceptibility (Tacconi Stefanelli et al., 2020, 2023). All studies show a clear relationship between mountainous areas with high relief and areas with higher landslide dam susceptibility. It's unclear what the variability of results may look like if this methodology were applied to a region nearly entirely within high relief slopes such as the Himalaya. We suggest that landslide dams are more likely to occur close to river headwaters, along stretches of river that cut through higher topography, and through resistant rock types. The location of the steep terrain and narrow valleys is likely controlled by lithology in the OCR but may have other controls (such as uplift rate) globally.

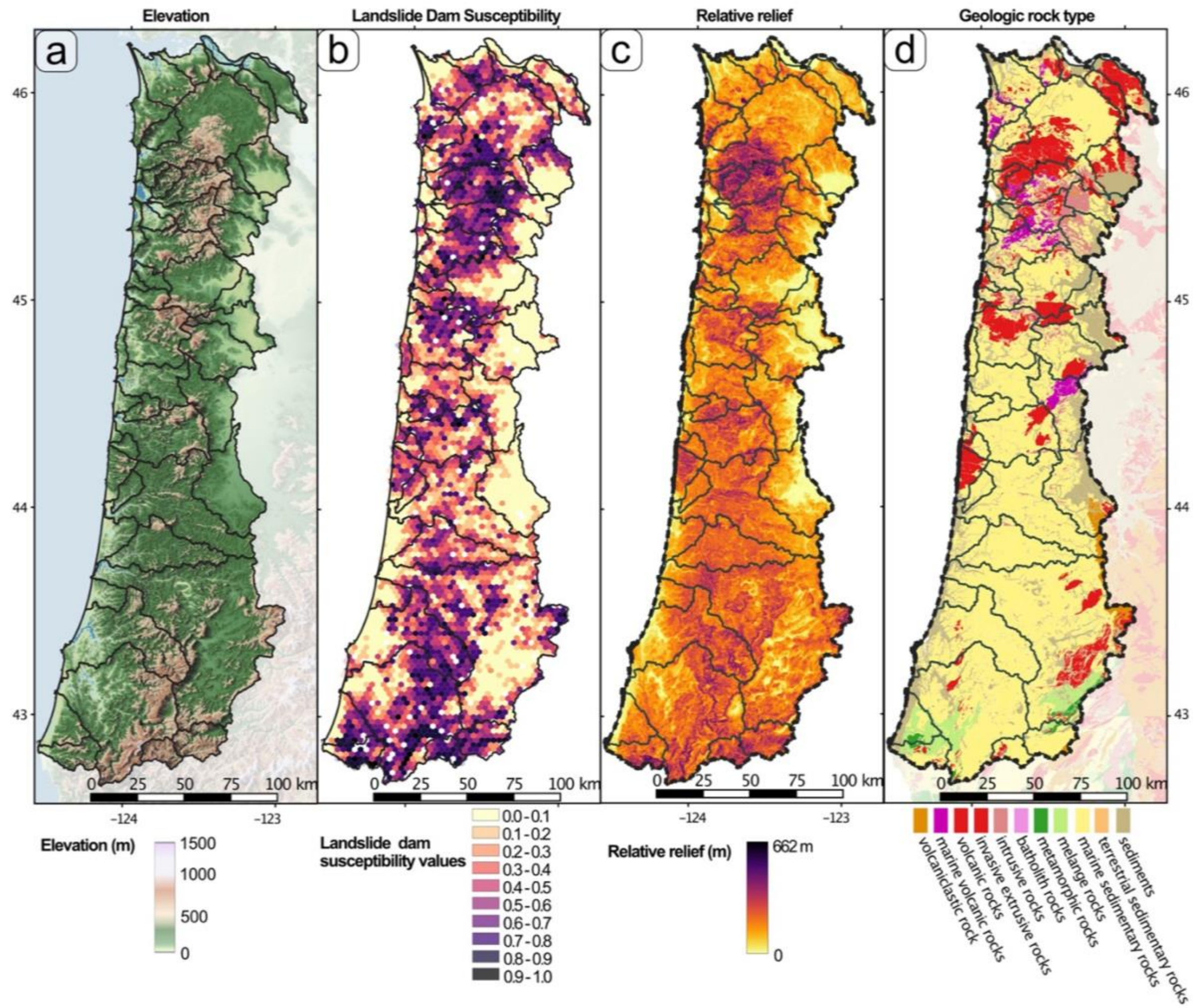

Figure 1.11: a) elevation b) dam potential, c) relative relief, and d) rock type for the study area presented side by side to showcase correlations. Dam potential values are averaged over each ~3km across or 7.5km^2 area diameter hex bin. Relative relief values are calculated over a 500 m moving window on the USGS 1/3 arc second (10m) 3DEP program DEM (US. Geological Survey, 2023). Rock type values are from the Oregon Geologic Data Compilation (OGDC-6) by DOGAMI.

1.5.3 Landslide dam hazards in the Oregon Coast Range

The potential for landslide dam formation is present and widespread across the OCR. Roughly one third of the river points have dam susceptibility values greater than 0.35, the threshold placed to define potential dam sites (visible points in Fig. 1.9). These results are consistent with the large number of landslide dam deposits (>200) observed throughout the study area (Struble et al., 2021) and suggest that flooding associated with landslide impounded riverways is a hazard worthy of consideration in community planning.

Fortunately, most of the river stretches with high potential for dam formation would likely hold small lakes (<10^4 m^3) (Fig. 1.12). Rivers with high landslide susceptibility values can be dammed by smaller landslides. Our lake estimate procedure adjusts the slide volume based on the minimum damming slide volume (V^{50}) for the river stretch, therefore we predict smaller lake volumes for narrower river valleys. We consider our predicted lake volumes (yellow line in Fig. 1.10) low when compared to a dataset of historic landslide dam outburst floods (Costa and Schuster, 1991), where lake volumes of around 1 million cubic meters are the minimum recorded lake volumes for catastrophic outburst floods (black dots in Fig. 1.12b). Smaller landslide dam lakes are still capable of causing damage and may still require a swift mitigation response, (Costa and Schuster, 1991), however the 1 million cubic meters mark provides a good approximation of extreme impact potential.

Landslide dam disasters are usually triggered by exceptionally large landslides (Costa and Schuster, 1991; Fan et al., 2020). Two examples of past landslide dams which occurred in the Pacific Northwest, the Oso landslide and the Bonneville landslide dam, dammed rivers in wide valleys which would have low damability values ~0.1 and ~0.01 respectively (Iverson et al., 2015; Pierson et al., 2016). These were rare and large landslides, lying at the 98th percentile (Oso) and 99.9th percentile (Bonneville) of the SLIDO volume distribution. Large landslides like these are also capable of damming relatively larger rivers with lower gradients that can lead to rapid lake filling and extensive upstream impacts.

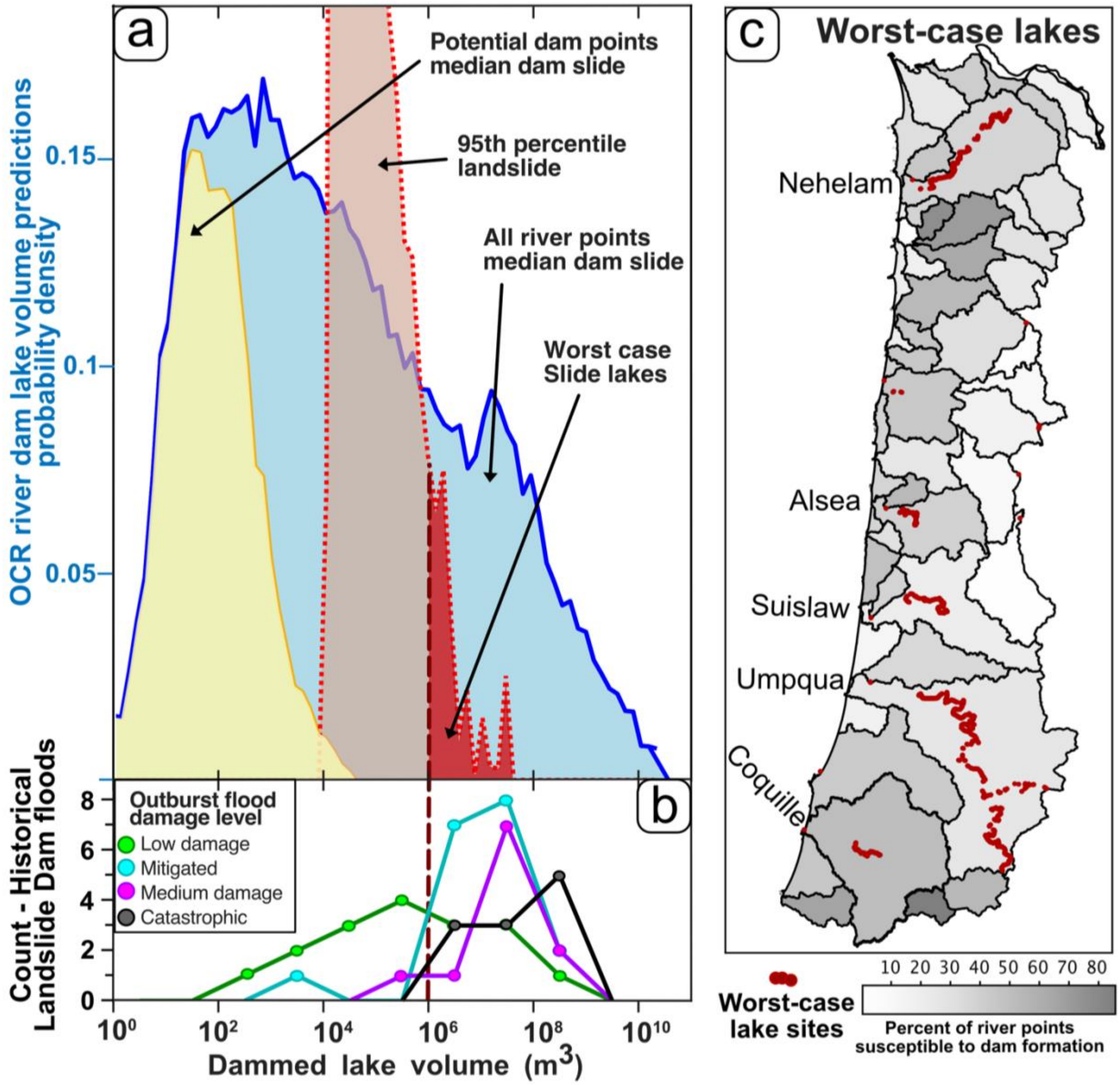

Figure 1.12: a) Predicted lake volumes for landslide dams at OCR river points compared with b) the volumes of historical landslide dam lakes. a) Blue line represents dam volumes predicted for every river point, calculated with the minimum damming landslide volume (V_{50} EQ. 5). The yellow line represents the same dataset as the blue line, but limited to only potential dam sites where landslide dam susceptibility is greater than 0.35 (Plotted in Fig. 1.7). Light red dashed line represents lake volumes estimated using the 95th percentile volume ($3x10^6$ m^3) landslide, and limited to points where that large slide leads to damability values > 0.5, and dark red shaded area represents the worst-case lakes where the 95th percentile landslide might impound a lake greater than 1 million cubic meters. b) Lines with dots represent a subset of the data presented in Costa and Schuster (1991) where dam lake volumes are recorded and outburst flood effects are noted and are colored by impact: green = little to low damage, blue = engineering mitigation took place, pink = medium damage, and black = catastrophic damage. c) maps the locations of the worst case lakes in a) over the catchments shaded by percent of river points that are above the dam potential threshold, same as Fig. 1.9.

If we estimate landslide dam lake formations with a worst-case assumption of a landslide with a volume corresponding to the 95th percentile of the SLIDO inventory ($3x10^6$ m^3) the magnitude and location of dams with the greatest potential impacts shifts dramatically. This worst-case landslide would likely (damability>0.5) dam 66% of the river stretches, and possibly (damability>0.1) dam 88%. The estimated lake volumes at those likely dammed sites increase significantly as well (red dashed line Fig. 1.12a). In a few rivers, the 95th percentile landslide would likely dam the river and could impound a lake exceeding the 1 million cubic meters associated with historic catastrophic outburst floods (Fig. 1.12a). The corresponding worst-case lakes (Fig. 1.12c) are primarily in the largest rivers in the study area and are not correlated to the catchments with the highest landslide dam susceptibility values. The mismatch between the rivers where landslide dams may be the most likely to form, and those where the impacts could be the greatest, presents a mitigation planning challenge worthy of further study.

An obvious next step would be to improve on this analysis through more detailed assessments within the most hazardous catchments. This could bypass some of the simplifications made to take advantage of regional datasets. Local lake volume estimates could be improved using local topography rather than a scaling relationship not calibrated on fluvial valleys (Argentin et al., 2021; Hergarten et al., 2023). Local evaluations may also be improved by valley specific geotechnical investigations to characterize local landslide susceptibilities as well as constrain landslide volumes and possible runout distances. For example, landslide patterns within the study area are known to be controlled by sub geologic unit lithologic properties (Roering et al., 2005; LaHusen and Grant, 2024). That level of detail is beyond the scope of this regional analysis.

Ultimately the risks to populations posed by landslide dams are controlled by the location of the landslide dam formation, the size and stability of the dam, the size of the impounded lake, and the exposure of upstream and downstream people and infrastructure. The scope of this study was to identify the locations where landslide dams may be most likely to occur, and place initial estimates on the magnitude of the impacts. Our results can help mitigation planning, prioritize valleys for localized detailed analysis, and order initial inventory scouting in the case of a widespread landslide triggering event. Future work to identify community exposure, investigate the landslide dam susceptibility upstream of those communities, and simulate outburst floods within those valleys, would extend the value of landslide dam susceptibility analyses for decision makers. How landslide dam hazard analysis work is continued and presented should represent a cross section of what is scientifically possible and be informed by what products end users need (e.g., Barnhart et al., 2023).

1.6 Conclusions

In this study, we refined a methodology used to estimate landslide dam susceptibility at a regional scale in the Oregon Coast Range (OCR). As part of this workflow, we present a new methodology for fitting a dam/non-dam inventory to derive a probabilistic damability function, which can be used to predict landslide dam likelihood given landslide volume and valley width. We show that landslide volume is not always predictable using data driven models including local geomorphic and geologic factors. Our case study demonstrates that a log-normal distribution of landslide volumes and our valley width measurement algorithm can be successfully used to assess landslide dam susceptibility using a damability function. Our methods separate sites with known landslide dams from all river sites with an ROC area under the curve of 0.834. We also demonstrate how damability function derived damability values can be used in conjunction with landslide susceptibility or impounded lake volume estimates to better characterize and visualize landslide dam formation likelihoods and magnitudes (Fig. 1.8-1.9). The damability function approach is flexible to the input of new data and can be recalibrated by existing or new inventories for use in other regions globally.

When applied to the OCR, we find that dam susceptibility correlates with drainage area, mountainous terrain, and lithology. High landslide dam susceptibility is widespread across the OCR, where roughly one-third of the river stretches have landslide dam susceptibility values above the dam potential threshold value (0.35). In most of these susceptible river stretches, we estimate that landslide dams would impound relatively small lakes that are generally less dangerous. However, exceptionally large landslides could dam most of the OCR rivers and impound lakes large enough for catastrophic outburst flooding in some rivers. These results show that landslide dam hazards could be significant in the Pacific Northwest. If a large, widespread landslide triggering event, such as a subduction zone earthquake, were to occur, we expect that landslide dams may form in the OCR, and the chances of a landslide dam leading to a catastrophic outburst flood are non-negligible.

1.7 Code Availability

The code used to measure valley width is openly available at https://github.com/PMonroeMorgan/ElevationThresholdValleyWidth.git Morgan (2026) 10.5281/zenodo.18992083

1.8 Data Availability

We provide supplemental data files including the dam/non-dam inventory used to fit the damability function, and the analysis results at all river points here: Paul M. Morgan, alex r.r. grant, and Alison R. Duvall, (2026) Landslide Dam Data and Susceptibility Estimates in the Oregon Coast Range: U.S. Geological Survey data release, https://doi.org/10.5066/P14SIP44. Much of the data used in this study is publicly available and provided by the Oregon Department of Geology and Mineral Industries (DOGAMI) including: the Lidar data (https://www.oregon.gov/dogami/lidar/Pages/index.aspx), geologic map data (https://www.oregon.gov/dogami/geologicmap/Pages/index.aspx), and landslide inventories (https://www.oregon.gov/dogami/slido/Pages/data.aspx).

1.9 Disclaimer

Any use of trade, firm, or product names is for descriptive purposes only and does not imply endorsement by the U.S. Government.

1.10 Acknowledgements

The authors gratefully acknowledge funding support from National Science Foundation (NSF) Grant Number 2103713 to Duvall. We thank N. Calhoun and B. Burns for comments and recommendations in the early stages of this work. The manuscript was improved by comprehensive reviews by internal U.S. Geological Survey researchers A. Dunham and S. Ahrendt, by two anonymous reviewers, and P. Bürgi. Any use of trade, firm, or product names is for descriptive purposes only and does not imply endorsement by the U.S. Government.

1.11 Financial Support

National Science Foundation grant ICER-2103713.

1.12 References

Alvioli, M., Marchesini, I., Reichenbach, P., Rossi, M., Ardizzone, F., Fiorucci, F., and Guzzetti, F.: Automatic delineation of geomorphological slope units with r.slopeunits v1.0 and their optimization for landslide susceptibility modeling, Geosci. Model Dev., 9, 3975–3991, https://doi.org/10.5194/gmd-9-3975-2016, 2016.
Argentin, A. L., Robl, J., Prasicek, G., Hergarten, S., Hölbling, D., Abad, L., and Dabiri, Z.: Controls on the formation and size of potential landslide dams and dammed lakes in the Austrian Alps, Nat. Hazards Earth Syst. Sci., 21, 1615–1637, https://doi.org/10.5194/nhess-21-1615-2021, 2021.
Barnhart, K. R., Romero, V. Y., and Clifford, K. R.: User needs assessment for postfire debris-flow inundation hazard products, US Geol. Surv. Open-File Rep., 2023, https://doi.org/10.3133/ofr20231025, 2023.
Bellugi, D. G., Milledge, D. G., Cuffey, K. M., Dietrich, W. E., and Larsen, L. G.: Controls on the size distributions of shallow landslides, Proc. Natl. Acad. Sci. U. S. A., 118, https://doi.org/10.1073/pnas.2021855118, 2021.
Bonnard, C.: Technical and Human Aspects of Historic Rockslide-Dammed Lakes and Landslide Dam Breaches, 1, 101–122, https://doi.org/10.1007/978-3-642-04764-0_3, 2011.
Bryce, E., Lombardo, L., van Westen, C., Tanyas, H., and Castro-Camilo, D.: Unified landslide hazard assessment using hurdle models: a case study in the Island of Dominica, Stoch. Environ. Res. Risk Assess., 36, 2071–2084, https://doi.org/10.1007/s00477-022-02239-6, 2022.
Burns, W. J. and Madin, I. P.: Protocol for Inventory MappIng of landslIde deposIts from lIght detectIon and rangIng (LIDAR) Imagery SpecIal Paper 42, Oregon Dep. Geol. Miner. Ind., 2009.
Burns, W. J., Mickelson, K. A., and Madin, I. P.: Landslide Susceptibility Overview Map of Oregon, 2016.
Clubb, F. J., Weir, E. F., and Mudd, S. M.: Continuous measurements of valley floor width in mountainous landscapes, Earth Surf. Dyn. Discuss., 2022, 1–27, 2022.
Clubb, F. J., Mudd, S. M., Schildgen, T. F., van der Beek, P. A., Devrani, R., and Sinclair, H. D.: Himalayan valley-floor widths controlled by tectonically driven exhumation, Nat. Geosci., 16, 739–746, https://doi.org/10.1038/s41561-023-01238-8, 2023.
Corominas, J.: The angle of reach as a mobility index for small and large landslides., Can. Geotech. J., 260–271, 1996.
Costa, J. E. and Schuster, R. L.: Formation and Failure of Natural Dams., Bull. Geol. Soc. Am., 100, 1054–1068, https://doi.org/10.1130/0016-7606(1988)100<1054:TFAFON>2.3.CO;2, 1988.
Costa, J. E. and Schuster, R. L.: Documented historical landslide dams from around the world, Open-File Rep. (United States Geol. Surv., 494, 1991.
Dai, F. C., Lee, C. F., Deng, J. H., and Tham, L. G.: The 1786 earthquake-triggered landslide dam and subsequent dam-break flood on the Dadu River, southwestern China, Geomorphology, 65, 205–221, https://doi.org/10.1016/j.geomorph.2004.08.011, 2005.

Dai, L., Fan, X., Jansen, J. D., and Xu, Q.: Landslides and fluvial response to landsliding induced by the 1933 Diexi earthquake, Minjiang River, eastern Tibetan Plateau, Landslides, 3011–3025, https://doi.org/10.1007/s10346-021-01717-2, 2021.
Dal Sasso, S. F., Sole, A., Pascale, S., Sdao, F., Bateman Pinzòn, A., and Medina, V.: Assessment methodology for the prediction of landslide dam hazard, Nat. Hazards Earth Syst. Sci., 14, 557–567, https://doi.org/10.5194/nhess-14-557-2014, 2014.
Densmore, A. L. and Hovius, N.: Topographic fingerprints of bedrock landslides, Geology, 28, 371–374, https://doi.org/10.1130/0091-7613(2000)028<0371:TFOBL>2.3.CO;2, 2000.
Dettinger, M. D., Ralph, F. M., and Rutz, J. J.: Empirical return periods of the most intense vapor transports during historical atmospheric river landfalls on the U.S. West Coast, J. Hydrometeorol., 19, 1363–1377, https://doi.org/10.1175/JHM-D-17-0247.1, 2018.
DiBiase, R. A. and Whipple, K. X.: The influence of erosion thresholds and runoff variability on the relationships among topography, climate, and erosion rate, J. Geophys. Res. Earth Surf., 116, 1–17, https://doi.org/10.1029/2011JF002095, 2011.
Duncan, J. M., Fleming, R. W., Patton, F. D., and U.S. Geological Survey: Report of the Thistle Slide Committee to State of Utah, Department of Natural Resources, Division of Water Rights, US Geol. Surv. Open-File Rep., 1986.
Dunne, K. B. J. and Jerolmack, D. J.: What sets river width?, Sci. Adv., 6, 1–8, https://doi.org/10.1126/sciadv.abc1505, 2020.
Ermini, L. and Casagli, N.: Prediction of the behaviour of landslide dams using a geomorphological dimensionless index, Earth Surf. Process. Landforms, 28, 31–47, https://doi.org/10.1002/esp.424, 2003.
Fan, X., Scaringi, G., Korup, O., West, A. J., van Westen, C. J., Tanyas, H., Hovius, N., Hales, T. C., Jibson, R. W., Allstadt, K. E., Zhang, L., Evans, S. G., Xu, C., Li, G., Pei, X., Xu, Q., and Huang, R.: Earthquake-Induced Chains of Geologic Hazards: Patterns, Mechanisms, and Impacts, Rev. Geophys., 57, 421–503, https://doi.org/10.1029/2018RG000626, 2019.
Fan, X., Dufresne, A., Siva Subramanian, S., Strom, A., Hermanns, R., Tacconi Stefanelli, C., Hewitt, K., Yunus, A. P., Dunning, S., Capra, L., Geertsema, M., Miller, B., Casagli, N., Jansen, J. D., and Xu, Q.: The formation and impact of landslide dams – State of the art, Earth-Science Rev., 203, 103116, https://doi.org/10.1016/j.earscirev.2020.103116, 2020.
Froude, M. J. and Petley, D. N.: Global fatal landslide occurrence from 2004 to 2016, Nat. Hazards Earth Syst. Sci., 18, 2161–2181, https://doi.org/10.5194/nhess-18-2161-2018, 2018.
Grant, A. R. R., Struble, W. T., and LaHusen, S. R.: Limits to coseismic landslides triggered by Cascadia Subduction Zone earthquakes, Geomorphology, 418, 108477, https://doi.org/10.1016/j.geomorph.2022.108477, 2022.
Grant, G. E. and Swanson, F. J.: Morphology and processes of valley floors in mountain streams, Western Cascades, Oregon, 83–101, https://doi.org/10.1029/GM089p0083, 1995.
Heimsath, A. M., DiBiase, R. A., and Whipple, K. X.: Soil production limits and the transition to bedrock-dominated landscapes, Nat. Geosci., 5, 210–214, https://doi.org/10.1038/ngeo1380, 2012.
Hergarten, S., Argentin, A., Prasicek, G., and Daniel, H.: The scaling of landslide-dammed lakes, 228, https://doi.org/10.1016/j.gloplacha.2023.104190, 2023.
Hilley, G. E., Baden, C. W., Dobbs, S. C., Plante, Z., Sare, R., and Steelquist, A. T.: A Curvature-Based Method for Measuring Valley Width Applied to Glacial and Fluvial Landscapes, J. Geophys. Res. Earth Surf., 125, 1–16, https://doi.org/10.1029/2020JF005605, 2020.
Iverson, R. M., George, D. L., Allstadt, K., Reid, M. E., Collins, B. D., Vallance, J. W., Schilling, S. P., Godt, J. W., Cannon, C. M., Magirl, C. S., Baum, R. L., Coe, J. A., Schulz, W. H., and Bower, J. B.: Landslide mobility and hazards: Implications of the 2014 Oso disaster, Earth Planet. Sci. Lett., 412, 197–208, https://doi.org/10.1016/j.epsl.2014.12.020, 2015.
Korup, O. and Tweed, F.: Ice, moraine, and landslide dams in mountainous terrain, Quat. Sci. Rev., 26, 3406–3422, https://doi.org/10.1016/j.quascirev.2007.10.012, 2007.
LaHusen, S. R. and Grant, A. R. R.: Complex landslide patterns explained by local intra-unit variability of stratigraphy and structure: Case study in the Tyee Formation, Oregon, USA, Eng. Geol., 329, 107387, https://doi.org/10.1016/j.enggeo.2023.107387, 2024.
LaHusen, S. R., Duvall, A. R., Booth, A. M., Grant, A., Mishkin, B. A., Montgomery, D. R., Struble, W., Roering, J. J., and Wartman, J.: Rainfall triggers more deep-seated landslides than Cascadia earthquakes in the Oregon Coast Range, USA, Sci. Adv., 6, https://doi.org/10.1126/sciadv.aba6790, 2020.

Lane, J. W.: Relations between geology and mass movement features in a part of the East Fork Coquille River Watershed, Southern Coast Range, Oregon, 855, 115, 1987.
Larsen, I. J. and Montgomery, D. R.: Landslide erosion coupled to tectonics and river incision, Nat. Geosci., 5, 468–473, https://doi.org/10.1038/ngeo1479, 2012.
Larsen, I. J., Montgomery, D. R., and Korup, O.: Landslide erosion controlled by hillslope material, Nat. Geosci., 3, 247–251, https://doi.org/10.1038/ngeo776, 2010.
Leopold, L. B. and Maddock, T.: The hydraulic geometry of stream channels and some physiographic implications, US Gov. Print. Off., Vol. 252, 1953.
Li, T., Venditti, J. G., and Sklar, L. S.: Steady-State Bedrock Channel Width, Geophys. Res. Lett., 50, 1–10, https://doi.org/10.1029/2023GL105344, 2023.
Lombardo, L., Tanyas, H., Huser, R., Guzzetti, F., and Castro-Camilo, D.: Landslide size matters: A new data-driven, spatial prototype, Eng. Geol., 293, https://doi.org/10.1016/j.enggeo.2021.106288, 2021.
May, C., Roering, J., Eaton, L. S., and Burnett, K. M.: Controls on valley width in mountainous landscapes: The role of landsliding and implications for salmonid habitat, Geology, 41, 503–506, https://doi.org/10.1130/G33979.1, 2013.
McMeckin, J.: Landslide Dam Hazard Modelling in the West Coast Region, New Zealand, 1–23, 2022.
Medwedeff, W. G., Clark, M. K., Zekkos, D., and West, A. J.: Characteristic landslide distributions: An investigation of landscape controls on landslide size, Earth Planet. Sci. Lett., 539, 116203, https://doi.org/10.1016/j.epsl.2020.116203, 2020.
Meunier, P., Hovius, N., and Haines, J. A.: Topographic site effects and the location of earthquake induced landslides, Earth Planet. Sci. Lett., 275, 221–232, https://doi.org/10.1016/j.epsl.2008.07.020, 2008.
Montgomery, D. R., Schmidt, K. M., Dietrich, W. E., and McKean, J.: Instrumental record of debris flow initiation during natural rainfall: Implications for modeling slope stability, J. Geophys. Res. Earth Surf., 114, 1–16, https://doi.org/10.1029/2008JF001078, 2009.
Moreno, M., Steger, S., Tanyas, H., and Lombardo, L.: Modeling the size of co-seismic landslides via data-driven models: the Kaikōura's example, Eng. Geol., 320, 107121, https://doi.org/10.1016/j.enggeo.2023.107121, 2022.
Morgan, P. M. PMonroeMorgan/ElevationThresholdValleyWidth: ElevationThresholdValleyWidthv1.0 (v1.0). Zenodo. https://doi.org/10.5281/zenodo.18992083, 2026
Neely, A. B., DiBiase, R. A., Corbett, L. B., Bierman, P. R., and Caffee, M. W.: Bedrock fracture density controls on hillslope erodibility in steep, rocky landscapes with patchy soil cover, southern California, USA, Earth Planet. Sci. Lett., 522, 186–197, https://doi.org/10.1016/j.epsl.2019.06.011, 2019.
Pierson, T. C., Evarts, R. C., and Bard, J. A.: Landslides in the western Columbia Gorge, Skamania County, Washington, USGS Sci. Investig. Map, 3358, 25, 2016.
Pollock, W.: A Framework for Regional Scale Quantitative Landslide Risk Analysis, Univ. Washingt Diss., 2020.
Qiu, H., Cui, P., Regmi, A. D., Hu, S., Zhang, Y., and He, Y.: Landslide distribution and size versus relative relief (Shaanxi Province, China), Bull. Eng. Geol. Environ., 77, 1331–1342, https://doi.org/10.1007/s10064-017-1121-5, 2018.
Riley, S. J., DeGloria, S. D., and Elliot, R.: Index that quantifies topographic heterogeneity., 1999.
Roering, J. J., Kirchner, J. W., and Dietrich, W. E.: Evidence for nonlinear, diffusive sediment transport on hillslopes and implications for landscape morphology, Water Resour. Res., 35, 853–870, https://doi.org/10.1029/1998WR900090, 1999.
Roering, J. J., Kirchner, J. W., and Dietrich, W. E.: Characterizing structural and lithologic controls on deep-seated landsliding: Implications for topographic relief and landscape evolution in the Oregon Coast Range, USA, Bull. Geol. Soc. Am., 117, 654–668, https://doi.org/10.1130/B25567.1, 2005.
Sappington, J. M., Longshore, K. M., and Thompson, D. B.: Quantifying Landscape Ruggedness for Animal Habitat Analysis: A Case Study Using Bighorn Sheep in the Mojave Desert, J. Wildl. Manage., 71, 1419–1426, https://doi.org/10.2193/2005-723, 2007.
Sattar, A. and Konagai, K.: Recent Landslide Damming Events and Their Hazard Mitigation Strategies, Adv. Geotech. Earthq. Eng. - Soil Liq. Seism. Saf. Dams Monum., https://doi.org/10.5772/28044, 2012.
Schanz, S. A. and Montgomery, D. R.: Lithologic controls on valley width and strath terrace formation, Geomorphology, 258, 58–68, https://doi.org/10.1016/j.geomorph.2016.01.015, 2016.
Schwanghart, W. and Scherler, D.: Short Communication: TopoToolbox 2 - MATLAB-based software for topographic analysis and modeling in Earth surface sciences, Earth Surf. Dyn., 2, 1–7, https://doi.org/10.5194/esurf-2-1-2014, 2014.

Sharifi-Mood, M., Olsen, M. J., Gillins, D. T., and Mahalingam, R.: Performance-based, seismically-induced landslide hazard mapping of Western Oregon, Soil Dyn. Earthq. Eng., 103, 38–54, https://doi.org/10.1016/j.soildyn.2017.09.012, 2017.
Shobe, C. M., Turowski, J. M., Nativ, R., Glade, R. C., Bennett, G. L., and Dini, B.: The role of infrequently mobile boulders in modulating landscape evolution and geomorphic hazards, Earth-Science Rev., 220, 103717, https://doi.org/10.1016/j.earscirev.2021.103717, 2021.
Stark, C. P. and Hovius, N.: The characterization of landslide size distributions, Geophys. Res. Lett., 28, 1091–1094, https://doi.org/10.1029/2000GL008527, 2001.
Struble, W. T., Roering, J. J., Black, B. A., Burns, W. J., Calhoun, N., and Wetherell, L.: Dendrochronological dating of landslides in western Oregon: Searching for signals of the Cascadia A.D. 1700 earthquake, Bull. Geol. Soc. Am., 132, 1775–1791, https://doi.org/10.1130/B35269.1, 2020.
Struble, W. T., Roering, J. J., Burns, W. J., Calhoun, N. C., Wetherell, L. R., and Black, B. A.: The Preservation of Climate-Driven Landslide Dams in Western Oregon, J. Geophys. Res. Earth Surf., 126, 1–25, https://doi.org/10.1029/2020JF005908, 2021.
Struble, W. T., Clubb, F. J., and Roering, J. J.: Regional-scale, high-resolution measurements of hilltop curvature reveal tectonic, climatic, and lithologic controls on hillslope morphology, Earth Planet. Sci. Lett., 647, 119044, https://doi.org/10.1016/j.epsl.2024.119044, 2024.
Tacconi Stefanelli, C., Catani, F., and Casagli, N.: Geomorphological investigations on landslide dams, Geoenvironmental Disasters, 2, https://doi.org/10.1186/s40677-015-0030-9, 2015.
Tacconi Stefanelli, C., Segoni, S., Casagli, N., and Catani, F.: Geomorphic indexing of landslide dams evolution, Eng. Geol., 208, 1–10, https://doi.org/10.1016/j.enggeo.2016.04.024, 2016.
Tacconi Stefanelli, C., Vilímek, V., Emmer, A., and Catani, F.: Morphological analysis and features of the landslide dams in the Cordillera Blanca, Peru, Landslides, 15, 507–521, https://doi.org/10.1007/s10346-017-0888-6, 2018.
Tacconi Stefanelli, C., Casagli, N., and Catani, F.: Landslide damming hazard susceptibility maps: a new GIS-based procedure for risk management, Landslides, 17, 1635–1648, https://doi.org/10.1007/s10346-020-01395-6, 2020.
Tacconi Stefanelli, C., Frodella, W., Caleca, F., Raimbekova, Z., Umuralievd, R., and Tofani, V.: Assessing Landslide Damming susceptibility in Central Asia, Nat. Hazards Earth Syst. Sci. Discuss., 2023, 1–37, 2023.
Taylor, G.: The Climate of Oregon. Climate Zone 1. Coastal Area, 1993.
Tebbens, S. F.: Landslide Scaling: A Review, Earth Sp. Sci., 7, 1–12, https://doi.org/10.1029/2019EA000662, 2020.
Tofelde, S., Bufe, A., and Turowski, J. M.: Hillslope Sediment Supply Limits Alluvial Valley Width, AGU Adv., 3, 1–20, https://doi.org/10.1029/2021AV000641, 2022.
Virtanen, P., Gommers, R., Oliphant, T. E., Haberland, M., Reddy, T., Cournapeau, D., Burovski, E., Peterson, P., Weckesser, W., Bright, J., van der Walt, S. J., Brett, M., Wilson, J., Millman, K. J., Mayorov, N., Nelson, A. R. J., Jones, E., Kern, R., Larson, E., Carey, C. J., Polat, İ., Feng, Y., Moore, E. W., VanderPlas, J., Laxalde, D., Perktold, J., Cimrman, R., Henriksen, I., Quintero, E. A., Harris, C. R., Archibald, A. M., Ribeiro, A. H., Pedregosa, F., van Mulbregt, P., Vijaykumar, A., Bardelli, A. Pietro, Rothberg, A., Hilboll, A., Kloeckner, A., Scopatz, A., Lee, A., Rokem, A., Woods, C. N., Fulton, C., Masson, C., Häggström, C., Fitzgerald, C., Nicholson, D. A., Hagen, D. R., Pasechnik, D. V., Olivetti, E., Martin, E., Wieser, E., Silva, F., Lenders, F., Wilhelm, F., Young, G., Price, G. A., Ingold, G. L., Allen, G. E., Lee, G. R., Audren, H., Probst, I., Dietrich, J. P., Silterra, J., Webber, J. T., Slavič, J., Nothman, J., Buchner, J., Kulick, J., Schönberger, J. L., de Miranda Cardoso, J. V., Reimer, J., Harrington, J., Rodríguez, J. L. C., Nunez-Iglesias, J., Kuczynski, J., Tritz, K., Thoma, M., Newville, M., Kümmerer, M., Bolingbroke, M., Tartre, M., Pak, M., Smith, N. J., Nowaczyk, N., Shebanov, N., Pavlyk, O., Brodtkorb, P. A., Lee, P., McGibbon, R. T., Feldbauer, R., Lewis, S., Tygier, S., Sievert, S., Vigna, S., Peterson, S., More, S., Pudlik, T., et al.: SciPy 1.0: fundamental algorithms for scientific computing in Python, Nat. Methods, 17, 261–272, https://doi.org/10.1038/s41592-019-0686-2, 2020.
Wells, R., Bukry, D., Friedman, R., Pyle, D., Duncan, R., Haeussler, P., and Wooden, J.: Geologic history of Siletzia, a large igneous province in the Oregon and Washington Coast Range: Correlation to the geomagnetic polarity time scale and implications for a long-lived Yellowstone hotspot, Geosphere, 10, 692–719, https://doi.org/10.1130/GES01018.1, 2014.
Whittall, J., Eberhardt, E., and McDougall, S.: Runout analysis and mobility observations for large open pit slope failures, Can. Geotech. J., 54, 373–391, https://doi.org/10.1139/cgj-2016-0255, 2017.
Wu, H., Trigg, M. A., Murphy, W., Fuentes, R., Martino, S., Esposito, C., and Marco, G.: A global - scale applicable framework of land - slide dam formation susceptibility, Landslides, https://doi.org/10.1007/s10346-024-02306-9, 2024.

Xu, Q., Fan, X. M., Huang, R. Q., and Westen, C. Van: Landslide dams triggered by the Wenchuan Earthquake, Sichuan Province, south west China, Bull. Eng. Geol. Environ., 68, 373–386, https://doi.org/10.1007/s10064-009-0214-1, 2009.
Yan, K., Zhao, T., and Liu, Y.: Experimental Investigations on the Spillway Section Shape of the Breaching Process of Landslide Dams, Int. J. Geomech., 22, 1–7, https://doi.org/10.1061/(asce)gm.1943-5622.0002360, 2022.
Yang, X., Yang, Z., Cao, S., Gao, X., and Li, S.: Key techniques for the emergency disposal of Quake lakes, Nat. Hazards, 52, 43–56, https://doi.org/10.1007/s11069-009-9350-y, 2010.
Yanites, B. J., Clark, M. K., Roering, J. J., West, A. J., Zekkos, D., Baldwin, J. W., Cerovski-, C., Gallen, S. F., Horton, D. E., Kirby, E., Leshchinsky, B. A., Mason, H. B., Moon, S., Barnhart, K. R., Booth, A., Czuba, J. A., Mccoy, S., Mcguire, L., Pfeiffer, A., and Pierce, J.: Cascading land surface hazards as a nexus in the Earth system Cascading land surface hazards as a nexus in the Earth system, 9559, https://doi.org/10.1126/science.adp9559, 2025.
Zeng, P., Wang, S., Sun, X., Fan, X., Li, T., Wang, D., Feng, B., and Zhu, X.: Probabilistic hazard assessment of landslide-induced river damming, Eng. Geol., 304, 106678, https://doi.org/10.1016/j.enggeo.2022.106678, 2022.

1.13 Supplementary material for Chapter 1

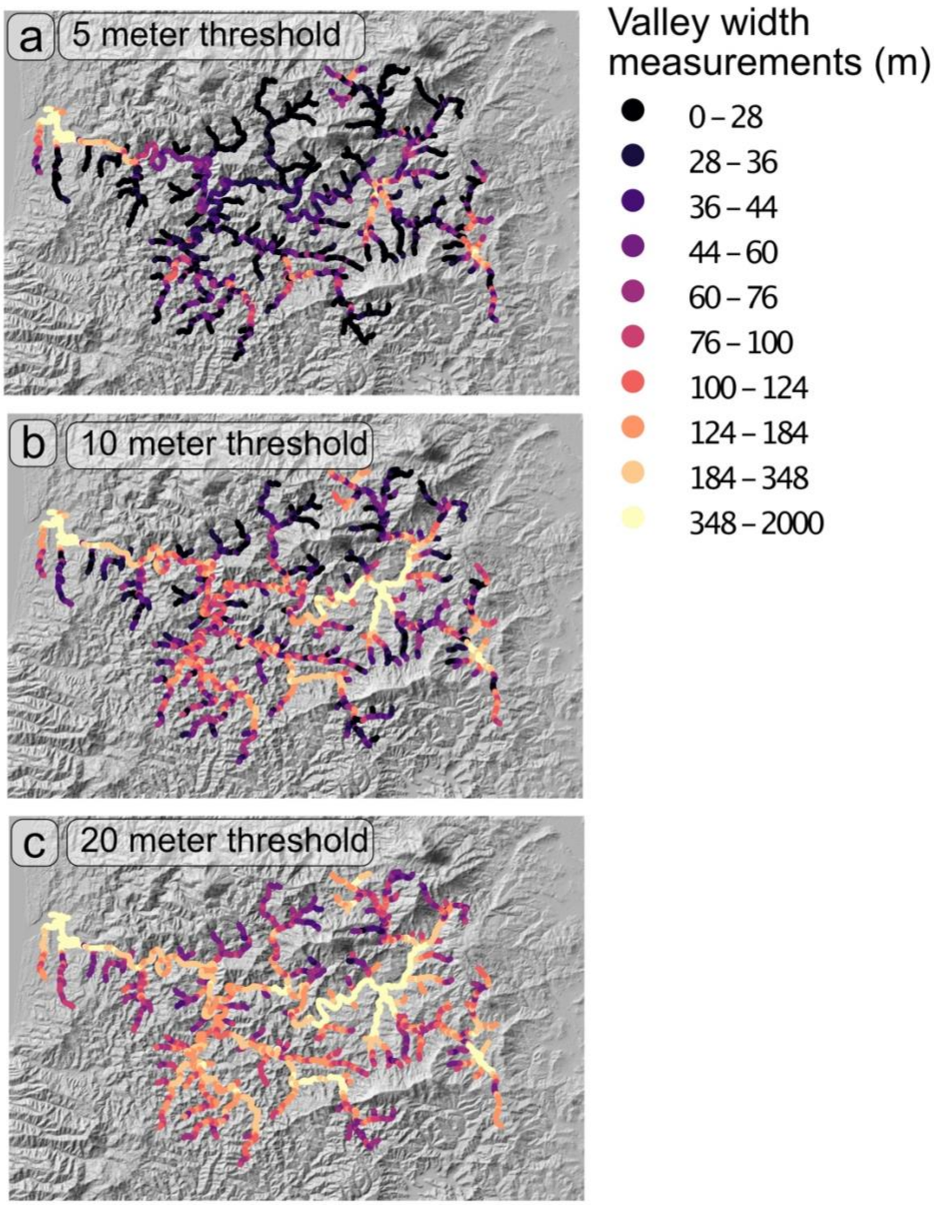

Supplementary Figure S1.1: Three plots of the Alsea River catchment, depicting valley width measurements with different elevation thresholds to define the valley edges. Note that while the absolute value of the widths does change, increasing width values with increasing threshold value, the spatial distribution does not. Locations with lower or higher width values remain constant. The elevation threshold is set to match the data from May et al. 2013 (Supp. Fig. S1.2).

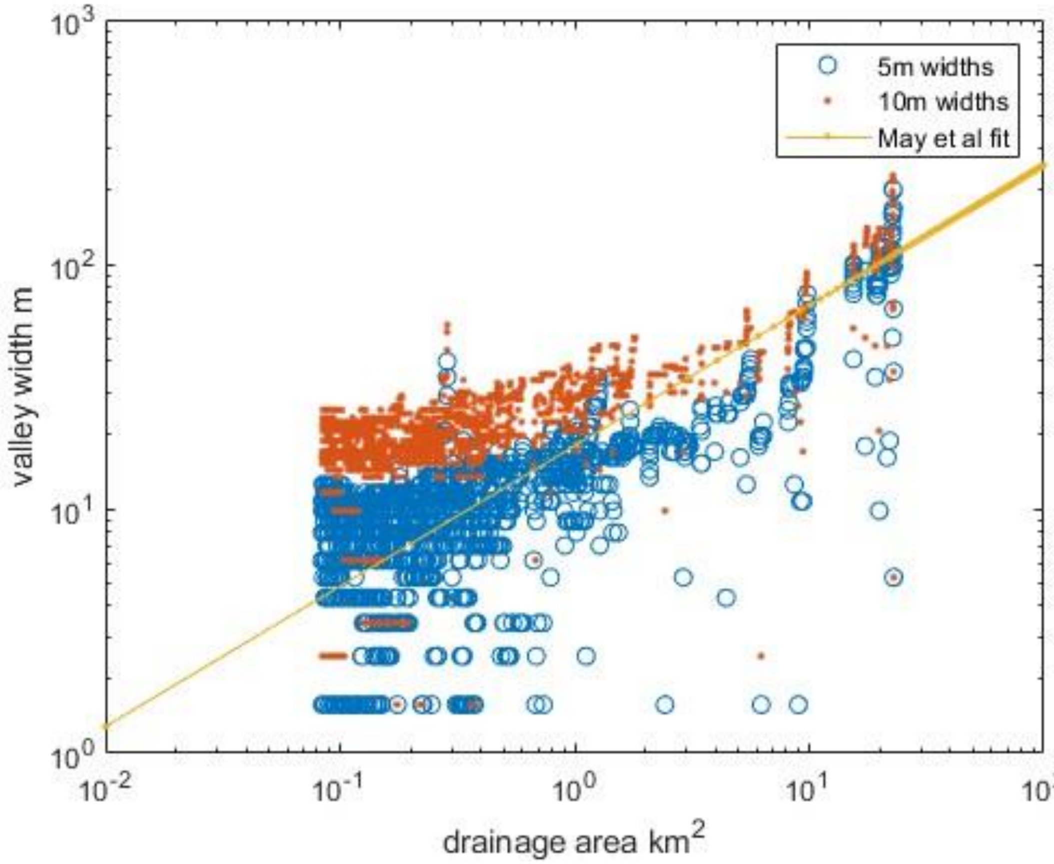

Supplemental Figure S1.2: Drainage area to valley width relationship plotted for the Harvey Creek drainage. After May et al. (2013). The yellow line is the data fit to the measurements from May et al. 2013 while the red dots and blue circles represent valley widths calculated with two different elevation thresholds. Note that the 10m threshold elevation values match the fit line better for drainage areas down to ~10 square km. McMeckin (2022) compared Topographic position index (TPI) based and threshold (slope and elevation) based methods and found both were acceptable where the methods succeeded. Most landslide dam susceptibility studies factor in some form of the river or valley geometry (Fan et al., 2020). We do not argue that the difference in valley width measurement method is important. Measuring valley width, through elevation thresholds matches intuition of blocking water flow to form lakes, though we have not explored differences between this approach and a river width only, or a morphological classification based approach.

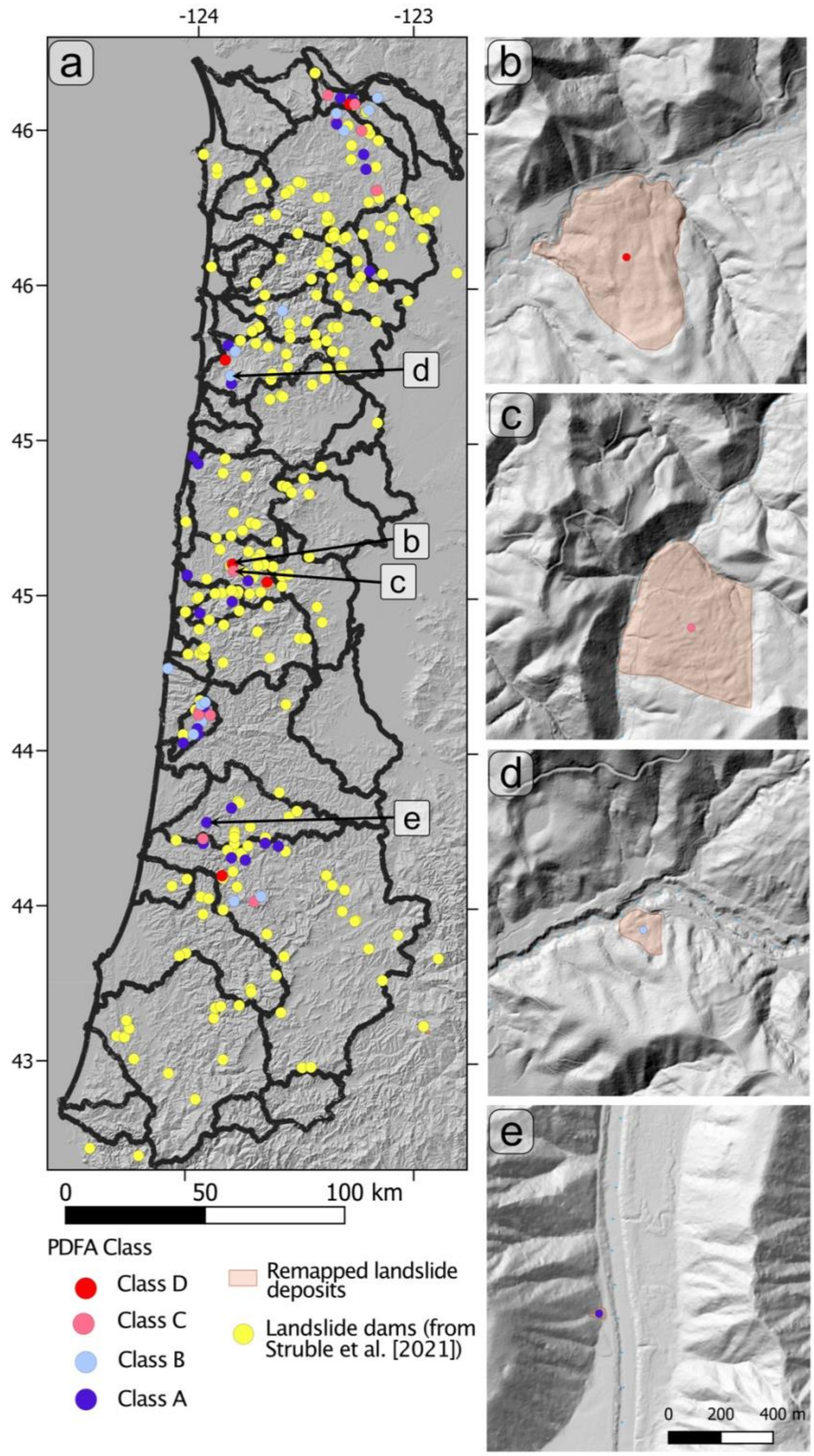

Figure S1.3: Examples of landslides within the dam/non-dam inventory used to calibrate the OCR DFD function. A) shows locations of landslide dams used for the DFD function regression. b) - e) examples of type 4 - type 1 landslides respectively.

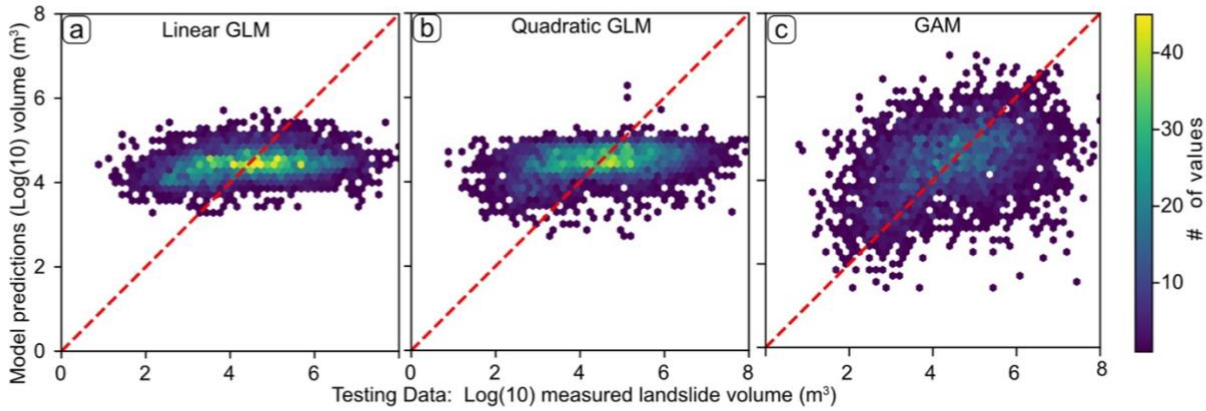

Figure S1.4: Comparison of measured landslide volumes and model predictions ultimately deemed unsuccessful. These are blind predictions of volume for the 20% of the inventory withheld from model development. a) shows the predictions from a general linear model limited to linear fits, b) shows the predictions from a general linear model predicted with quadratic fits, and c) shows the predictions from a general additive model. All models trained with slope unit extracted local parameters, for radially extracted predictor results see Supp. Fig. S5.

Predictor variable extraction technique	GAM	GLM1	GLM4
Radial mean	1.1237	0.9767	0.9546
Slope unit	0.9615	1.075	1.051

Table S1.1: Statistical regression model results presented as the IMMSE (improved minimum mean squared error).

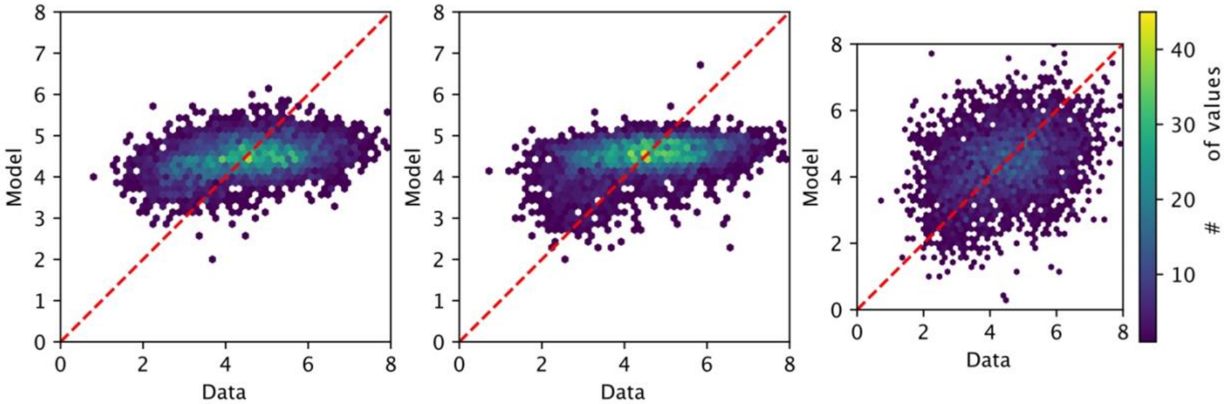

Figure S1.5: Comparison of measured landslide volumes and regression model predictions. These are blind predictions of volume for the 20% of the inventory withheld from model development. a) shows the predictions from a general linear model limited to linear fits, b) shows the predictions from a general linear model predicted with quadratic fits, and c) shows the predictions from a general additive model. As opposed to Fig. S4 these are results calculated from predictor variables extracted using a moving window with a 500 m radius. More methodological differences between this study and previous studies that may account for the differences include: The target variable in our study is individual landslides whereas Moreno et al. (2022) aggregated all landslides within a slope area, and Lombardo et al. (2021) used the maximum landslide area per slope unit. Additionally, these previous studies were limited to landslide area, whereas we use landslide volumes. The additional complexity stepping from area to volume may make a difference.

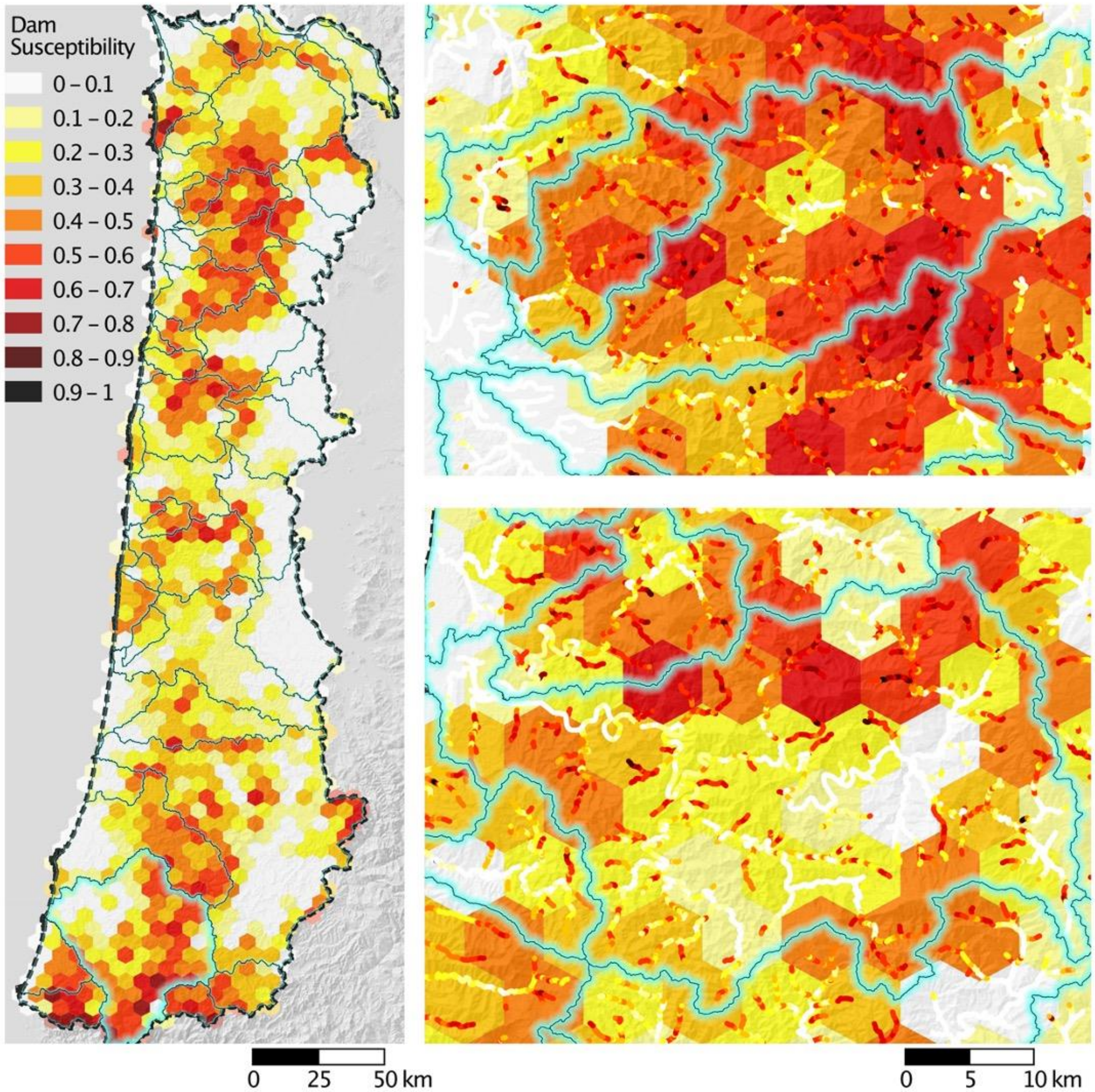

Supplemental Figure S1.6: a) Damability value estimates for the Oregon Coast Range. a) shown as averages over ~6 km across or ~30 km^2 area hexagons as well as for individual 100 m long river stretches. b) Wilson and c) Alsea catchments. Note that changes in the values is minimal between the 'damability' values plotted here and the dam susceptibility values plotted in Fig. 1.8

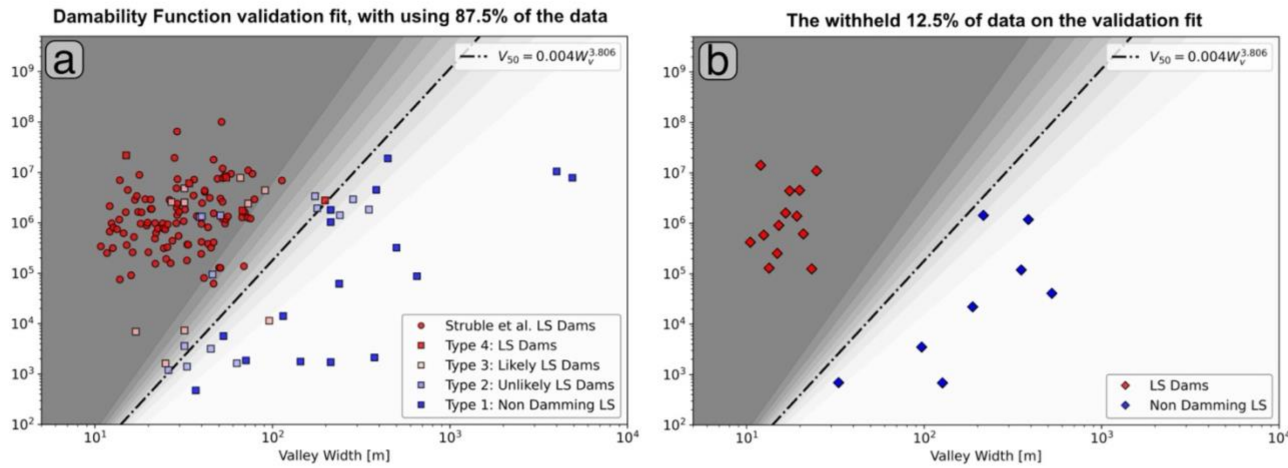

Supplementary Figure S1.7: Validation of the damability function fits. a) depicts the damability function fit to a training dataset with 12.5% of the dam forming datapoints and the dam non-forming datapoints randomly withheld. Note that the function fit is very similar to the function plotted in Fig. 6. b) depicts the withheld datapoints plotted on the validation fit from a). Note that all points lay on the matching side of the V_{50} line.

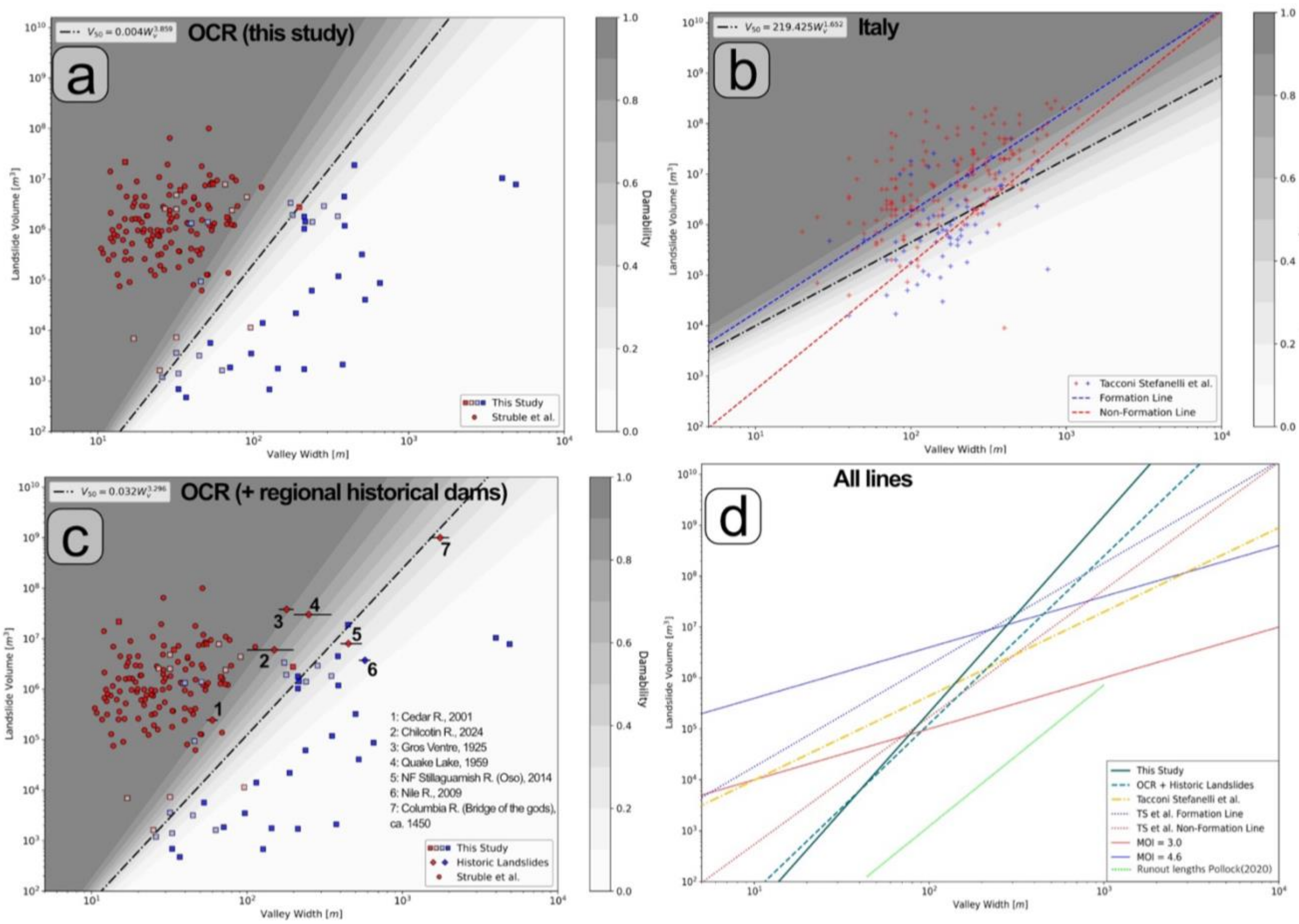

Supplementary Figure S1.8: Damability function fits for various datasets. a) is a repeat of Fig. 6, b) is the logistic damability function regression results for the landslide dam/non-dam dataset presented in (Tacconi Stefanelli et al., 2015). Also plotted are the V_{50} line of the regression damability function, and the formation and non-formation lines used in Tacconi Stefanelli et al. (2020). c) is the same as a), but with the addition of several notable recent and historic landslide dams within the Northwest US. The damability function is refit to include the notable landslides, this illustrates that the damability logistic regression is flexible to the input of new data, however the new fit is not used in our study, since the notable landslides are from outside the study area. d) has all lines in the volume valley width plot referenced in this study: dark grey is the V_{50} line from plot a) this study, dark grey dashed is the V_{50} line from plot c, note that it has a shallower slope than the line used in this study, Yellow dashed is the V_{50} line from plot b), blue and red dashed are the formation and non-formation lines used as the primary damability functions in Tacconi Stefanelli et al., (2020), solid red and blue lines represent the upper and lower edges of Morphological Obstruction Index (MOI) values claimed to mark the edges of the dam forming and non-forming domains in Tacconi Stefanelli et al., (2016), Light green dashed line represents the global regression to fit landslide volume to runout relationships of Pollock (2020), note that in this line the length scale is slide runout rather than valley width. The damability functions work better at separating the data into formation and non-formation domains than the Morphological Obstruction Index (MOI) metric numbers itself, which is calculated as the ratio between log width and log volume (Figure S4) (Carlo Tacconi Stefanelli et al., 2016). The slopes of lines defined by constant MOI values are 1 in the log-log space, which is too shallow to accurately capture the domains represented by the data. We suggest that the MOI values be rethought with an exponent added, or that only the dam formation domain functions be considered going forward.

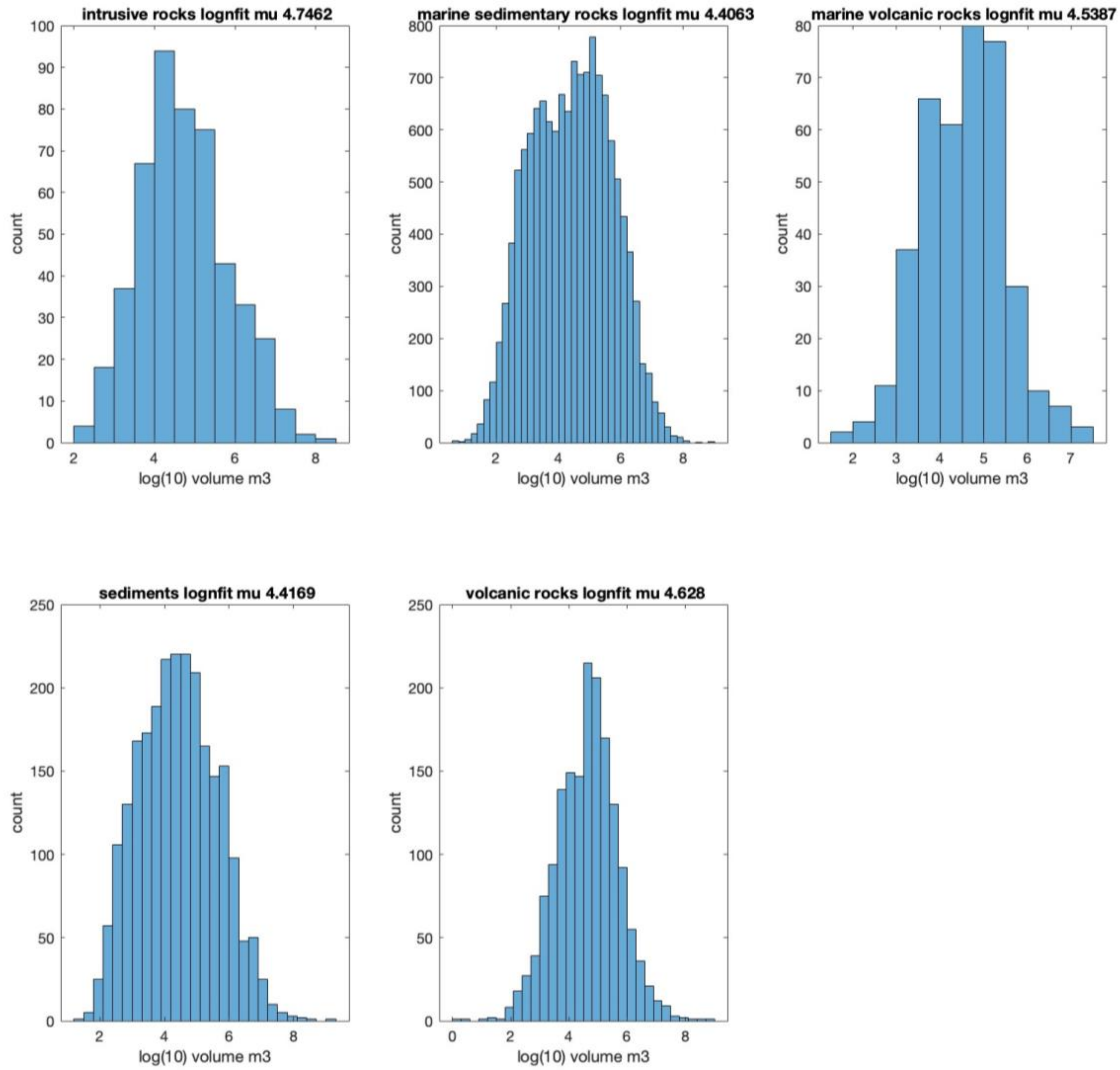

Supplementary Figure S1.9: Histograms of the SLIDO landslide log volumes (Franczyk et al. 2020) with respect to rock type. Note that the lognormal mean of the distributions is similar for all rock types. Minimum number of landslides of 200 required to be listed in this plot.

2. **Chapter 2**: SoilLandslider: A soil landsliding component for landscape evolution modeling implemented in Landlab

Abstract.
Shallow landslides influence hillslope development and sediment transport across mountainous landscapes. However, most landscape evolution models lack explicit representation of shallow landslides that fail the uppermost soil regolith layer. This study presents SoilLandslider, a module for simulating shallow soil landslides in the Landlab modelling framework, that is designed to operate at the millennial timescales required for geomorphic steady state. The module uses infinite slope stability analysis to identify susceptible terrain (incorporating soil depth and ground water table depth), and triggers landslides stochastically. When triggered, landslides propagate uphill according to local stability conditions and slope geometry, with sediment transported downslope via multiple path flow routing and deposited based on a depositional slope. We validate SoilLandslider against field observations from the Oregon Coast Range, comparing model predictions of instability locations, landslide size distributions, and the spatial pattern of erosion and deposition with mapped landslides. We demonstrate the model's utility and inform its use through numerical experiments. We demonstrate that shallow landsliding can generate landscape forms comparable to those produced by non-linear diffusion, suggesting that discrete landslides may be the primary mechanism driving non-linear transport at steep slopes. We also demonstrate how hydrologic assumptions affect long-term landscape evolution. The SoilLandslider module enables more process-based landscape evolution modelling, advancing our understanding of how discrete geomorphic mechanisms form landscapes over long timescale simulations.

2.1 Introduction

Landslides are a foundational geomorphic process that significantly influence the form and evolution of landscapes (Crozier, 2010). Landsliding accounts for some of the highest rates of erosion on hillslopes, mobilizing large volumes of sediment in steep landscapes (e.g., Broeckx et al., 2020; Hovius et al., 1997). They also act to set slopes at constant angles within threshold hillslope regimes (Korup et al., 2007; Larsen and Montgomery, 2012; Montgomery, 2001; Montgomery and Brandon, 2002). As a primary agent of hillslope erosion in upland environments, landslides deliver a majority of sediment to neighboring rivers, and thus have the capability to impact and alter fluvial systems (Fan et al., 2019, 2020; Yanites et al., 2018). Nevertheless, many of the most used numerical models of landscape evolution (LEMs) do not include explicit functions for landsliding.

LEMs are excellent tools for studying the processes that shape landscapes and how these processes interact with each other over different temporal scales (Campforts et al., 2020; Tucker and Hancock, 2010). Given the outsized role of landslides in mountainous landscape evolution, equations that simulate landslides should be included in LEMs. Moreover, to map the full impact of landslides on hillslopes and rivers requires a computational model that explicitly includes the path of sediment from uplifting bedrock through weathering, soil creep, rapid landsliding, and into a landslide deposit, as well as the impact of this sediment on fluvial erosion or deposition (Campforts et al., 2022).

Landslides are discrete events of non-local sediment transport, which do not necessarily fit well into the simplified continuous functions that are used in LEMs. Some LEMs explicitly include landslides, modeled as either stochastic events or as continuous processes (Booth et al., 2013; Campforts et al., 2020; Claessens et al., 2007; Densmore et al., 1998; Egholm et al., 2013; Istanbulluoglu and Bras, 2005; Keck, 2023; Meisina and Scarabelli, 2007; Moon, 2015; Tucker and Bras, 1998). The models implemented at landscape evolution timescales are mostly continuum style functions (Istanbulluoglu and Bras, 2005; Tucker and Bras, 1998), while discrete event models are mostly implemented at decadal to centennial timescales (Claessens et al., 2007; Keck et al., 2024). The BedrockLandslider model (Campforts et al., 2022) is both discrete event based and implemented at landscape evolution timescales. This model was built on earlier landsliding models (Densmore et al., 1998), and stochastically simulates Culmann theory bedrock landslides. It was developed within the Landlab open source software environment (Barnhart et al., 2020). Campforts et al. (2022) found that bedrock landsliding worked to create quasi-planar hillslopes, sediment filled valleys, and persistent dynamism of ridges and rivers in 'steady state' systems. However, Campforts et al. (2022) did not include soil depth or groundwater as part of the failure criteria and only explored the impact of 'large' bedrock slides while neglecting shallow landslides. Shallow soil landslides are the primary process for hillslope development in some landscapes (Claessens et al., 2007). However, most discrete shallow landslide models focus on short timescales, and are too complex or computationally intensive to be implemented much past decadal timescales (Keck et al., 2024).

Existing models lack a stochastic soil landslide module which can be implemented at landscape spatial scales and at the millennial timescales necessary for geomorphic landform evolution to reach topographic steady state. To fill this gap, we developed a Landlab module (SoilLandslider) that can run at these large spatial and temporal scales. We define 'soil landslides' as shallow landslides constrained to the uppermost unconsolidated layer of soil, colluvium, or regolith. In this paper we describe the module in detail and provide a set of parameters for the module to function within a landscape evolution model. Because the SoilLandslider module relies heavily on inputs and outputs from other process modules, we also go through the sets of parameters that must be used in 3 existing LEM components, why we chose them, and their impacts on model form. We validate the model against specific landslides and a landslide inventory from within the Oregon Coast Range (Montgomery et al., 2000) by comparing: the locations of instability predicted with where landslides occurred, the size of landslides modeled with the mapped inventory, and the pattern of erosion and deposition predicted by the model for an individual landslide. Lastly, we further inform the model use with two case studies. We compare landscape forms produced by a model with only linear diffusion, a model with non-linear diffusion, and a model with linear diffusion and soil landsliding. We also test the impact that ground water saturation, defined in two different ways, has on landscape form. We finish by discussing when a soil-landsliding model represents processes integral to the landscape process being studied, and when this process can be satisfactorily subsumed into other hillslope functions for future landscape evolution modelers.

2.2 Review of components of a landslide model for landscape evolution

To function in a landscape evolution model, a landslide component must solve the following 4 questions: (1) Susceptibility: where is the hillslope unstable and prone to landsliding? (2) Trigger: when and where does the landslide happen? (3) Size: how big is the landslide source area, how is that determined? (4) Runout: where does the landslide material end up?

2.2.1 Susceptibility

Due to the hazard applications, this is likely the most solved part of the landslide equation. Methods for estimating susceptibility range in scales from geotechnical approaches only applicable to outcrop scale studies to region or nationwide susceptibility estimates (Burns et al., 2016; Mirus et al., 2024). Susceptibility estimate techniques can generally be grouped into two types, empirical methods that use landslide data and statistics to identify slopes prone to landsliding based on where landslides have happened before (Glade et al., 2001; Carrara et al., 1995; Kirschbaum et al., 2012), and process driven models that characterize the forces driving and resisting failure (Montgomery and Dietrich, 1994; Strauch et al., 2018).

Most process driven models rely on some type of limit equilibrium equation where the forces resisting failure (shear strength) are compared to the forces driving failure (shear stress). Numerically this is often defined by a factor of safety value which is equal to the ratio of the shear stress over the shear strength. Factor of safety values of 1 are at equilibrium, while values above 1 are considered stable and values below 1 are considered unstable.

A common formulation to solve for the failure of a soil layer, simplifies the failure surface to an infinite plane (neglecting edge forces and giving the model its name). The infinite slope equation is derived from Mohr-Coulomb failure law and is defined by the ratio of the stabilizing forces of cohesion and friction reduced by pore water pressure, to the destabilizing forces of gravity (Hammond et al., 1992; Wu and Sidle, 1995; Strauch et al., 2024). A key component of the infinite slope equation is the estimation of ground water table, or the fraction of the soil column that is saturated. Some models simplify and assume that this value is constant across the landscape, while other methods employ hydrologic models of varying complexity. Perhaps the most common formulation for shallow landslide estimates (SHALSTAB approach) combines the infinite slope stability equation with a steady state topographically controlled flow hydrologic model following of Montgomery and Dietrich (1994) (Claessens et al., 2007; Strauch et al., 2018).

2.2.2 Triggering

In early landscape evolution models landsliding was implicitly built into the steady diffusion processes through critical slope controlled non-linear diffusion. Some models incorporated functional forms for landsliding that failed and moved material during every timestep (Tucker and Bras, 1998). However, landslides are infrequent events with a stochastic temporal nature (Campforts et al., 2022). Landslides are often triggered by earthquakes or extreme rainfall events, which occur randomly but with some degree of periodicity if considered from a landscape evolution timescale.

Variability in landslide occurrence can be accomplished by triggering a landslide at a location if the cell is unstable and a stochastic criterion is met. This can be through stochastically varying spatial and temporal parameters resisting or promoting sliding (Strauch et al., 2018; Tucker and Bras, 1998), by sampling a random number as part of the failure criteria (Densmore et al., 1998), or with a return time based temporal probability incorporation (Campforts et al., 2020).

2.2.3 Size

Landslide size is not easily predictable (Morgan et al., 2026), adjacent hillslopes can produce landslides of largely different sizes (Bellugi et al., 2021). Often susceptibility models are limited to showing which cells are at a failure state, but stop short of organizing the cells into discrete landslides. If landslide forms are desired then this step is required. Generating discrete landslides on a grid of hillslope cells can be accomplished multiple ways.

Keck et al., (2024) used a rule based clumping algorithm (LandslideMapper) to delineate landslide size, where cells prone to failure were clumped into one landslide if: they were touching, they did not extend over a ridgeline (area of convex topography), and would extend to the stream if they were within a given distance. Lehmann and Or (2012) considered a 3d network of soil columns and the forces between columns in a model (STEP-TRAMM) to simulate the onset and cascading failure of a shallow landslide, estimating landslide size extents. Milledge et al. (2014) used a 3d model (MD-STAB) which incorporated lateral forces adjoining the landslide area and estimated wedge geometries on the landslide edges to examine controls on landslide shape. Bellugi et al. (2021) built on MD-STAB with the addition of a spectral search algorithm to search for the least stable combination of possible cells for failure. Mathews et al. (2024) used a 3d force equilibrium model (RegionGrow3d) to iterate through landslide sizes and grow instabilities to balance forces (Mathews et al., 2024). Campforts et al. (2020) implemented a geometric failure propagation approach in BedrockLandslider wherein the landslide eroded all the material within a conical envelope uphill of a critical cell. The envelope is defined by the bisector of the angle of internal friction and the steepest uphill slope from the critical cell, and failure extends only uphill until this envelope daylights often at a ridgetop.

2.2.4 Runout

Once an area prone to landsliding is identified, landsliding occurs by transporting the eroded material non-locally downhill. Model forms to predict runout fall under a few classes: empirical statistical models resting on geometric rules (Reid et al., 2016), detailed mechanistic based models usually simulating landslides as some type of flow (Frank et al., 2015; Han et al., 2015; Iverson and Denlinger, 2001; Medina et al., 2008), reduced complexity models, or hybrid modelling approaches that combine physical mechanisms, with reduced complexity rules, and empirical calibrations (D'Ambrosio et al., 2003; Iovine et al., 2005; Lancaster et al., 2003; McDougall and Hungr, 2004; Keck et al., 2024). For a landscape evolution model, a single deterministic landslide displacement must be chosen. Most LEM compatible models use a reduced complexity runout model resting on a multiple flow path downhill flow map (Campforts et al., 2020; Densmore et al., 1998; Tucker and Bras, 1998, Claessens et al., 2007). These models transport material downslope until the slope is shallow enough for deposition to occur.

BedrockLandslider (Campforts et al., 2022) implements a non-linear, non-local deposition scheme (Carretier et al., 2016) where sediment is redistributed to downhill cells proportional to their slope as identified by a multiple path flow routing algorithm (Barnes et al., 2014). How much of the incoming material that is deposited on a cell depends on the ratio of the local slope to a defined deposition threshold slope, where more material will be deposited if the local slope is small relative to the deposition threshold slope, and no material will be deposited if the local slope is equal to or greater than the deposition threshold slope.

2.3 SoilLandslider model description

We built the SoilLandslider function following the architecture of the BedrockLandslider function currently available in Landlab (Campforts et al., 2022), altering the susceptibility and erosion to follow unique processes suited to soil landslides. For parts of the model which are similar to BedrockLandslider, we refer to papers describing the model in more detail (Campforts et al., 2020, 2022).

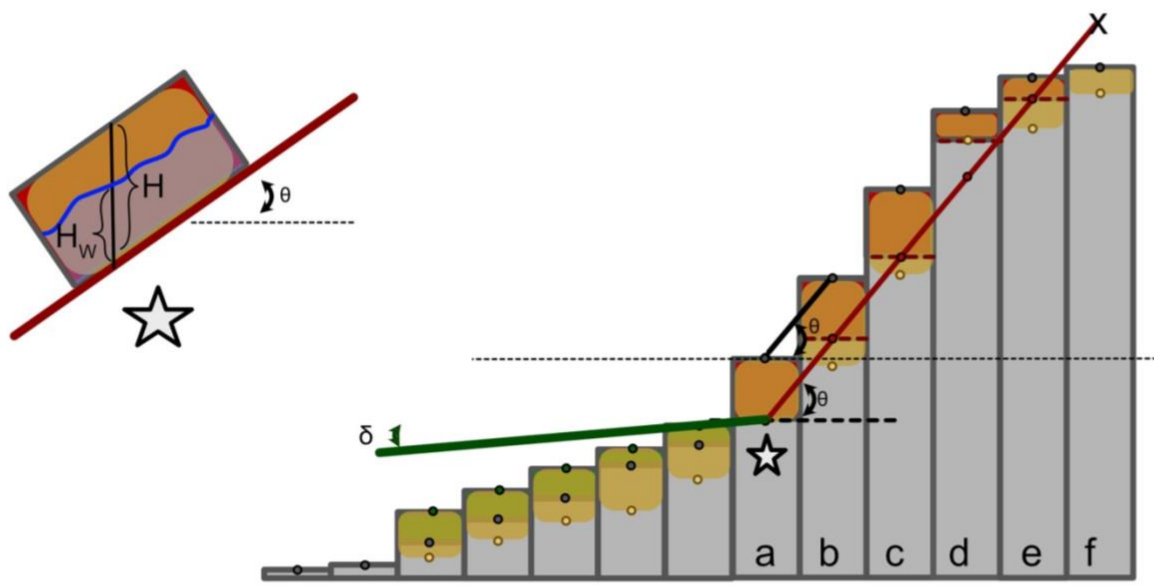

Figure 2.1: A schematic diagram of SoilLandslider. Inset illustrates the parameters used for the infinite slope equation to assess susceptibility, H is the vertical height of the soil column at the cell, H_W is the vertical height of the water column and R_W, the relative wetness fraction, is the ratio of the two H_W/H. A 2d slice of a model grid is presented, showing bedrock in grey and soil in orange-yellow. The critical node is shown at the cell with a star (cell a), and the failure plane (red line) extends up from the base of the soil parallel to the surface slope at the critical node (black line). Soil above the failure plane is eroded, see text for descriptions of the differences in the lettered cells. The failure stops propagating upslope where the cells elevation is lower than the critical plane (denoted by an X). Green highlighted region shows where sediment deposition occurs downslope of the critical node based on the deposition threshold slope S_{DT}.

2.3.1 SoilLandslider susceptibility

Soil landslide susceptibility is assessed using a factor of safety limit equilibrium equation based on the infinite slope stability model (Eq. 2.1). The derivation is similar to that of Montgomery and Dietrich, (1994); Hammond et al. (1998) and Strauch et al., (2018), except that we use the formulation for vertical measurements of soil depth (H) and relative wetness (R_W) rather than slope parallel in order to match built in Landlab outputs. This results in the factor of safety equation:

$$FS = \frac{Shear\ Strength}{Shear\ stress} = \frac{C + g\ \ H\ cos^2(\theta)(\rho_{soil} - R_W * \rho_{water})\ tan(\phi)}{\rho_{soil}\ g\ \ H\ \ cos(\theta)sin(\theta)} \qquad \text{(Eq. 2.1)}$$

where C is the effective cohesion (Pa or N/m^2), g is the gravitational constant (9.81 m/s^2), H is the vertical soil depth (m), θ is the slope (Radians), R_W is the fraction of the vertical soil depth saturated by groundwater (1 is fully saturated), ϕ is the angle of internal friction (m/m), and ρ_{soil} and ρ_{water} are the densities of soil and water respectively. The R_W fraction can be provided to the model two ways: either a set as a constant value across the entire grid of cells, or read in from each cell individually and calculated for each cell externally by the user.

2.3.2 SoilLandslider triggering

SoilLandslider triggers landslides through a critical cell based stochastic approach following the methodology of Campforts et al. (2022). For every time step, each cell has a probability of failure calculated by the product of a temporal and spatial probability, (both 0-1 values). If this probability of failure is greater than a pseudo-random number between 0 and 1 then the cell will be selected as a critical node for the initiation of a landslide.

The spatial probability is set by 1/FS from the factor of safety susceptibility analysis (Eq. 2.1), and maximizes at 1 for any cell with an unstable FS. The temporal probability is determined by a user-defined landslide return time (LRT) following Campforts et al., (2022). This LRT sets the temporal probability following a Poisson model for the probability of landslide occurrence during a set time period defined by the time step length (Crovelli, 2000). A larger LRT will result in a lower temporal probability for all cells and result in fewer landslides per model timestep.

Alternatively, critical nodes can be predetermined and provided to the model by their model grid node number. However, the model will only fail a predetermined critical node if the cell is determined to be unstable.

2.3.3 SoilLandslider erosional area

Once a landslide is triggered at a critical node, that cell defines the failure plane of the landslide. A failure plane is projected uphill from the base of the soil layer on the critical node with an inclination defined by the steepest surface slope at the critical node. The landslide area grows by iterating through uphill neighbors of cells that have added to the erosional volume. When iterated to as an uphill neighbor, there are a few possibilities for each cell. (1) if the failure plane intersects the cell below the surface but above the bedrock elevation (cells b, c and e in Fig. 2.1), only the soil above the failure plane is removed from the cell and added to the erosional volume and the failure continues to propagate uphill. (2) if the failure plane intersects the cell below the top of the bedrock layer (cell d in Fig. 2.1) then all of the soil layer of that cell is removed and added to the erosional volume and the failure continues to propagate uphill, but the bedrock above the failure plane is not removed and remains intact. And (3) if the failure envelope intersects a cell's location above the surface of the soil (cell f in Fig. 2.1) then no material is eroded and the failure will stop propagating uphill. This default case results in landslides that fail until the failure plane daylights at a ridge top.

While this is a generally reasonable assumption for bedrock landslides, soil landslides may be less likely to always fail to the hilltop (See validation section for more information). We add in two ways to limit the propagation of failure before the failure surface reaches the ridgetop. (A) the user can define a 'stable stopper' factor of safety value: if a cell has a factor of safety above the defined stable stopper value then no material will be eroded from that cell and the propagation will not continue through that cell to nodes uphill. (B) the user can define a maximum step height that the landslide cannot pass through: if the bedrock elevation at the cell is greater than a maximum step height above the elevation of the failure plane at that location then no material will be eroded at that cell and the failure will stop propagating uphill through that cell. The max step height feature also limits propagation through strongly concave up landscapes.

2.3.4 SoilLandslider runout

For each landslide, the total eroded volume is summed from above the critical node, and then is deposited starting downhill of the critical node. Landslide runout and sediment deposition is deposited according to the same algorithm as implemented in Campforts et al. (2022). Landslide material cannot be deposited within the source area, but rather only downhill of the critical node. Material is deposited on cells downhill from the critical node according to their distance from the critical node and the slope of the cells. Deposition at a downslope cell does not occur if the cell's slope is above a critical deposition slope (which is set by the user), and is instead deposited further downhill where this condition is met. Material is deposited downhill proportioned by the relative slopes to downhill cells using a multiple flow path flow routing algorithm (Barnes et al., 2014).

2.4 Landscape evolution model components and parameter choices

Running a landscape evolution model with a soil landsliding module requires model components in which material travels through the earth system from bedrock, through soil production into soil, then is transported downslope through creep or landsliding, incorporated into fluvial processes when connected to rivers. In this section we lay out the Landlab modules and chosen parameter values we use to simulate a landscape with realistic river networks, hilltop widths and drainage densities, and a stable soil layer. Although this section is intended to serve as a general guide to our module and workflow, our chosen model parameters in the outlined workflow are inspired by the Oregon Coast Range, USA. A more in depth discussion of these parameters can be found in the accompanied supplemental user manual.

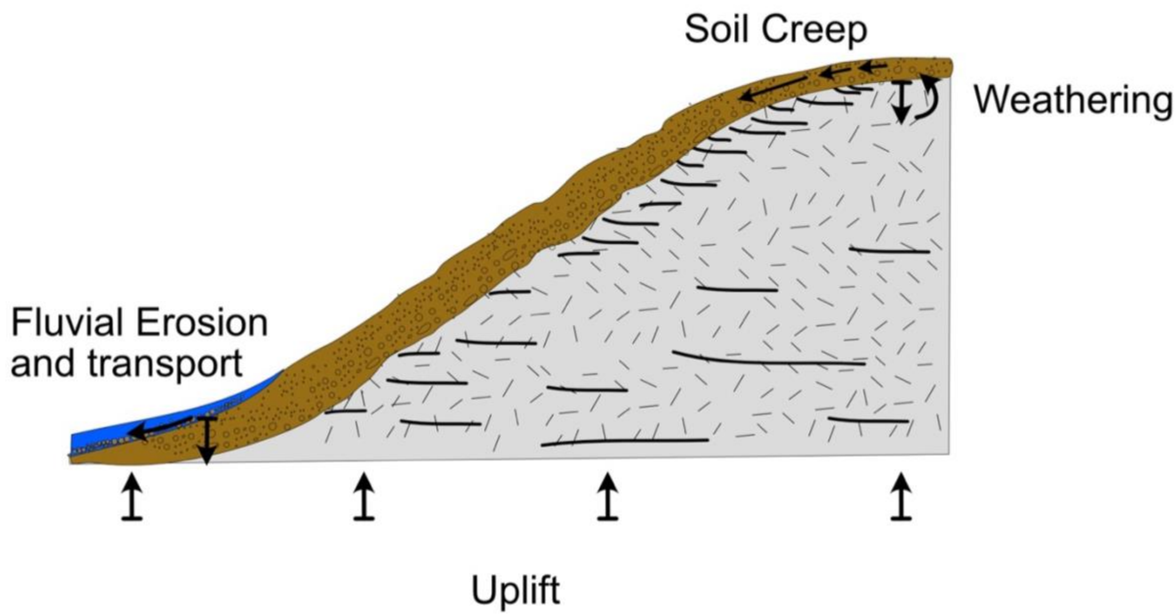

Figure 2.2: Schematic of a hillslope, illustrating the four processes we simulate in our landscape evolution models, including Uplift that acts evenly across cells raising bedrock elevations, weathering or soil production that converts bedrock to soil lowering bedrock elevation and generating a soil layer, soil creep or diffusion which moves soil downhill, and fluvial processes that transport sediment, and incise into bedrock and sediment.

2.4.1 Soil Landsliding

The new landsliding component requires several inputs to run. To determine the temporal frequency the landslide return time must be set. This sets the frequency of landslide triggering (though there must also exist unstable cells). We find values of 20,000 years works to generate a reasonable amount of landslides, this is the same value chosen in (Campforts et al., 2020). Varying the landslide return time does change the general number and size of landslides, but does not alter the landscape form significantly. Because the spatial landslide frequency depends on the selected LRT and the grid resolution, grid size, and model setup it is difficult to approximate this parameter directly from recorded landslide frequency estimates (e.g., Luna et al., 2025) so users may wish to calibrate this return time after model runs.

Two parameters must be set relating the hillslope strength in the Factor of Safety calculation, the effective cohesion C (in Pa or $m^{-1}s^{-2}$), and the angle of internal friction (ϕ)(fraction m/m). Effective cohesion values (primarily due to lateral root strength) measured in the Oregon Coast Range vary greatly from 6.8-94 kPa depending on the logging history and forest type (Schmidt et al., 2001), though cohesion values of 0-1.8 kPa where found to match the saturated soil properties at the time of failure of a soil landslide within the coast (Montgomery et al., 2009).

We choose values of 4 kPa (input at 4000 Pa in the model) for C, which falls near both of these ranges. (Montgomery et al., 2009) also found that friction angle values of ~40 degrees or ~0.8 (m/m) match recorded landslides, which is what we use in the model.

One parameter controls the runout and deposition, the threshold slope (not to be confused with the critical slope for non-linear diffusion), which sets the slopes that landslide material can begin to deposit. Campforts et al., (2022) used a value of 0.8 for their model runs that simulated deep seated bedrock landslides with the same runout algorithm. Keck et al., (2024) measured the surface slopes of several fresh landslide deposits in the field (including several in coastal ranges of Washington State) to calibrate a similarly functioning slope for material deposition and found depositional slopes ranging from 0.1 to 0.4 (m/m). To match the non-deposition locations of the Greenleaf landslide we chose a value of 0.3 (m/m).

The relative wetness fraction (R_W) can be provided to the model in two ways, either as a constant set value for all cells, or a value read in on a cell by cell basis from the grid, as calculated or specified by the user. In this study we implement our own simple topographically controlled relative wetness calculation (following the example of Strauch et al., 2018) where the relative wetness at each cell is calculated by:

$$R_W = \frac{H_w}{H_S} = \frac{R\ A}{K_{Sat} H_S sin(\theta)} \tag{2.2}$$

Where H_w is the height of the water table, and H_S is the height of the soil column (both perpendicular to the slope), R is the recharge rate (mm/d), A is the drainage area at a cell, K_{sat} is the saturated hydraulic conductivity (m/d), and θ is the slope. See section 2.6.2 for models implementing this simple topographically controlled ground water flow model.

2.4.2 Other modules and model setup

In our models we implement uniform uplift across the whole grid by adding elevation to the bedrock layer each timestep before updating the topographic elevation and running the erosive modules. Uplift experienced by real landscapes varies greatly from landscapes not (or no longer) uplifting to the fastest actively uplifting mountains ~6-9 mm/yr in New Zealand (Little et al., 2005) or 4-8 mm/yr in Taiwan (Hsu et al., 2016). Proposed uplift values for the Oregon Coast Range vary from 0.05 mm/yr ($5x10^{-5}$ m/yr) to 0.3 mm/yr ($3x10^{-4}$ m/yr) (Struble et al., 2021); for our models we use an uplift value of $3x10^{-4}$ m/yr or 0.3 mm/yr which is on the high end of proposed uplift rates.

For grid resolution we use a 10 m x 10 m cell size, fine enough resolution so that hilltop character and curvature are realistic, but coarse enough so that derivations for the fluvial erosion component are still valid. Grid resolution plays a role in landslide frequency because the temporal probability-based trigger is applied to every cell, so if there are more cells within an unstable hillslope then it is more likely for a landslide to be triggered on it. Grid resolution also has been shown to impact landslide sizes in LEMs, where coarser resolution smooths the landscape and results in more area being classified as stable and smaller amounts of soil redistribution (Claessens et al., 2005). For the model grid domain size we choose a 100 by 100 cell square grid, we choose an open on all sides grid so that the central ridges are not defined by edge effects and are limited to 100 by 100 cells for computational limits.

For Flow routing on our model we use the landlab ***PriorityFloodFlowRouter*** component (Barnes et al., 2014). This module is preferred because it efficiently fills and flows over landslide created depressions.

Our landsliding model only displaces the topmost layer of mobile regolith or soil, while a bimodal classification difference between soil and bedrock neglects the spectrum between the end members, it also reflects observations that soil landslides often fail weathered soil and leave intact relatively cohesive bedrock (Larsen et al., 2010; Montgomery et al., 2009). Having these layers in a model necessitates a function that simulates physical and chemical weathering processes that convert cohesive bedrock into soil. We implement the Landlab component ***ExponentialWeathererIntegrated*** (Barnhart et al., 2019). This component, uses an inverse-exponential function of soil thickness to define the weathering rate at any time step (Ahnert, 1976, Heimsath et al., 1997; Small et al., 1999):

$$W = P_0 e^{(-H/H_{WD})} \tag{2.3}$$

where w is the amount of weathered soil from bedrock, P_0 is the maximum weathering rate, H is the soil depth at the node, and H_{WD} is the soil production (*weathering*) decay depth. The soil production maximum rate (P_0) has a large impact on the stable soil depth on hillslope cells. Heimsath et al. (2001) used cosmogenic nuclides in bedrock in the Coos Bay area finding an exponential relationship between soil production rate and soil depth with rates varying from 268 m/ Ma^{-1} (2.68×10^{-4} m/yr) on slopes with thin to absent soils and as slow as ~0.02 mm yr^{-1} (0.2 $\times 10^{-4}$ m/yr) on hillslopes with deep (~1 m) soils. Measurements of the maximum soil production rates observed in the world are in New Zealand and are up to 2 mm yr^{-1} (20×10^{-4} m/yr) (Larsen et al., 2014). In our models we use a value of 4.5 $\times 10^{-4}$ m/yr which is slightly higher than most of the measurements for the Oregon Coast Range, but still within reasonable bounds, in order to keep a stable soil layer on the landscape. For H_{WD} we use 1.5 m which is similar to observed depths of creep related processes that are likely shallower than the weathering front for observation in California (Johnstone and Hilley, 2015).

To represent the continuous gradual transport of sediment downhill on hillslopes we use the Landlab module ***DepthDependentTaylorDiffuser*** which represents soil creep as diffusive transport that is modified by a depth-dependent term and a non-linear transport near critical slopes term following the equation:

$$Q_s = (K_s H_{DD} S)\left(1 - e^{-H/H_{DD}}\right)\left[1 + \sum_{i=1}^{Nterms} \left(\frac{S}{S_C}\right)^{2i}\right] \tag{2.4}$$

Where K_S is a transport coefficient with units of velocity, H is the soil depth, H_{DD} is the soil transport (*diffusion*) decay depth, S is slope (m/m), S_C is the critical slope, and Nterms defines how many terms of the Taylor expansion are used. The first term in Eq. 2.4 analogous to a traditional diffusion equation where the product of the soil transport velocity and soil transport decay depth is equivalent to commonly used diffusivity coefficients (D) ($K_s \times H_{DD} = D$), in formulations where $Q_s = DS$ (Barnhart et al., 2019). Measured values for D range from 1 $\times 10^{-4}$ – 80 $\times 10^{-4}$ $m^2\,yr^{-1}$ (Martin and Church, 1997), and for the Oregon Coast Range have been estimated at 30 $\times 10^{-4}$ $m^2\,yr^{-1}$ (Roering et al., 1999) and 22 $\times 10^{-4}$ $m^2\,yr^{-1}$ (Struble et al., 2024). The soil transport decay depth is perhaps the parameter in our model least well constrained by field data. Johnstone and Hilley, (2015) observed a value of 0.33 m to match the drop off in activity of agents thought responsible for soil disturbance with depth on Californian hillslopes. In our tests we found that slightly higher values of D ($K_s \times H_{sc}$) than those estimated for the OCR are needed to achieve observed ridgetop widths above critical slopes. We use values of 0.22 m for H_{DD} and 0.03 m/yr for K_S resulting in an equivalent D value of 66 $\times 10^{-4}$ $m^2\,yr^{-1}$. For our critical slope we choose 0.8 which is set to match the angle of internal friction, though slightly lower than some calibrated value in the OCR (Roering et al., 1999).

Landslides can move large volumes of sediment into river systems (Li et al., 2016) so it follows that any fluvial component must be able to simulate sediment transport. Multiple modules exist within the Landlab ecosystem that simulate river sediment transport and erosion: the Stream Power with Alluvium Conservation and Entrainment (*SPACE*) model (Shobe et al., 2017), the *RiverBedDynamics* model (Monsalve et al., 2025), *ErosionDeposition* (Barnhart et al., 2019), and the *GravelBedrockEroder* (GBE) model (Gabel et al., 2024).

Parameter	Description	Realistic Value range	Value in model X
Landlab model setup/component list			
Rows (-)	Number of grid rows	-	100
Columns (-)	Number of grid columns	-	100
dx, dy (m)	Grid cell size	-	10
U (m yr^{-1})	Uplift	0 - 5e-3	3e-4
R (m yr^{-1})	Runoff_rate		10
Weathering / Soil production using **ExponentialWeathererIntegrated**			
P_0 (m yr^{-1})	P_0 is the ***soil_production__maximum_rate***	0.2 – 20 x10^{-4} m/yr	4.5 x10^{-4} m/yr
H_{WD} (m)	H_{WD} is the (***soil_production__decay_depth***	0.4 - 2 m	1.5 m
H_E (-)	(***soil_production__expansion_factor***)	1-2	1
Soil Creep / diffusion using **DepthDependentTaylorDiffuser**			
K_S (m yr^{-1})	(***soil_transport_velocity***)		0.03
H_{DD} (m)	(***soil_transport_decay_depth***)	0.1-0.5	0.22
Nterms	Number of terms in the Taylor expansion 1 for linear diffusion, 2+ for non-linear diffusion.	1-3	2
S_C	Critical slope (***slope_crit***)	0.8-1.25	1 or 0.8
Fluvial erosion / deposition with **GravelBedrockEroder**			
k_{QS}	k_{QS} is (***transport_coefficient***)	?	0.041
I	I is the ***(intermittency_factor***)	?	0.01
H_{FD} (m)	The fluvial (***depth_decay_scale)***	1+	2.0
ζ	ζ Is the (***abrasion_coefficient***)	0.002-0.01	0.005
K_P	K_P is the (***plucking_coefficient***)	10^{-4}-10^{-7}	10^{-4}
γ	(γ) (***coarse_fraction_from_plucking***)	?	0.25
Sed_por	sed_por is the (***sediment_porosity***)	?	0.35
Soil Landsliding **SoilLandslider**			
ϕ	Angle_int_frict		0.8
C	Cohesion_eff	2200-7000	4000
R_W	Relative Wetness saturation fraction	0.8 or calculated	0.8
LRT	Landslides_return_time	Depends on grid	20000
S_{TH}	Threshold slope	0.1-0.8	0.3

Table 2.1: Model Parameter choices

2.5 Model validation

We designed SoilLandslider to run in landscape evolution models tracking erosion and deposition from landslides over tens of thousands to millions of years. As a result, we lack existing robust real-world datasets to calibrate model relevance over that timescale, but we can compare short term model results with real landslides. We compare our stability predictions to observed landslide locations, the size distributions of the triggered landslides, and the erosion and deposition pattern of a single landslide (Figure 2.2-2.4), all within the Oregon Coast Range.

2.5.1 Susceptibility

To test our susceptibility estimates we follow the example of (Bellugi et al., 2015) and compare model predictions of stability to a detailed landslide inventory collected over 10 years (1987-1998) in the Coos Bay area of the Oregon Coast Range (Fig. 2.2) (Montgomery et al., 2000). To compare our model to the dataset, we input a lidar DEM of the region as the model topography, down-sample the DEM to 3m x 3m pixels for computational feasibility, drape 1m of soil over the landscape evenly and run 500 years of diffusion and weathering to prime the landscape for failure (W_0 = 4.5 x10^{-4} m/yr, H_{WD} = 1m, K_S= 0.03 m/yr, H_{DD}= 0.22m, Nterms=2, and S_C = 1 m/m). We compute the R_W fraction using the estimated soil depths a K_{Sat} value of 7 m/day (Matching value chosen by Strauch et al., 2018) and a recharge value of 0.03 m/day scaled to match the grid size and to saturate at the mapped channel heads in Fig. 2.2 b. The factor of safety is calculated using a cohesion C value of 22 kPA and a ϕ of 0.8 (following Bellugi et al. (2015)).

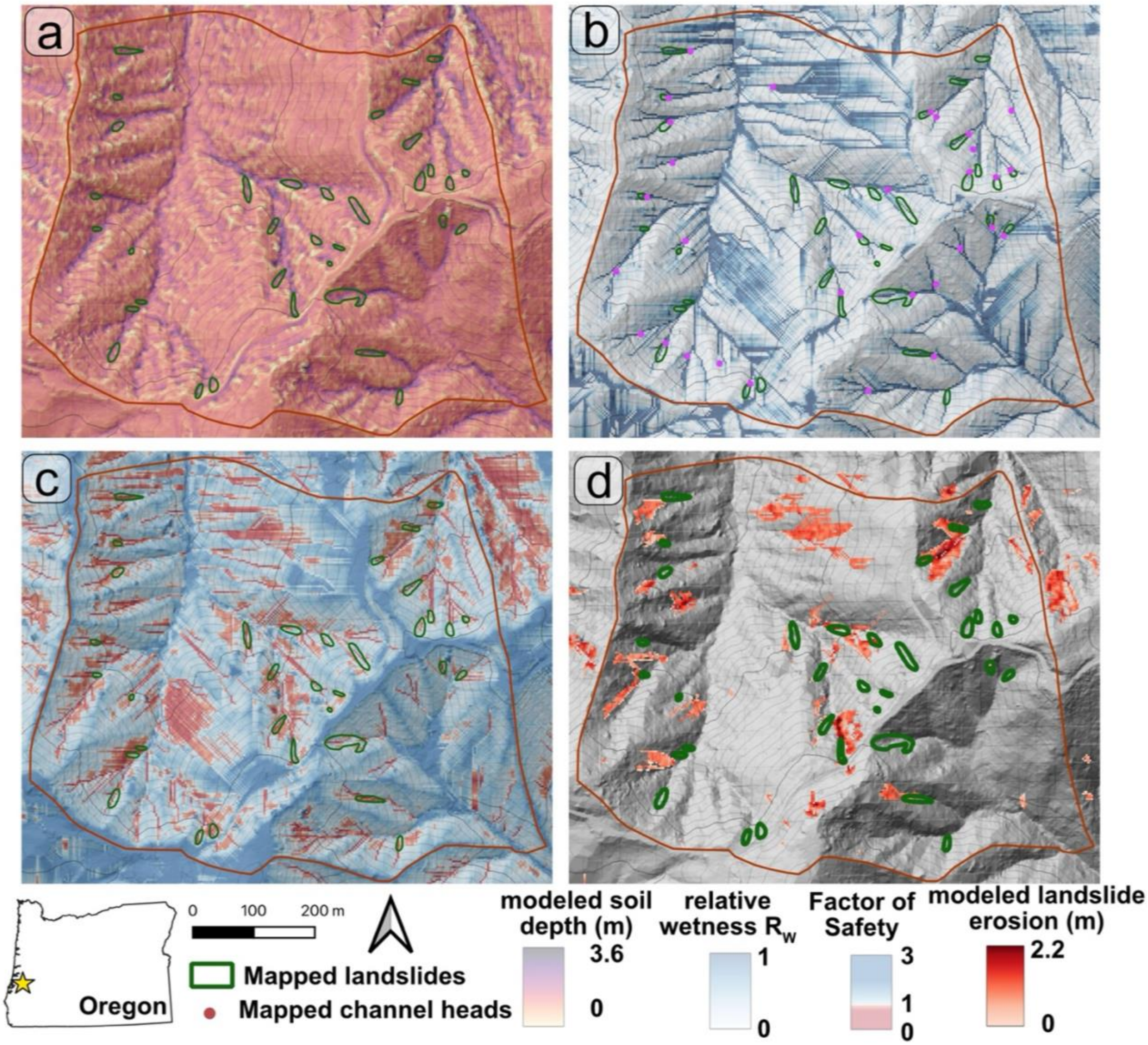

Figure 2.2: Model results and mapped landslide inventories for the Coos Bay site, Oregon Coast Range. Mapped landslide inventory of Montgomery et al. (2000) in green polygons for all 4 panels. (a) modelled soil depth predictions, (b) modelled relative wetness R_W predictions, (c) modelled factor of safety estimations, and (d) landslide distributions from a single model run.

Five hundred years of simulated weathering and diffusive creep causes soil to collect in colluvial hollows near the areas where landslides are mapped and deeper soil depths are observed (Montgomery et al., 2000) (Fig. 2.2a). The simple steady state solution for topographically directed hydrologic processes collects water in hollows around the mapped channel heads and around where the mapped landslides are located (Fig. 2.2b). The flow router used tends to concentrate flow into single pixel flow paths, observable as occasional pixel wide fingers of saturated depths (Fig 2.2b) and more notable on grids with high resolution, or planar slopes. The factor of safety calculation estimates the least stable locations in the hollows where landslides are mapped (Fig. 2.2c). All the mapped landslides overlap with unstable values by at least one cell (Fig. 2.3a), though only 15% of all cells were unstable and the mapped polygons only make up 1% of all of the slide points. This demonstrates that our model is capable of predicting failure at the landslide locations while not dramatically overpredicting that all slopes are unstable.

2.5.2 Landslide inventory comparisons

We also use the Coos Bay dataset to compare the sizes of simulated versus real world landslides. After calculating the factor of safety on the topography (Fig. 2.2c), we ran a landsliding time step with SoilLandslider (dt=10 years, LRT of 2000 years, FS stopper = 1.1) which triggered 80 landslides (Fig. 2.2d). Following Bellugi et al. (2015) we compare the topographic position index defined by Dietrich et al. (1992) of the mapped and modelled landslides and find a good match signifying that the simulated landslides occur in similar positions in slope-area space in the landscape (Fig. 2.3b).

Relative size scaling is a common method for validating landslide models (Bellugi et al., 2015; Campforts et al., 2020). Visually, many of the modelled landslides appear similar in dimensions to the mapped landslides, and also there are many model landslides with finger-like uphill extents following valleys. When comparing the log distribution of landslide areas (following (Bellugi et al., 2015; Medwedeff et al., 2020), our model predicts landslides with a smaller area distribution and similar maximum sizes (Fig. 2.3c). We also compare the frequency density of the landslide area distributions (Fig. 2.3d) (Campforts et al., 2020; Malamud et al., 2004). Frequency density plots help to illustrate the relative frequency of the larger landslides in an inventory by showing their decreasing relative abundance. Again, the modelled landslide inventory includes more small landslides, but the larger landslides of both inventories follow a similar decreasing abundance trend (Fig. 2.3c).

The SoilLandslider component is capable of producing many landslides smaller than are observed in our real-world dataset. We believe that the dataset is complete and not missing small landslides (like many landslide inventories (Tanyaş et al., 2019)), due to the small area and detail of the mapping (Montgomery et al., 2000). The modelled small landslide sizes is not surprising given that the landslide area growth algorithm does not impose a minimum size for instability, which allows for even single cell landslides. This limitation of the model is especially notable when using high resolution grids and low FS stopper values.

There are several ways in which parameter adjustments can alter the size of landsliding. Increasing the pixel size would raise the lower limit on landslide sizes and smooth out gradients, decreasing variability in factor of safety values and grouping more cells per slide (Claessens et al., 2005). Altering the strength parameters can increase the area of the slopes that are unstable allowing further uphill landslide area propagation, though this represents a trade-off between overprediction of unstable areas and predicting larger landslides. Similarly altering or removing the FS stopper can also allow landslides to extend further on the hillslopes and represents a trade-off between landslide size and failure of stable terrain. While modelled small landslides are less notable on lower resolution models, the user must decide what is more important for their model to capture: the precise location of landsliding or realistic size distributions. Finally, this inventory covers an exceptionally small area and contains only relatively small landslides, that are restricted to the hollows, so more validation should be done to compare the model predictions with larger inventories that capture more and larger soil landslides.

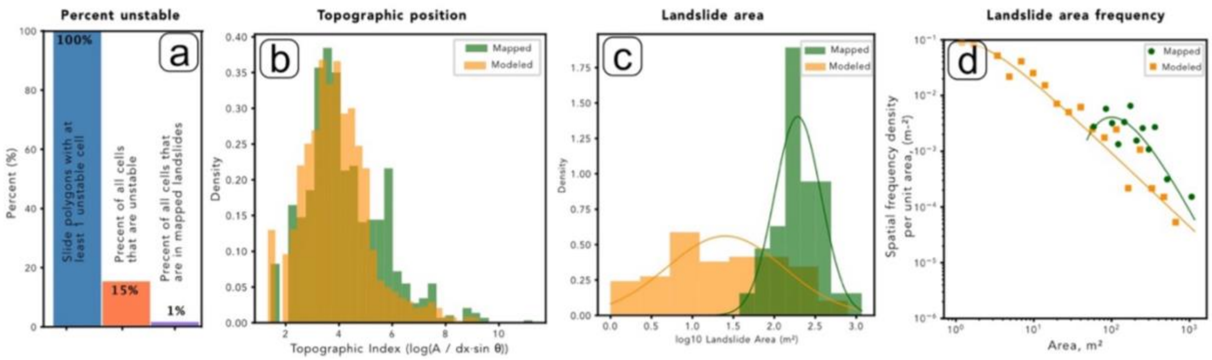

Figure 2.3: Comparison of modelled and mapped landslide distributions for the Coos Bay site, Oregon Coast Range. A) relative percentage of mapped landslides containing unstable cells, the percent of all cells that are unstable, and the percent of all cells that are contained in the mapped landslides. b) relative topographic position of mapped (green) and modelled (yellow) landslides calculated following the equation of Dietrich et al., (1992). c) log10 areas of the mapped (green) and modelled (yellow) landslides fit by a lognormal distribution and d) spatial frequency density of areas of the mapped (green) and modelled (yellow) landslides and fits by a three parameter inverse gamma function (Malamud et al., 2004).

2.5.3 Individual landslides erosion and runout patterns

We use the recent shallow landslide on Greenleaf Creek within the Oregon Coast Range to compare mapped and modelled individual landslide erosion and runout patterns (Fig. 2.4). We set up our model grid pre-landsliding conditions using the following configuration: (1) we use a 10 m DEM grid resolution to match the grid resolution used in long term landscape evolution models, (2) we add 1 m of soil to the landscape, and (3) we then simulate 500 years of diffusive soil creep, weathering, and fluvial erosion following the parameters used in the model presented in section 2.5.1. We switch from a 3m grid resolution used to capture the finely detailed inventory in Coos Bay, to a 10m grid resolution to test the pattern of erosion and deposition with a resolution that is more likely to match long term landscape evolution models. The resulting model grid has the soil depth distribution plotted in Fig. 2.4b. We calculate the R_W values using these soil depth values, a K_{Sat} value of 7 m/day and a recharge value of 0.005 m/day (scaled down from Sect. 2.5.1 because of the increased cell dimensions). And we use the same landslide strength parameters C = 22 kPA and ϕ = 0.8 for the factor of safety estimations. For this test, we predefine the point of landslide initiation to match the bottom edge of the erosive zone of the observed landslide. We test the landslide failure area growth with three different FS stopper values, the results of which are shown in Fig. 2.4d-f.

In general, the model produces a realistic looking landslide, with an arcuate erosional scar, slim valley bottom runout path, and slightly lobate toe at the valley bottom (Fig. 2.4). However, there are several notable differences between the extent of erosion and deposition in the modelled and real landslide. First, the real landslide did not erode all the way to the ridge; rather, the headscarp of the soil slide is ~100 m (horizontally) downslope from the ridgeline. In SoilLandslider, the failure propagates uphill until one of three things happen: (1) the failure plane daylights above the elevation of a cell, often at a ridge top (Figure 2.4d), (2) a maximum step height (i.e., bedrock elevation height above the failure threshold) is reached. This can occur if there is a significant step in the landscape above the hillslope, or if the landscape curvature is significantly concave up but is not demonstrated in this model. And (3) if the factor of safety stable stopper value is pre-defined, which will prevent a landslide from propagating through a point if that point's pre-slide factor of safety is above (i.e., more stable) than a set value (Fig. 2.4e,f). By varying the FS stopper value, we can limit the extent of upslope landslide propagation, producing a modelled erosional area more similar to the observed slide. Clumping algorithms that calculate strength based on the slide area and optimize slide extent to minimize hillslope strength (Mathews et al., 2024; Milledge et al., 2014) may show an improvement over the failure area propagation method we implement, but are generally not feasible to operate over geomorphic timescales.

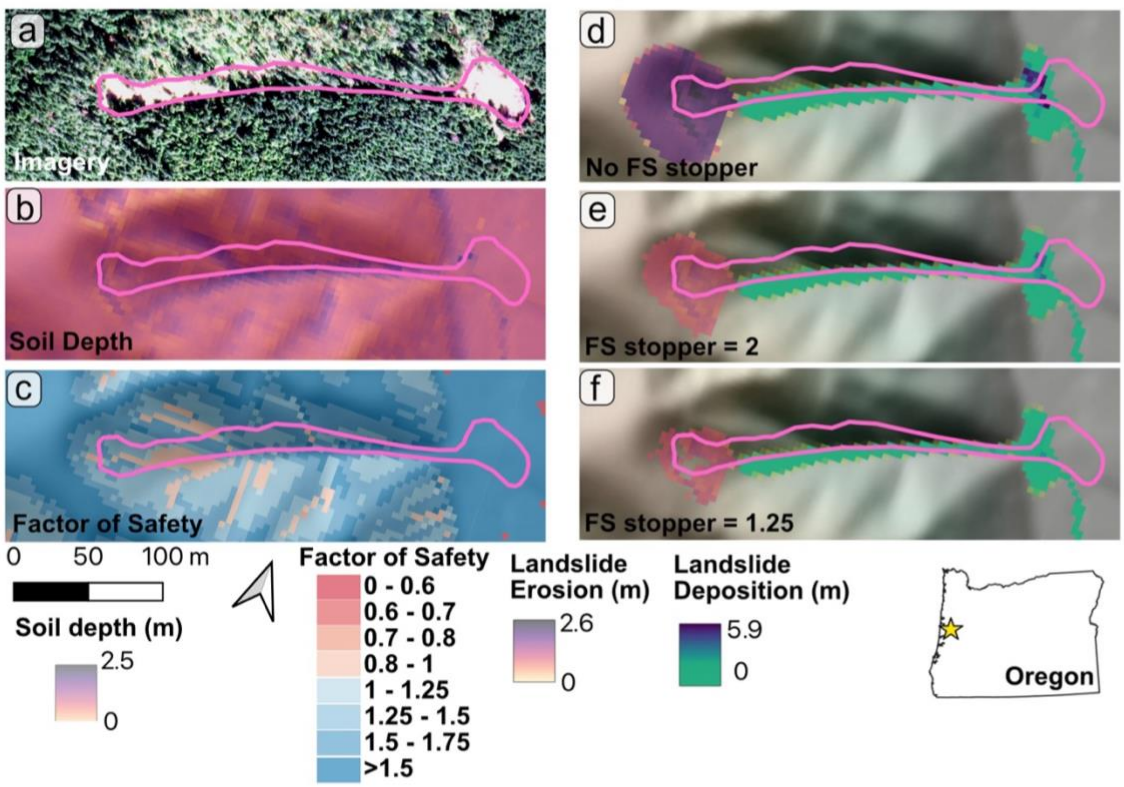

Figure 2.4: A comparison landslide erosional and depositional extent for modelled landslides and the Greenleaf Creek landslide. (a) imagery of the Greenleaf Creek landslide used to map the landslide extent. (b) the simulated soil depth on a DEM of the area. (c) estimated factor of safety. (d-f) show the modelled landslide erosional and depositional extent for models with different FS stopper values.

The runout patterns also differ slightly. The modelled runout extends into the valley and piles sediment up at the base of the hollow, including some deposition slightly upstream, before continuing to deposit sediment downstream along the river path.

The observed runout forms a debris lobe that extends further into the valley bottom flat, and does not travel down the stream. Our model does not incorporate the momentum that the falling debris clearly had, which allowed it to crash through trees and run up slightly uphill on the other side of the valley bottom stream which hugs the western side of the valley. In the model we can tune the deposition angle of the sediment which alters where deposition begins and the slope at which it is left behind. Some models (Claessens et al., 2007; Keck et al., 2024) incorporate parameters that simulate slide momentum, though at a computational cost. Allowing modelled runout to move uphill would require an approach beyond flow-routing-based method used here, and thus is beyond the scope of this model. While this limitation is important for hazard prediction, at the timescales over which this model is designed, these differences are likely to smooth out through the downstream reworking of the deposited material over decades. In general, the peak erosional and depositional locations predicted by the model match the observations.

2.6 Discussion

2.6.1 SoilLandslider compared with non-linear diffusion

To further inform the use of the SoilLandslider module, we present a numerical experiment in which we compare landscape evolution models that incorporate SoilLandslider to models with only non-linear diffusion, which has previously been suggested to approximate shallow landsliding (Roering et al., 1999). This case study is intended to inform future use of the SoilLandslider module, and demonstrates its application within a landscape evolution model run to steady state.

Significant effort has been devoted to the theoretical description of, and implications of, models that combine linear hillslope diffusion and stream power fluvial advection (Litwin et al., 2025; Perron et al., 2008; Theodoratos et al., 2018). The addition of a non-linear diffusion term to hillslope erosion has also been explored in detail, both in primarily 1d theoretical models (Roering et al., 2007) and in applications explaining observed topography (DiBiase et al., 2023; Godard et al., 2016; Roering et al., 1999), to the point where it is considered standard to implement non-linear diffusion to simulate hillslope erosion in landscape evolution models (Barnhart et al., 2019).

We compare three models with different modes of hillslope erosion: one model with only linear diffusion (LD, Nterms=1), one model with non-linear diffusion (NLD, Nterms=2), and one model with linear diffusion and soil landslides (LDSL). We hypothesize that non-linear diffusion is analogous to soil landsliding in that both models accelerate sediment transport at steep slopes. We expect to observe steeper slopes in the linear diffusion model and more planar slopes in both the non-linear diffusion model and landsliding model. Figure 2. (a-c) shows the “steady state” topography of modelled landscapes after 2 million model years, as well as slope-area plots (Figure 2.5 d-f) for the three experiments.

Overall, we observe similarity in the relief, the general spread of slopes, and drainage structure across all three models. In two-dimensional models with no fluvial erosion (Roering et al., 2007), these components would produce strongly contrasting forms, between a planar hillside and a parabolic form. In three dimensions, with the given drainage density, soil production rates, and soil-depth dependencies, the linear diffusion model produces remarkably planar hillslopes, though it also exhibits the highest slopes at low drainage areas (Fig. 2.5d). Both the non-linear model and the landsliding model reduce slopes at lower drainage areas, though the landsliding model has lower slopes than both other models at drainage areas corresponding to the channel heads (~10^3 m^3). Although subtle, the landsliding model appears to produce a slightly lower drainage density as well.

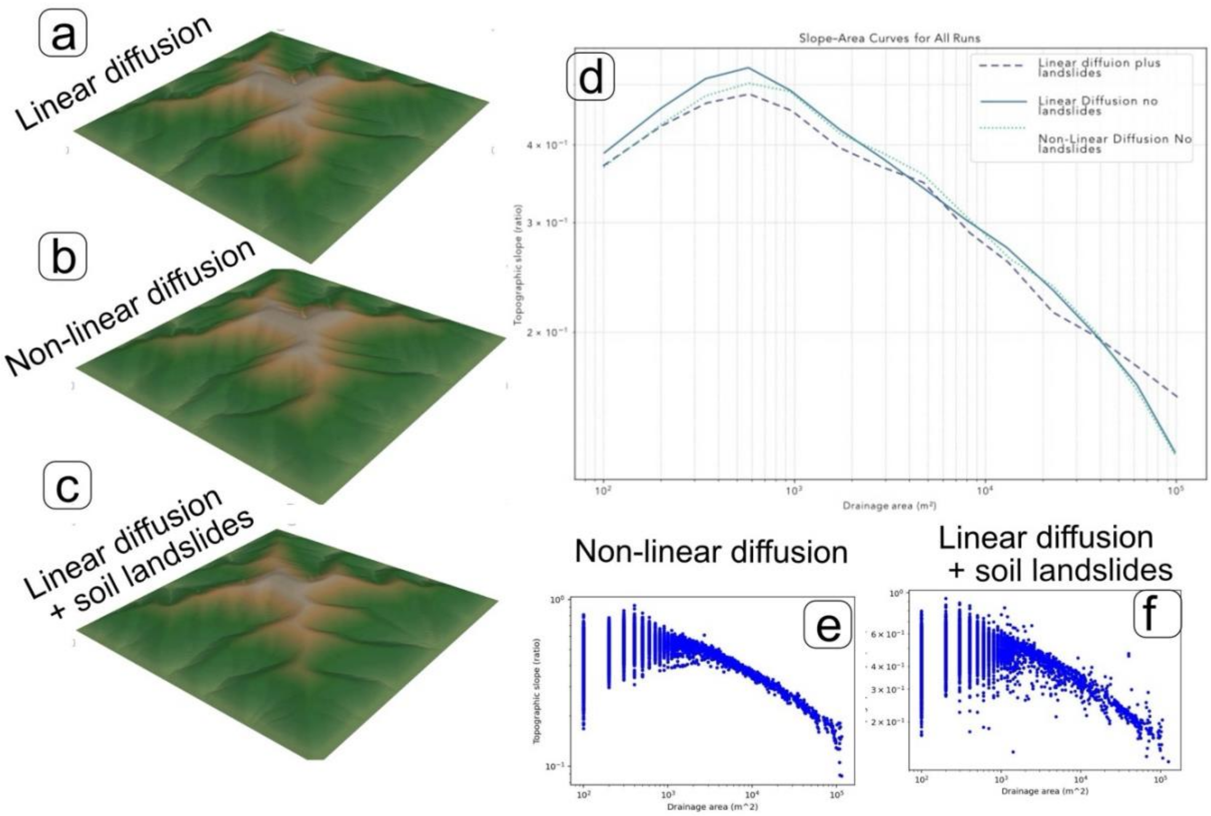

Figure 2.5: Comparison of landscape evolution models, using three different methods for hillslope sediment transport. (a-c) show landscapes generated by model runs with separate hillslope sediment transports functions, (a) linear diffusion only, (b) non-linear diffusion, and (c) linear diffusion with soil landslides. (d) shows the drainage area binned average slope-area plots for all three resultant model topographies. (e) and (f) show the raw slope-area data for all pixels in the non-linear diffusion model and the linear diffusion and soil landsliding model, showing increased spread in the data for the landsliding model.

We conclude that the difference between linear and non-linear diffusive models is less than expected. In the linear diffusion only model, the interplay between the river network, convergent topography, and the depth-dependent terms of all of the components act to decrease downhill slopes preventing the profiles from appearing entirely parabolic. Shallower slopes at relatively low drainage areas are the primary difference in hillslope form between the linear and non-linear diffusion models. Decreased slopes at low drainage areas are also produced by the shallow landsliding only model. While more mechanisms than shallow landsliding likely account for non-local transport at steep slopes (Furbish et al., 2021), it is feasible that soil landsliding alone could act as the dominant non-linear transport mechanism, forcing higher transport rates at steeper slopes.

2.6.2 *Impacts of the groundwater model*

We also ran a numerical experiment to assess the role of groundwater hydrologic parameter choices in controlling landscape form, again to inform use case decisions for users and to demonstrate the model capabilities. At the years to decades timescales, hydrologic conditions are the input to slope stability with the greatest variation and thus their relationship to landslide susceptibility has been extensively studied (Strauch et al., 2018 and the references therein). However, dry or constant R_W susceptibility estimates are still common, especially for regional or earthquake triggered susceptibility studies (Grant et al., 2016; Sharifi-Mood et al., 2017).

We ran 10 model scenarios with various characterizations of the hydrologic inputs to landslide susceptibility. In one set of models, the R_W fraction is calculated using topographically controlled steady-state ground water flow and in the other set the R_W fraction is set to a constant value across the map area. We use the hydrologic model defined by equation 2.2, and vary recharge while keeping the other parameters fixed; the resulting R_W values from different recharge parameters are shown in Fig. 2.6 b-c. In the constant R_W case, we vary R_W from 0.25 to 1 uniformly across all cells.

When we view the resultant landscapes as slope-area plots (showing the mean slope per area bin), we see that all the different models produce minimal changes to the fluvial portion of the landscape, i.e., locations with drainage areas > 10^4 m^2. The least saturated models from both sets have a similar pattern, maintaining the steepest slopes across the models, and are most similar in form to the linear diffusion only model in Fig. 2.5d. The most saturated models in both sets also follow a similar pattern, with a notable relative decrease in slopes from drainage areas around 10^4 m^2 and below, marking the regions where landsliding reduces slopes. In the models where R_W is constant, the hillslope slopes progressively decrease with each increase in R_W. In contrast, the change in calculated R_W is more dramatic: it appears that once recharge is large enough to saturate only the hollows (A~10^3-10^4 m^2) landsliding occurs and alters the landscape similarly to the fully saturated case. This suggests that landsliding processes do not substantially further alter the slope-area relationship if more of the hillslopes and ridges are saturated. These results are consistent with the model results of Tucker and Bras (1998) who implemented a pseudo-landsliding scheme controlled by similar underlying failure criteria and steady state runoff flow estimations, and observed a similar depression in the slopes within the hollows prone to landsliding, producing a similar step-like form in the slope area plot.

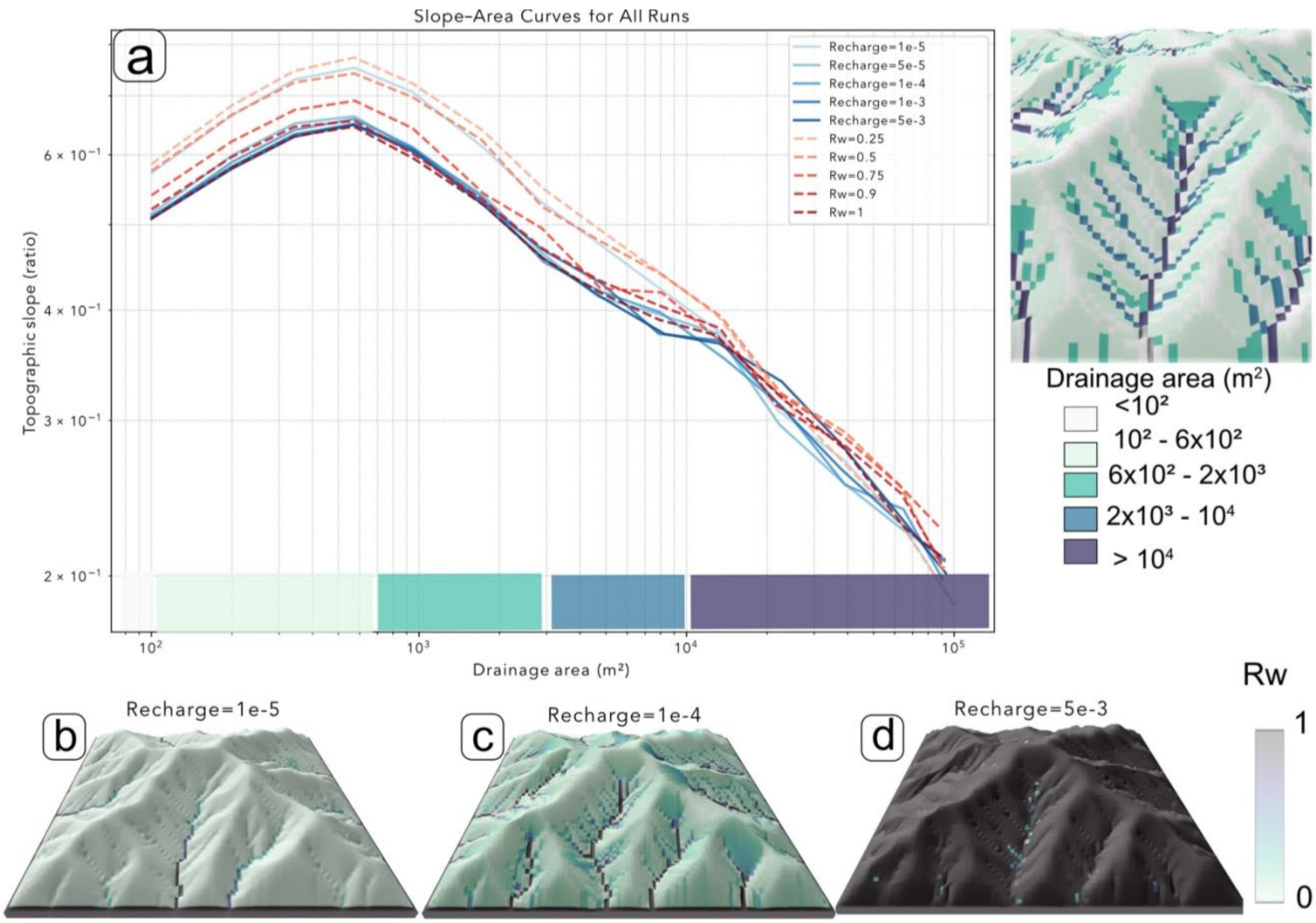

Figure 2.6: Comparison of models implementing SoilLandslider with different input R_W estimations. (a) is a slope area plot with area-bin averaged slope values, plotted for all models with varying recharge values(cool tones solid lines) and varying constant R_W values (warm tones, dashed lines). Drainage area values are color coded to match hillslope transport regimes and highlighted in the inset illustrative plot. (b-d) illustrate the resultant R_W estimates using a simple steady state topographically constrained groundwater flow equation with varying recharge values.

2.6.3 Model use

The addition of SoilLandslider to the Landlab modelling toolkit further enables customization of hillslope processes for landscape evolution models. However, with increased flexibility comes the need for choices that optimize numerical experiments to minimize computation time and reduce the number of user-defined parameters. Fortunately, the modular nature of the Landlab modelling ecosystem allows users to choose from different published modules.

The strength of SoilLandslider lies in its simplicity, and therefore in its ability to integrate with models efficiently simulating long timescales. For short timescale studies focused on real landscapes and hazard analysis, we recommend alternative modules, though this study has demonstrated the feasibility of using SoilLandslider for these applications. To identify which real hillslope slopes are unstable for shallow landsliding, we recommend the *LandslideProbability* component (Strauch et al., 2018). Alternatively, for earthquake-triggered landslides, ***ShallowLandslider*** (Ghoshal et al. 2025) may also be appropriate. If a hazard analysis using real slopes also requires incorporation of runout, we recommend ***MassWastingRouter*** (Keck et al., 2024), which has more realistic runout physics and can be run probabilistically to estimate runout probabilities. SoilLandslider's applications to studies on real landscapes and limitations or advantages compared to more complicated models warrant further exploration.

SoilLandslider is most appropriate for models where simplicity is important and long timescales are considered, both of which are typical when generating synthetic landscapes. When generating a landscape the user must choose which functions govern hillslopes. For example, should they use only linear diffusion on undifferentiated terrain or a model incorporating mobile regolith and landsliding?

When implementing a model with SoilLandslider it is important to consider the goals of the model and set the model parameters appropriately. Both the angle of internal friction and cohesion modify the strength parameters similarly and can be modified to make slopes unstable at specific slopes and soil depths, though the angle that slopes become unstable is not a simple relationship to these parameters. As demonstrated in section 2.6.2 the groundwater model chosen also plays an important role in setting hillslope strength and the distribution of unstable cells. While the onset of landsliding is set by the above-mentioned strength parameters, the interaction of the FS values set by these parameters and the FS stopper directly control the size of landslides. So, the FS stopper plays a strong role in controlling the total erosion of landslides via, modifying landslide size. The runout distance is modified by the runout threshold slope, however due to the nature of the model where all eroded volume runs out starting at the critical cell, most slides are connected to the river network, and the runout distances vary minimally with changing runout threshold angles.

Sediment plays an important role in landscapes, influencing river erosion rates (Guirro et al., 2025), channel widths (Inoue and Hiramatsu, 2025), hillslope form (Heimsath et al., 2005; Johnstone and Hilley, 2015) among other processes. For users simulating hillslopes in Landlab with sediment, a choice in soil production function parameters is required. Currently only the *ExponentialWeatherer* (or *ExponentialWeathererIntegrated*) components are available. No humped (Heimsath et al., 2009) soil production function module exists at this time. The primary module for hillslope soil creep is *depthdependenttaylordiffuser*. Soil depth is as important as slope for soil landslide initiation and size, so the model parameter choices surrounding soil production and creep are critical for setting landslide stability and size.

Non-linear soil transport processes may be simulated using soil landsliding via this component, DepthdependentDiffuser with a critical slope and *nterms* >1, or BedrockLandslider. Figure 2. demonstrates the similarities and differences between the first two options. If the experiment does not explicitly concern how changes to the landslide regime or fluvial sediment cover impact the landscape, we suggest that non-linear diffusion models are sufficiently accurate. However, landsliding introduces more realistic spatial variability, affects steady state river sediment cover, and may alter hillslope erosion patterns. If these effects are of interest, we suggest using

SoilLandslider. It also remains to be tested, how strongly sediment pulses derived from soil landslides influence rivers compared to continuous soil creep. Sometimes it is appropriate to simulate bedrock landslides rather than only soil landslides. Campforts et al. (2022) used BedrockLandslider to demonstrate that sediment pulses from landsliding can lead to landscapes persisting in dynamic equilibrium with constant perturbations. While BedrockLandslider and SoilLandslider are similar modules, BedrockLandslider assesses stability using only slope and ϕ and can erode soil and bedrock while SoilLandslider stability is controlled by several more parameters including soil depth, and groundwater, and only erodes soil. If simulating rapidly uplifting landscapes that may be home to large landslides, or not have a deep stable hillslope soil depth we recommend BedrockLandslider. If considering soil mantled landscapes and hillslope soil depth, debris flows, or water-based triggers we recommend SoilLandslider.

2.7 Conclusions

Here, we present a new module that simulates shallow landslides which fail only the uppermost mobile regolith or soil layer, and can be implemented on landscape evolution timescales. The SoilLandslider module identifies susceptible terrain using an infinite slope factor of safety calculation, stochastically triggers landslides from critical cells, erodes material upslope of these cells based on local stability and slope angle, and deposits this material downhill from the critical cells following a multiple flow path flow routing algorithm. We demonstrate that this model successfully identifies observed areas of landslide susceptibility, and reproduces characteristic patterns of erosion and deposition from real shallow landslides. The model is capable of generating realistic landslide inventory statistics, though it may underpredict landslide sizes at fine grid resolutions.

We further demonstrate the utility of the module through two long timescale (2 Myr) numerical experiments. In the first we show that process-based shallow landsliding can reproduce the first-order landscape characteristics commonly attributed to non-linear diffusion. In the second experiment we demonstrate the impacts of the hydrologic model choices on landscape form. We show that different hydrological regimes produce distinct spatial patterns of instability and, consequently, different topographic outcomes. These results highlight the importance of hydrologic assumptions in long term landscape evolution modelling.

More broadly, SoilLandslider represents a shift in landscape evolution modelling towards the combination of continuum landscape-form derived geomorphic functions with discrete mechanistic event scale processes. By resolving these discrete stochastic events within long-timescale simulations, models can become more grounded in physical geomorphic processes and the direct observations of these processes on human timescales. These process and event-based models offer new opportunities to investigate how the geomorphic system works at a fundamental level as an intertwined web of discrete processes and events that form the landscapes of our world.

2.8 References

Barnes, R., Lehman, C., and Mulla, D.: Priority-flood: An optimal depression-filling and watershed-labeling algorithm for digital elevation models, Comput. Geosci., 62, 117–127, https://doi.org/10.1016/j.cageo.2013.04.024, 2014.
Barnhart, K. R., Glade, R. C., Shobe, C. M., and Tucker, G. E.: Terrainbento 1.0: A Python package for multi-model analysis in long-term drainage basin evolution, Geosci. Model Dev., 12, 1267–1297, https://doi.org/10.5194/gmd-12-1267-2019, 2019.
Barnhart, K. R., Hutton, E. W. H., Tucker, G. E., M. Gasparini, N., Istanbulluoglu, E., E. J. Hobley, D., J. Lyons, N., Mouchene, M., Siddhartha Nudurupati, S., M. Adams, J., and Bandaragoda, C.: Short communication: Landlab v2.0: A software package for Earth surface dynamics, Earth Surf. Dyn., 8, 379–397, https://doi.org/10.5194/esurf-8-379-2020, 2020.
Bellugi, D., Milledge, D. G., Dietrich, W. E., Perron, J. T., and McKean, J.: Predicting shallow landslide size and location across a natural landscape: Application of a spectral clustering search algorithm, J. Geophys. Res. Earth Surf., 120, 2552–2585, https://doi.org/10.1002/2015JF003520, 2015.
Bellugi, D. G., Milledge, D. G., Cuffey, K. M., Dietrich, W. E., and Larsen, L. G.: Controls on the size distributions of shallow landslides, Proc. Natl. Acad. Sci. U. S. A., 118, https://doi.org/10.1073/pnas.2021855118, 2021.
Booth, A. M., Roering, J. J., and Rempel, A. W.: Topographic signatures and a general transport law for deep-seated landslides in a landscape evolution model, J. Geophys. Res. Earth Surf., 118, 603–624, https://doi.org/10.1002/jgrf.20051, 2013.
Broeckx, J., Rossi, M., Lijnen, K., Campforts, B., Poesen, J., and Vanmaercke, M.: Landslide mobilization rates: A global analysis and model, Earth-Science Rev., 201, 102972, https://doi.org/10.1016/j.earscirev.2019.102972, 2020.
Burns, W. J., Mickelson, K. A., and Madin, I. P.: Landslide Susceptibility Overview Map of Oregon, 2016.
Campforts, B., M. Shobe, C., Steer, P., Vanmaercke, M., Lague, D., and Braun, J.: HyLands 1.0: A hybrid landscape evolution model to simulate the impact of landslides and landslide-derived sediment on landscape evolution, Geosci. Model Dev., 13, 3863–3886, https://doi.org/10.5194/gmd-13-3863-2020, 2020.
Campforts, B., Shobe, C. M., Overeem, I., and Tucker, G. E.: The Art of Landslides: How Stochastic Mass Wasting Shapes Topography and Influences Landscape Dynamics, J. Geophys. Res. Earth Surf., 127, 1–22, https://doi.org/10.1029/2022jf006745, 2022.
Carretier, S., Martinod, P., Reich, M., and Godderis, Y.: Modelling sediment clasts transport during landscape evolution, Earth Surf. Dyn., 4, 237–251, https://doi.org/10.5194/esurf-4-237-2016, 2016.
Claessens, L., Heuvelink, G. B. M., Schoorl, J. M., and Veldkamp, A.: DEM resolution effects on shallow landslide hazard and soil redistribution modelling, Earth Surf. Process. Landforms, 30, 461–477, https://doi.org/10.1002/esp.1155, 2005.
Claessens, L., Schoorl, J. M., and Veldkamp, A.: Modelling the location of shallow landslides and their effects on landscape dynamics in large watersheds: An application for Northern New Zealand, Geomorphology, 87, 16–27, https://doi.org/10.1016/j.geomorph.2006.06.039, 2007.
Crovelli, R. A.: Probability Models for Estimation of Number and Costs of Landslides, U.S. Geol. Surv. Open-File Rep. 2000-249, 23 p. ;28 C., https://doi.org/https://doi.org/10.3133/ofr00249, 2000.
Crozier, M. J.: Landslide geomorphology: An argument for recognition, with examples from New Zealand, Geomorphology, 120, 3–15, https://doi.org/10.1016/j.geomorph.2009.09.010, 2010.
Densmore, A. L., Ellis, M. A., and Anderson, R. S.: Landsliding and the evolution of normal-fault-bounded mountains, J. Geophys. Res. Solid Earth, 103, 15203–15219, https://doi.org/10.1029/98jb00510, 1998.
DiBiase, R. A., Neely, A. B., Whipple, K. X., Heimsath, A. M., and Niemi, N. A.: Hillslope Morphology Drives Variability of Detrital 10Be Erosion Rates in Steep Landscapes, Geophys. Res. Lett., 50, 1–10, https://doi.org/10.1029/2023GL104392, 2023.
Dietrich, W. E., Wilson, C. J., Montgomery, D. R., Mckean, J., and Bauer, R.: Erosion thresholds and land surface morphology, 1992.
Egholm, D. L., Knudsen, M. F., and Sandiford, M.: Lifespan of mountain ranges scaled by feedbacks between landsliding and erosion by rivers, Nature, 498, 475–478, https://doi.org/10.1038/nature12218, 2013.
Fan, X., Scaringi, G., Korup, O., West, A. J., van Westen, C. J., Tanyas, H., Hovius, N., Hales, T. C., Jibson, R. W.,

Allstadt, K. E., Zhang, L., Evans, S. G., Xu, C., Li, G., Pei, X., Xu, Q., and Huang, R.: Earthquake-Induced Chains of Geologic Hazards: Patterns, Mechanisms, and Impacts, Rev. Geophys., 57, 421–503, https://doi.org/10.1029/2018RG000626, 2019.
Fan, X., Dufresne, A., Siva Subramanian, S., Strom, A., Hermanns, R., Tacconi Stefanelli, C., Hewitt, K., Yunus, A. P., Dunning, S., Capra, L., Geertsema, M., Miller, B., Casagli, N., Jansen, J. D., and Xu, Q.: The formation and impact of landslide dams – State of the art, Earth-Science Rev., 203, 103116, https://doi.org/10.1016/j.earscirev.2020.103116, 2020.
Furbish, D. J., Roering, J. J., Doane, T. H., Roth, D. L., Williams, S. G. W., and Abbott, A. M.: Rarefied particle motions on hillslopes – Part 1 : Theory, 539–576, 2021.
Gabel, V., Tucker, G. E., and Campforts, B.: A mathematical model for bedrock incision in near-threshold gravel-bed rivers, Earth Surf. Process. Landforms, 4168–4186, https://doi.org/10.1002/esp.5957, 2024.
Godard, V., Ollivier, V., Bellier, O., Miramont, C., Shabanian, E., Fleury, J., Benedetti, L., and Guillou, V.: Weathering-limited hillslope evolution in carbonate landscapes, Earth Planet. Sci. Lett., 446, 10–20, https://doi.org/10.1016/j.epsl.2016.04.017, 2016.
Grant, A., Wartman, J., and Abou-Jaoude, G.: Multimodal method for coseismic landslide hazard assessment, Eng. Geol., 212, 146–160, https://doi.org/10.1016/j.enggeo.2016.08.005, 2016.
Guirro, M. O., Hodge, R., Clubb, F., and Turnbull, L.: Network - Scale Dynamics of Alluvial Cover in a Mixed Bedrock - Alluvial River, https://doi.org/10.1029/2024JF007968, 2025.
Heimsath, A. M., Dietrich, W. E., Nishiizumi, K., and Finkel, R. C.: Stochastic processes of soil production and transport: Erosion rates, topographic variation and cosmogenic nuclides in the Oregon coast range, Earth Surf. Process. Landforms, 26, 531–552, https://doi.org/10.1002/esp.209, 2001.
Heimsath, A. M., Furbish, D. J., and Dietrich, W. E.: The illusion of diffusion: Field evidence for depth-dependent sediment transport, Geology, 33, 949–952, https://doi.org/10.1130/G21868.1, 2005.
Heimsath, A. M., Fink, D., and Hancock, G. R.: The 'humped' soil production function: eroding Arnhem Land, Australia, Earth Surf. Process. Landforms, 34, 1674–1684, https://doi.org/10.1002/esp.1859, 2009.
Hovius, N., Stark, C. P., and Allen, P. A.: Sediment flux from a mountain belt derived by landslide mapping, Geology, 25, 231–234, https://doi.org/10.1130/0091-7613(1997)025<0231:SFFAMB>2.3.CO;2, 1997.
Hsu, W., Byrne, T. B., Ouimet, W., Lee, Y., Chen, Y., Soest, M. Van, and Hodges, K.: Pleistocene onset of rapid , punctuated exhumation in the eastern Central Range of the Taiwan orogenic belt, 719–722, https://doi.org/10.1130/G37914.1, 2016.
Inoue, T. and Hiramatsu, Y.: Morphological and Sediment Supply Controls on Lateral Bedrock Channel Erosion, https://doi.org/10.1029/2024GL113436, 2025.
Istanbulluoglu, E. and Bras, R. L.: Vegetation-modulated landscape evolution: Effects of vegetation on landscape processes, drainage density, and topography, J. Geophys. Res. Earth Surf., 110, 1–19, https://doi.org/10.1029/2004JF000249, 2005.
Johnstone, S. A. and Hilley, G. E.: Lithologic control on the form of soil-mantled hillslopes, Geology, 43, 83–86, https://doi.org/10.1130/G36052.1, 2015.
Keck, J.: New methods for coupling climate-driven hydrology with hillslope and channel geomorphic processes at the watershed scale, Univ. Washingt. Res. Arch., Thesis, 2023.
Keck, J., Istanbulluoglu, E., Campforts, B., Tucker, G., and Horner-devine, A.: A landslide runout model for sediment transport , landscape evolution , and hazard assessment applications, 1165–1191, https://doi.org/10.5194/esurf-12-1165-2024, 2024.
Korup, O., Clague, J. J., Hermanns, R. L., Hewitt, K., Strom, A. L., and Weidinger, J. T.: Giant landslides, topography, and erosion, Earth Planet. Sci. Lett., 261, 578–589, https://doi.org/10.1016/j.epsl.2007.07.025, 2007.
Larsen, I. J. and Montgomery, D. R.: Landslide erosion coupled to tectonics and river incision, Nat. Geosci., 5, 468–473, https://doi.org/10.1038/ngeo1479, 2012.
Larsen, I. J., Montgomery, D. R., and Korup, O.: Landslide erosion controlled by hillslope material, Nat. Geosci., 3, 247–251, https://doi.org/10.1038/ngeo776, 2010.
Lehmann, P. and Or, D.: Hydromechanical triggering of landslides : From progressive local failures to mass release, 48, 1–24, https://doi.org/10.1029/2011WR010947, 2012.
Li, G., West, A. J., Densmore, A. L., Hammond, D. E., Jin, Z., Zhang, F., Wang, J., and Hilton, R. G.: Connectivity of earthquake-triggered landslides with the fluvial network: Implications for landslide sediment transport after the 2008 Wenchuan earthquake, J. Geophys. Res. Earth Surf., 121, 703–724, https://doi.org/10.1002/2015JF003718, 2016.
Little, T. A., Cox, S., Vry, J. K., and Batt, G.: Variations in exhumation level and uplift rate along the oblique-slip

Alpine fault , central Southern Alps , New Zealand, 707–723, https://doi.org/10.1130/B25500.1, 2005.
Litwin, D. G., Malatesta, L. C., and Sklar, L. S.: Hillslope diffusion and channel steepness in landscape evolution models, Earth Surf. Dyn., 13, 277–293, https://doi.org/10.5194/esurf-13-277-2025, 2025.
Malamud, B. D., Turcotte, D. L., Guzzetti, F., and Reichenbach, P.: Landslides, earthquakes, and erosion, Earth Planet. Sci. Lett., 229, 45–59, https://doi.org/10.1016/j.epsl.2004.10.018, 2004.
Martin, Y. and Church, M.: Diffusion in landscape development models: On the nature of basic transport relations, Earth Surf. Process. Landforms, 22, 273–279, https://doi.org/10.1002/(sici)1096-9837(199703)22:3<273::aid-esp755>3.0.co;2-d, 1997.
Mathews, N. W., Leshchinsky, B. A., Mirus, B. B., Olsen, M. J., and Booth, A. M.: RegionGrow3D: A Deterministic Analysis for Characterizing Discrete Three-Dimensional Landslide Source Areas on a Regional Scale, J. Geophys. Res. Earth Surf., 129, 1–29, https://doi.org/10.1029/2024JF007815, 2024.
Medwedeff, W. G., Clark, M. K., Zekkos, D., and West, A. J.: Characteristic landslide distributions: An investigation of landscape controls on landslide size, Earth Planet. Sci. Lett., 539, 116203, https://doi.org/10.1016/j.epsl.2020.116203, 2020.
Meisina, C. and Scarabelli, S.: A comparative analysis of terrain stability models for predicting shallow landslides in colluvial soils, i, 207–223, https://doi.org/10.1016/j.geomorph.2006.03.039, 2007.
Milledge, D. G., Bellugi, D., McKean, J. A., Densmore, A. L., and Dietrich, W. E.: A multidimensional stability model for predicting shallow landslide size and shape across landscapes, J. Geophys. Res. Earth Surf., 119, 2481–2504, https://doi.org/10.1002/2014JF003135, 2014.
Mirus, B. B., Belair, G. M., Martinez, S. N., Wood, N. J., and Jones, J.: Parsimonious High - Resolution Landslide Susceptibility Modeling at Continental Scales, 1–25, https://doi.org/10.1029/2024AV001214, 2024.
Monsalve, A. D., Anderson, S. R., Gasparini, N. M., and Yager, E. M.: RiverBedDynamics v1 . 0 : a Landlab component for computing two-dimensional sediment transport and river bed evolution, 3427–3451, https://doi.org/https://doi.org/10.5194/gmd-18-3427-2025, 2025.
Montgomery, D. R.: SLOPE DISTRIBUTIONS , THRESHOLD HILLSLOPES , AND STEADY-STATE TOPOGRAPHY, 301, 432–454, 2001.
Montgomery, D. R. and Brandon, M. T.: Topographic controls on erosion rates in tectonically active mountain ranges, 201, 481–489, 2002.
Montgomery, D. R. and Dietrich, W. E.: A physically based model for the topographic control on shallow landsliding, Water Resour. Res., 30, 1153–1171, https://doi.org/10.1029/93WR02979, 1994.
Montgomery, D. R., Schmidt, K. M., Greenberg, H. M., and Dietrich, W. E.: Forest clearing and regional landsliding, Geology, 28, 311–314, https://doi.org/10.1130/0091-7613(2000)28<311:FCARL>2.0.CO;2, 2000.
Montgomery, D. R., Schmidt, K. M., Dietrich, W. E., and McKean, J.: Instrumental record of debris flow initiation during natural rainfall: Implications for modeling slope stability, J. Geophys. Res. Earth Surf., 114, 1–16, https://doi.org/10.1029/2008JF001078, 2009.
Moon, S.: Journal of Geophysical Research : Earth Surface, 856–876, https://doi.org/10.1002/2014JF003387, 2015.
Morgan, P. M., Grant, A., Struble, W., Lahusen, S., and Duvall, A.: The damability function : a probabilistic approach to regional landslide dam susceptibility analysis applied to the Oregon Coast Range , USA, 1745–1766, 2026.
Perron, J. T., Dietrich, W. E., and Kirchner, J. W.: Controls on the spacing of first-order valleys, 113, 1–21, https://doi.org/10.1029/2007JF000977, 2008.
Roering, J. J., Kirchner, J. W., and Dietrich, W. E.: Evidence for nonlinear, diffusive sediment transport on hillslopes and implications for landscape morphology, Water Resour. Res., 35, 853–870, https://doi.org/10.1029/1998WR900090, 1999.
Roering, J. J., Perron, J. T., and Kirchner, J. W.: Functional relationships between denudation and hillslope form and relief, Earth Planet. Sci. Lett., 264, 245–258, https://doi.org/10.1016/j.epsl.2007.09.035, 2007.
Schmidt, K. M., Roering, J. J., Stock, J. D., Dietrich, W. E., Montgomery, D. R., and Schaub, T.: The variability of root cohesion as an influence on shallow landslide susceptibility in the Oregon Coast Range, Can. Geotech. J., 38, 995–1024, https://doi.org/10.1139/cgj-38-5-995, 2001.
Sharifi-Mood, M., Olsen, M. J., Gillins, D. T., and Mahalingam, R.: Performance-based, seismically-induced landslide hazard mapping of Western Oregon, Soil Dyn. Earthq. Eng., 103, 38–54, https://doi.org/10.1016/j.soildyn.2017.09.012, 2017.
Shobe, C. M., Tucker, G. E., and Barnhart, K. R.: The SPACE 1.0 model: A Landlab component for 2-D calculation of sediment transport, bedrock erosion, and landscape evolution, Geosci. Model Dev., 10, 4577–4604, https://doi.org/10.5194/gmd-10-4577-2017, 2017.

Strauch, R., Istanbulluoglu, E., Siddhartha Nudurupati, S., Bandaragoda, C., Gasparini, N. M., and Tucker, G. E.: A hydroclimatological approach to predicting regional landslide probability using Landlab, Earth Surf. Dyn., 6, 49–75, https://doi.org/10.5194/esurf-6-49-2018, 2018.
Struble, W. T., Roering, J. J., Burns, W. J., Calhoun, N. C., Wetherell, L. R., and Black, B. A.: The Preservation of Climate-Driven Landslide Dams in Western Oregon, J. Geophys. Res. Earth Surf., 126, 1–25, https://doi.org/10.1029/2020JF005908, 2021.
Tanyaş, H., van Westen, C. J., Allstadt, K. E., and Jibson, R. W.: Factors controlling landslide frequency–area distributions, Earth Surf. Process. Landforms, 44, 900–917, https://doi.org/10.1002/esp.4543, 2019.
Theodoratos, N., Seybold, H., and Kirchner, J. W.: Scaling and similarity of a stream-power incision and linear diffusion landscape evolution model, 779–808, 2018.
Tucker, G. E. and Bras, R. L.: Hillslope processes, drainage density, and landscape morphology, Water Resour. Res., 34, 2751–2764, https://doi.org/10.1029/98WR01474, 1998.
Tucker, G. E. and Hancock, G. R.: Modelling landscape evolution, Earth Surf. Process. Landforms, 35, 28–50, https://doi.org/10.1002/esp.1952, 2010.
Yanites, B. J., Mitchell, N. A., Bregy, J. C., Carlson, G. A., Cataldo, K., Holahan, M., Johnston, G. H., Nelson, A., Valenza, J., and Wanker, M.: Landslides control the spatial and temporal variation of channel width in southern Taiwan: Implications for landscape evolution and cascading hazards in steep, tectonically active landscapes, Earth Surf. Process. Landforms, 43, 1782–1797, https://doi.org/10.1002/esp.4353, 2018.

3. **Chapter 3**: Numerical landscapes reveal limits and feedbacks among slopes, soils, and shallow landslides

Abstract
Shallow soil landslides drive substantial hillslope erosion, yet their capacity to erode is not unlimited, even at steep slopes and high uplift rates. Using landscape evolution models, we explore the limits on soil landslide erosion. Through systematic variation of uplift rate, soil production rate, hillslope diffusivity, and fluvial erodibility, we model how soil depth, slope angle, and soil landslide erosion rates in a variety of simulated landscapes. We find that landscapes are partitioned into two domains: a slope-limited domain characterized by gentle slopes and deep soils where landsliding in inhibited by insufficient slopes to promote instability, and a soil-limited domain with steep slopes and shallow soils where erosion by soil landslides is limited by a lack of soil supply. We introduce two dimensionless numbers to quantify these domains: a slope number (N_{SLP}) and a soil number (N_{SD}). N_{SLP} balances uplift against erosive efficiency to predict the magnitude of landslide erosion. N_{SD} expresses the ratio between uplift and the maximum soil production rate to identify a critical transition between the slope-limited and supply-limited domains. This transition occurs at N_{SD}=0, where uplift rate equals the maximum soil production rate. We also identify two additional soil depth behaviors: (1) mean soil depth is set by the balance between uplift and depth-dependent soil production, and (2) soil-depth-driven steepening, where depth-dependent diffusion evolves steeper slopes at low soil depths to maintain steady state soil fluxes. Our results reconcile field observations of reduced shallow landslide erosion on steep slopes and emphasize that depth-dependent soil mantled geomorphic transport functions are supply limited at low soil depths. Our results underscore the importance of soil depth as a governing variable in controlling soil landslide erosion, in geomorphic transport functions for soil mantled landscapes, and in setting the transition from soil-mantled (transport-limited) hillslopes to bedrock (strength-limited) hillslopes.

3.1 Introduction

Landslides are a foundational geomorphic process that significantly influences the form and evolution of landscapes (Crozier, 2010) and in steep terrain, contributes disproportionately to hillslope erosion by mobilizing large volumes of sediment (e.g., Broeckx et al., 2020; Hovius et al., 1997). In particular, shallow landslides, which fail only the uppermost mobile regolith layer, are likely dominant agents of soil erosion in upland landscapes (Larsen et al., 2010; De Rose, 2013), as well as expensive and deadly natural disasters (Schuster and Highland, 2001). In this study, we focus specifically on these shallow failures, referred to here as soil landslides, and their geomorphic impacts.

Several geomorphic transport functions (Dietrich et al., 2003) have been defined to describe the governing processes that keep uplift and erosion in balance for landscapes in long-term topographic steady state (Tucker and Hancock, 2010). Bedrock is weathered to soil via a soil production function (Heimsath et al., 2001), and soil creeps continuously downhill as a function of slope following a diffusion function (Dietrich et al., 1995). Observations of steep planar slopes led to the development of the nonlinear diffusion function, where soil transport increases dramatically (sometimes exponentially) as the slope angle approaches a threshold hillslope (Montgomery, 2001; Montgomery and Brandon, 2002; Roering et al., 1999). Landsliding is often invoked as a dominant process responsible for this non-linear behavior, allowing landscapes to maintain near-threshold slopes even as uplift rates increase (e.g., Larsen and Montgomery, 2012).

Recent studies suggest that there is a limit to the amount of landslide erosion that can occur to balance uplift (e.g., DiBiase et al., 2023; Prancevic et al., 2020). In the San Gabriel Mountains of CA, DiBiase et al. (2023) compiled erosion rates, mapped deep-seated landslide coverage and bedrock exposures to reveal a decrease in landsliding at steep slopes coincident with the transition from landscapes with a continuous soil mantle to areas of patchy soil coverage and exposed bedrock. Multiple rainfall triggered shallow landslide inventories have also documented decreased soil landslide erosion on steep slopes (Emberson et al., 2022; Prancevic et al., 2020). Prancevic et al. (2020) suggest that existing low soil depths on steep slopes may limit the size of soil-landslides, rather than the conventional wisdom that landsliding on steep slopes controls soil depth.

Indeed, soil depth must play a central role in the processes that govern soil mantled hillslopes. Soil depth modulates soil production rates, soil creep rates, and slope stability, which in turn modulate soil formation and erosion, ultimately influencing topographic slope. The relationships, feedbacks, and limits on these processes are difficult to conceptualize on a real-world three-dimensional landscape. This motivates the use of numerical models to explore how these processes interact across a wide range of geomorphic conditions.

In this study, we implement a soil-landsliding module (Morgan, Ch. 2) within a landscape evolution model (LEM) that simulates soil mantled landscape evolution on timescales needed to reach steady-state landscape morphology. By systematically varying uplift rate, the maximum soil production rate, soil creep efficiency, and fluvial erodibility, I explore a broad parameter space representing different geomorphic regimes. We track the landscapes as they evolve, paying special attention to the slopes, soil depths, and rates of soil-landsliding that emerge. By using LEMs, we both explore the conditions when soil landsliding is maximized or limited and assess why these conditions emerge across landscapes over geologic timescales.

We find that our range of simulated landscapes fall into two landsliding domains: a slope-limited domain characterized by gentle slopes and deep soil depths where landsliding is limited by the lack of steep slopes required to drive instability, and a soil-limited domain, characterized by steep slopes and shallow soil depths, where landslide erosion is limited by the lack of soil. We use two dimensionless numbers to assess these domains: a slope number, which relates to the balance between uplift and diffusive and advective erosion, and a new soil number which relates to the predicted soil depths from the ratio between uplift and soil production. We find that a simulated landscape's soil number controls whether landslides are slope-limited or soil-limited and the slope number controls the magnitude of landslide erosion. Our models also reveal the importance of soil depth in supplying soil landslides as well as setting landscape form through feedbacks between depth-dependent geomorphic transport functions.

3.2 Landscape evolution model setup

3.2.1 Soil Landsliding

We simulate landsliding via the module SoilLandslider within the Landlab landscape evolution modeling framework (Morgan Ch. 2, Barnhart et al., 2020). The module is described in detail in Chapter 2. In SoilLandslider, landslide failure criteria are controlled by a factor of safety (FS) equation for a soil layer on an infinite slope following the form:

$$FS = \frac{Shear\ Strength}{Shear\ stress} = \frac{C + g\ \ H\ cos^2(\theta)(\rho_{soil} - R_W * \rho_{water})\ tan(\phi)}{\rho_{soil}\ g\ \ H\ \ cos(\theta)sin(\theta)} \quad \text{(Eq. 3.1)}$$

Where C is the effective cohesion (Pa or N/m^2), g is the gravitational constant (9.81 m/s^2), H is the vertical soil depth (m), θ is the slope (radians), R_W is the fraction of the vertical soil depth saturated by groundwater (1 is fully saturated), ϕ is the angle of internal friction (radians), and ρ_{soil} and ρ_{water} are the densities of soil and water respectively.

Locations of landslides are triggered stochastically on cells with unstable FS values through a specified temporal probability rate. Landslide failure then propagates uphill from the stochastically selected critical cell, failing all soil above a failure envelope defined by the slope from the critical cell. The failures propagate uphill until the failure envelope daylights or until it reaches cells more stable than a set arresting threshold (FS=5 for this study). All of the failed material then runs out downhill of the critical cell following a multiple flow path flow routing method, eventually deposited according to a depositional slope following the methodology of Campforts et al. (2020).
We run the soil landsliding module in concert with three other modules for landscape evolution to generate simulated landscapes, with uplift set to be continuous across all cells.

3.2.2 Soil production (weathering)

Bedrock is weathered into soil using the soil production function module ***ExponentialWeathererIntegrated*** (Barnhart et al., 2019), which uses an inverse-exponential function of soil thickness to define the weathering rate at any time step (Ahnert, 1976; Heimsath et al., 1997; Small et al., 1999).

$$W = P_0 e^{(-H/H_{SP})} \quad \text{(Eq. 3.2)}$$

Where the rate of soil production (here used interchangeably with weathering) is controlled by the maximum soil production rate (P_0), and the current soil depth (H) relative to a soil production decay depth (H_{SP}) with soil production increasing with decreasing soil depth.

3.2.3 *Soil creep (diffusion)*

To model diffusive soil creep of only the soil layer, we use the Landlab module ***DepthDependentTaylorDiffuser*** (Barnhart et al., 2019), which represents soil creep as diffusive transport that is modified by a depth-dependent term following the equation:

$$Q_S = (K_S H_{SS} S)\left(1 - e^{-H/H_{DD}}\right) \qquad \text{(Eq. 3.3)}$$

Where Ks is a transport coefficient with units of velocity, H_{DD} is the soil transport (*Diffusion*) decay depth, H is the soil depth, and S is slope (m/m). This module can also incorporate a Taylor expansion series to represent non-linear diffusion near critical slopes. However, in this study we represent soil creep as linear diffusion and explicitly consider soil landsliding as the primary component of a generalized non-linear diffusion term.

The first term in equation 3.3 [$Q_s = (K_s H_{DD} S)$] is analogous to a traditional diffusion equation where the product of the soil transport velocity and soil transport decay depth is equivalent to the more commonly used diffusivity coefficient (D) ($K_s \times H_{DD} = D$), in formulations where $Q_s = D \times S$ (Barnhart et al., 2019). The depth-dependent transport term $\left(1 - e^{-H/H_{DD}}\right)$ represents the adjustment to the total sediment flux made by integrating motion across a soil column with an exponential decrease in sediment transport rates with depth, and a finite depth (Johnstone and Hilley, 2015). This term acts to limit the rate of sediment transport when the soil thickness is low.

3.2.4 *Fluvial erosion and advection*

Fluvial incision through bedrock and sediment, fluvial sediment transport, and sediment deposition are modeled using the Stream Power with Alluvium Conservation and Entrainment (SPACE) module (Shobe et al., 2017), which generally follows a stream power model formulation where:

$$E_{Sfluv} = K_{Sed} A^m S^n \left(1 - e^{-H/H_{FD}}\right) \qquad \text{(Eq. 3.4)}$$

represents the sediment entrainment,

$$E_{R\,fluv} = K_{BR} A^m S^n \left(e^{-H/H_{FD}}\right) \qquad \text{(Eq. 3.5)}$$

represents bedrock erosion, and

$$D_{Sfluv} = \frac{Q_{Sfluv}}{Q} V_S \qquad \text{(Eq. 3.6)}$$

represents sediment deposition. Where K_S and K_{BR} are the erodibility constants for sediment and bedrock respectively (m^{-1}), A is the drainage area (m^2), S is the channel slope (m/m), H is the sediment thickness in the river (m), H_{FD} is the fluvial depth decay scale (m), m is the drainage area exponent, n is the slope exponent, D_{Sfluv} is the sediment deposition flux (m^3/yr), Q_{sfluv} is the sediment flux (m^3/yr), Q is the river flux(m^3/s), and V_S is the effective settling velocity scale (m/s).

In our experiment we use mathematical formulations derived for a simple stream power model, so we set m=0.5, n=1, and V_S and K_{Sed} to high values [V_S=0.1 K_{Sed}=0.0001] so that river sediment is eroded and transported, keeping the model detachment-limited and analogous to stream power models that do not include sediment cover. Further exploration into sediment feedbacks is within the fluvial system is beyond the scope of this study, but these effects should be explored in future work.

3.2.5 Experimental design

Our goal is to understand the erosional regimes where soil landsliding occurs, and whether there is a limit to soil landsliding at high slopes. To accomplish this, we run a suite of landscape evolution models simulating a large set of landscape dynamics. We have identified four key variables to vary across our model runs to represent the simulated processes at play. We vary uplift rate (U) as a primary modulator of the total erosion rate, bedrock erodibility (K_{BR}) as the primary modulator of fluvial erosion, soil transport velocity (Ks) as a modulator of soil creep (diffusivity), and the maximum weathering rate (P_0) to modulate the strength of soil production.

All models were run on 100 by 100 cell model grids with entirely open edges, with a cell size of 10m by 10m, and time step length of 10 years for a total run time of 2 million years. Nearly all the models evolved to a dynamic steady state, where the mean elevation of all the cells does not change with time, though individual cell elevations are not entirely static due to stochastic landsliding. Across all landscape simulations we keep the parameters for landsliding constant, and thus the amount of landslide erosion recorded by each model run is emergent from the landscape evolution model parameters. We run the numerical models in two phases. In Phase 1 (79 individual models – see Table S3.1), we explore a wide range of parameters for the four variables in question. Then, in Phase 2, we run sets of numerical models where we keep specific dimensionless numbers constant to probe the relationships between slope, soil depth, and landslide erosion (44 model simulations, Table S3.2).

3.3 Theoretical controls on slope and soil depth

The primary ingredients for soil landsliding are soil, steep slopes, and a temporary loading factor. The loading from water, or instability induced by seismic shaking are the main factors that vary human timescales, and thus are often explored thoroughly in susceptibility analyses. On the thousands of years timescales we may exceed the return interval of these temporary loading factors allowing them to be approximated as constant in time across our models. To quantify the other two variables, emergent mean slopes and soil depths across a landscape, we consider two dimensionless parameters described below. Our goal is to identify predictors for landsliding in modelled landscapes based on input parameters.

3.3.1 Slope number N_{SLP}

The resultant slopes of a landscape evolved to topographic steady state are a function of the balance between uplift and erosion. When a model is in steady state the erosion at each cell equals the uplift at that cell, and landscapes evolve towards equilibrium through the adjustment of slopes which modulate the erosional processes. Both diffusive soil creep processes and fluvial advection or incision increase with increasing slopes.

To define this balance between uplift and erosion we adopt the characteristic gradient defined by Theodoratos et al., (2018), which we term the slope number N_{SLP}, defined as:

$$N_{SLP} = \frac{h_c}{\ell_c} = \frac{U}{\sqrt{D\,K}} = \frac{U}{\sqrt{(K_s H_{DD})(K_{BR})}} \qquad (Eq. 3.7)$$

Where U is the uplift rate (LT^{-1}), D is the diffusivity (in our model $K_s H_{DD}$), K is the fluvial erodibility (in our model K_{BR}), h_c and ℓ_c are the critical height and critical length scales also defined by (Theodoratos et al., 2018), which is only true for the simplified case where the fluvial erosion exponents are n=1 and m=0.5

N_{SLP} is directly proportional to the uplift and inversely proportional to the root of the hillslope diffusivity and the fluvial erodibility. When uplift rate increases, N_{SLP} increases, as a steeper slope is needed to erode at a faster rate. If either erosional process increases in efficiency, the slope number decreases, as the same erosion rate can be accomplished at lower slopes.

The critical height scale [h_c = U/K] has been used to scale the steady state value of the channel steepness index (Whipple, 2001), which has been shown to scale relief (Sklar and Dietrich, 1998, Perron and Royden, 2013). The critical length scale [ℓ_c=$\sqrt{D}$/$\sqrt{K}$] derived by Perron et al. (2008) defines the point where the timescales for hillslope diffusion and fluvial advection are equal, more generally representing the competition between fluvial incision and hillslope diffusion. This parameter has been used in dimensional analysis concerning stream power and diffusion models as a characteristic length scale (e.g., Duvall and Tucker, 2016; Litwin et al., 2025; Theodoratos et al., 2018).

3.3.2 Soil number N_{SD}

The soil depth of a landscape in steady state reflects a balance between the rate of uplifting bedrock, the conversion rate of bedrock to soil, and the diffusive flux of soil in and out of each location. At the landscape scale, soil depth has been shown to correlate with topographic curvature due to the convergence or divergence of diffusive transport paths (Patton et al., 2018). However, to predict the soil depth landscape wide, we consider the soil production function. In a steady state landscape, the soil production rate will equal the bedrock uplift rate. The soil production rate at a given point is controlled by the soil production function, which is a function of soil depth. Shallower soil depths lead to faster soil production up to the soil production maximum rate P_0. As such, when uplift rate is less than P_0 there exists a soil depth at which the soil production rate is equal to the uplift rate.

The soil depth at which this balance occurs (H_{steady}) can be solved for by setting uplift rate equal to the weathering rate in Eq. 2 and solving for H (Campforts et al., 2022):

$$H_{steady} = -H_{SP}\ ln\left({}^{U}/_{P_0}\right) \qquad (Eq. 3.8)$$

Where H_{steady} is the steady state soil depth, H_{SP} is the soil production decay depth, U is uplift, and P_0 is the soil production maximum rate. To non-dimensionalize this equation we divide by H_{SP}, representing the steady state soil depth relative to the depth decay scale to find an expression for the soil number N_{SD}: (Note: the fraction flips to remove the negative sign preceding the ln)

$$N_{SD} = ln\left({}^{P_0}/_{U}\right) \qquad (Eq. 3.9)$$

When U is less than P_0 the N_{SD} value is positive and linearly correlated to the predicted soil depth. When U equals P_0 $N_{SD} = 0$, which marks a predicted soil depth of zero, an important inflection point is reached. When U is greater than P_0 the N_{SD} value becomes negative, and soil production alone no longer keeps pace with bedrock uplift, requiring other processes to account for the erosion. In these cases, soil depth predictions break down, which may represent where landscapes transition from soil mantled to bedrock dominated, or from transport-limited to strength-limited (Schlunegger et al., 2013). However, some studies have shown that the transition to bedrock landscapes is not binary but occurs over a transition zone (DiBiase et al., 2023; Heimsath et al., 2012). Nonetheless, we consider the point where P_0 equals U of interest and refer to it throughout this study as the N_{SD} zero point.

3.4 Results

3.4.1 Models recreate reduced soil erosion at high slopes

Figure shows landslide erosion rate vs mean slope angle for phase 1 model results (K_S, K_{BR}, P_0, and U systematically varied, see detailed table S1). We calculated landslide erosion rate by tracking the volume of soil eroded and transported by each landslide and by dividing the cumulative landslide volume by total model run times. We measured topographic slopes of the model grid at the final timestep. We recorded the mean slope of all cells with a drainage area < 10^4 m^2, an identified transition from diffusive to advective processes for many of the models. The plot reveals systematic changes in morphology and landsliding. Landscapes characterized by shallow slopes with mean slopes less than 30° (labeled "Slope-limited" in Figure 3.1) have little to no landslide erosion. Between ~30° and 40-45° landslide erosion increases with increasing mean slopes. Models with steep slopes > 40-45° (labeled as "Soil-limited") show decreasing landslide erosion correlative with increasing slopes.

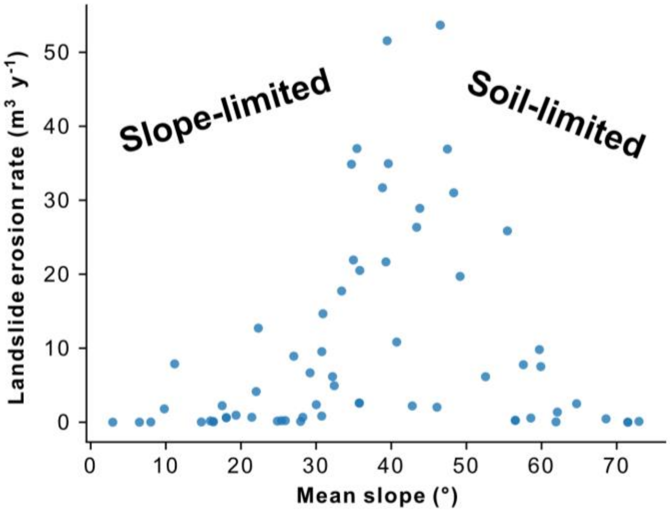

Figure 3.1: Landslide erosion rates and mean hillslope slopes reveal two landsliding domains. The landslide erosion rate (total volume of landslide material divided by total model time) and mean hillslope (mean slopes for all cells with drainage area less than 10^4 m^2). Landslide erosion generally increases with increasing slopes up to ~40 degrees revealing the slope limited domain. Landslide erosion decreases with increasing slopes above 40 degrees revealing the soil limited domain.

The simulated soil depth also varies systematically with slope (Fig. 3.2). Mean soil depth was recorded for all cells with drainage areas < 10^4 m^2 on the final model timestep. Soil depth exponentially decreases as slope increases ($R^2 = 0.80$, Fig. 3.2).

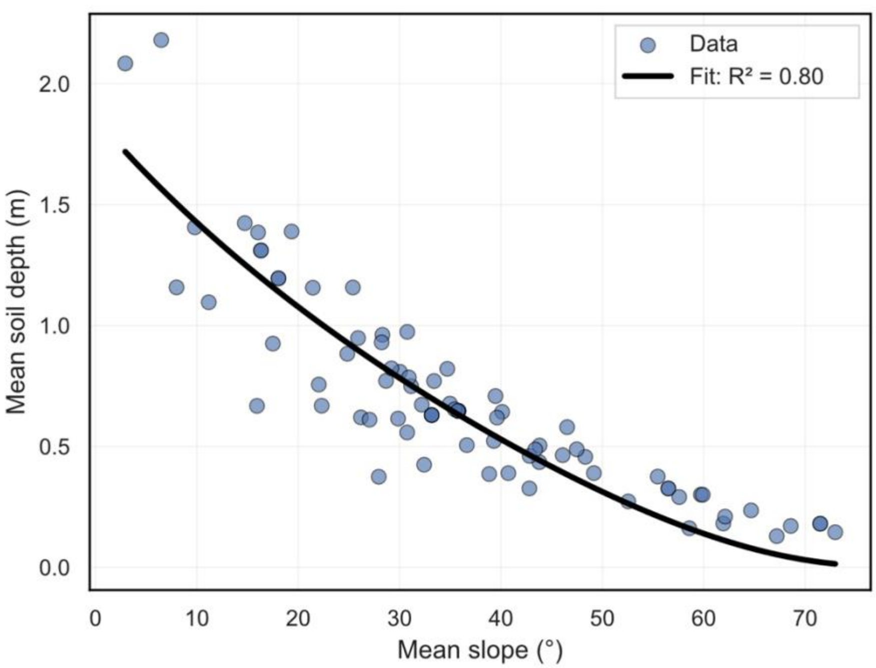

Figure 3.2: Simulated mean hillslope soil depths vary systematically with mean hillslope slopes. The fit is by an exponential line $Y=1.86e^{(-1.5x)}$

The soil depth, slope, and landslide erosion values together demarcate two distinct limits on landsliding. At low slopes, in the slope-limited domain, the landscape has enough soil to fail in a landslide, but the slope is not steep enough to be unstable and trigger mass movement. Landslide frequency only increases as mean slopes approach ~ 30° (Fig. 3.3c), and then landslide frequency increases with increasing slope until very high slopes (Fig. 3.3c). However, beyond steep slopes of ~30 degrees, in the soil-limited domain individual landslide areas begin to decrease in size (Fig. 3.3e), which correlates well with decreasing soil depth (Fig. 3.3f). Though landslide frequency decreases in models with the steepest slopes, landslide erosion volume begins to decrease while landslide frequency is still high. This may be a function of low soil depths limiting the size of landslides at steep slopes and thus defining a soil-limited, or supply-limited landsliding domain.

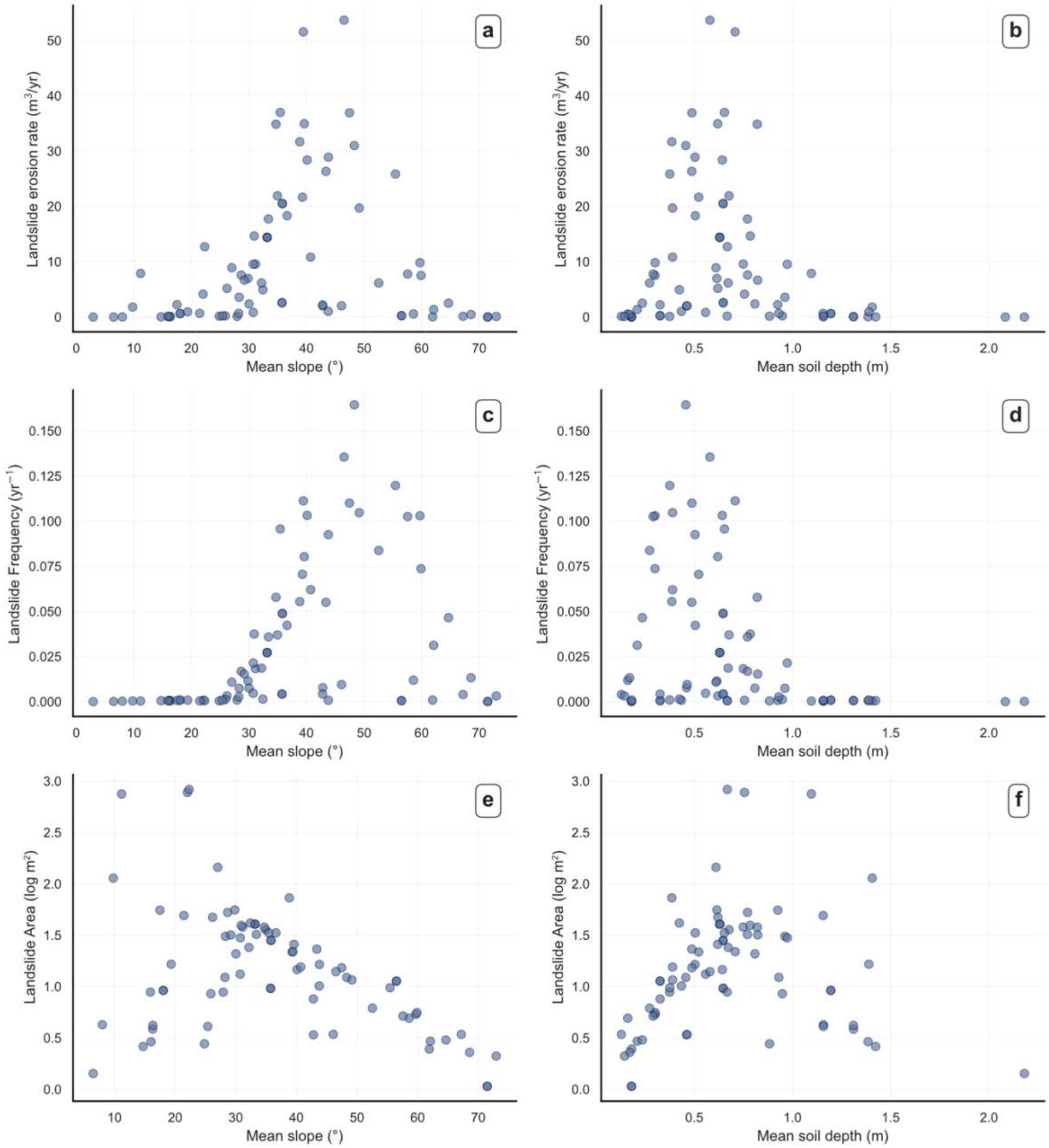

Figure 3.3: Phase one landscape evolution models comparing total landslide erosion, landslide frequency, and landslide size as a function of mean slope or soil depth. The x axis in (a), (c), and (e) is the mean slope of all cells in the model grid, the x axis in (b), (d), and (f) is the mean soil depth for all cells with drainage area less than 10^4 m^2. The y axis for (a) and (b) is the landslide erosion rate, the total volume moved by landslides divided by the total time. The y axis for (b) and (c) is the total number of landslides divided by the total model time. The y axis for (e) and (f) is the lognormal mean for the distribution of individual landslide areas for all landslides in the model runs.

3.4.2 *The slope number and soil number capture landscape attributes*

Figure 3.4 demonstrates that $\boldsymbol{N_{SLP}}$ and $\boldsymbol{N_{SD}}$ track the modelled slopes and soil depths for the phase 1 modelled landscapes. For slopes <30° N_{SLP} generally correlates positively with slope. Above 30°, only models with $N_{SD} > 0$ (reddish dots in Fig. 3.4a) continue to scale linearly with N_{SLP}, whereas models with $N_{SD} < 0$ (gray scale dots in Fig. 3.4a) correlate with steep slopes, without especially large N_{SLP} values. Above around 30 degrees, or N_{SLP} values from 2 to 4, modelled slope appears to correlate better with the N_{SD} values (Darker greys = steeper slopes) than with the slope number (left and right on the x axis).

The soil depth values also correlate with the N_{SD} numbers (Fig. 3.4b), with less noise than the slope numbers. Deeper mean soil depths correlate with higher N_{SD} numbers, where uplift is less than P_0, and match the soil depths predicted by Eq. 3.8. The relationship between soil depth and NSD appears linear from high N_{SD} values down to the N_{SD} zero point. At negative N_{SD} values, models where $U > P_0$ simulated soil depth values are low, depart from the linear trend in soil depths and the predicted soil depth values. Model output soil depths cannot be negative, while the predicted soil depths can. In general, there is relatively little apparent relationship between the soil depth and N_{SLP} values, though most of the low N_{SD} values also match higher N_{SLP} values.

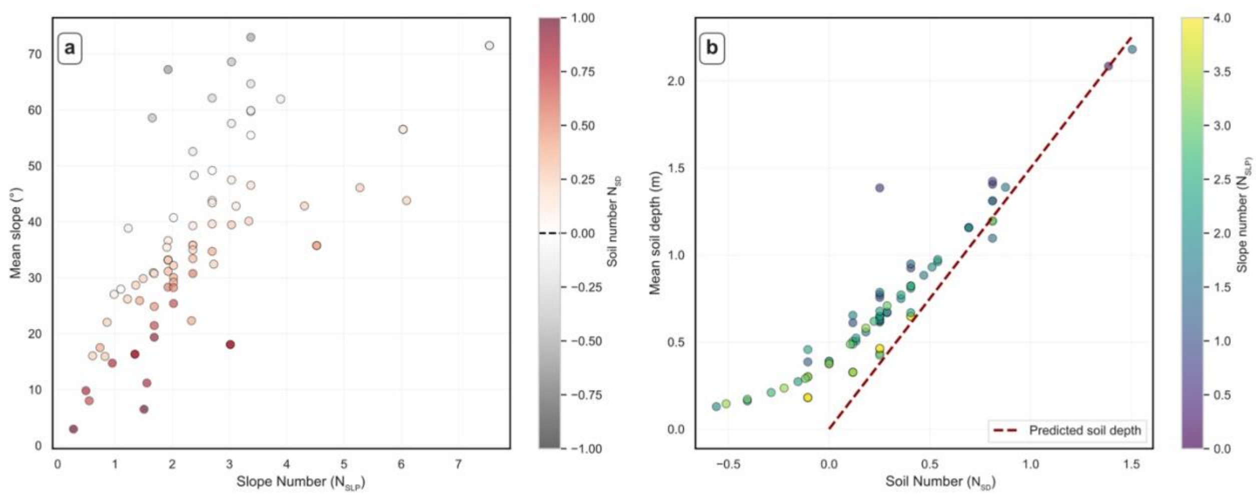

Figure 3.4: The slope number N_{SLP} and the soil number N_{SD} compared to the model values they represent. (a) shows the mean hillslope slopes compared with the slope number and colored by the soil number. (b) shows the mean soil depths (also for cells with less than 10^4 m^2 drainage area) compared with the N_{SD}, and colored by N_{SLP}. Also shown as a dashed brown line are the predicted soil depths by equation 9.

3.4.3 *The slope number and soil number reveal landsliding domains*

In phase 2 of the numerical experiment, sets of models were run to explore N_{SLP} and relative controls on landsliding. We keep the diffusivity (via K_S) and the fluvial erodibility (via K_{BR}) constant for these model runs (see Table S2).

Figure 3.5a shows how landslide erosion varies with N_{SLP} for landscapes with three different N_{SD} values (-0.12, 0.12, and 0.47 the ratio between weathering and uplift is held constant across variable uplift rates). Landscapes with negative N_{SD} values (low soil depths, grey dots), have relatively low landslide erosion for model runs across the three slope numbers. For models with low positive N_{SD} values (intermediate soil depths, orange dots), landslide erosion increases linearly with increasing N_{SLP}. For models with larger N_{SD} values (deep soil depths, red dots), no landsliding is observed until a threshold N_{SLP} value, and then landsliding increases generally linearly with increasing N_{SLP}.

Figure 3.5b shows how landslide erosion varies with N_{SD} for models with three different N_{SLP} values (1.6, 2.3, and 3). In each set of models uplift rate, diffusivity, and fluvial erodibility are held constant, while the maximum weathering rate (P_0) varies. All model sets have a central peak, with low landslide erosion at high N_{SD} values where the deepest soil depths are predicted. Landslide erosion increases as the N_{SD} decreases until a value slightly above zero. Where N_{SD} is near or slightly higher than zero, landslide erosion decreases with decreasing (more negative) values. The height of the peak correlates with the N_{SLP} value, with greater N_{SLP} values achieving greater landslide erosion.

Together these models reveal how slope and soil depth limit landslide erosion. The soil depth sets the landscapes' landsliding domain, with positive N_{SD} values matching the slope limited domain and negative N_{SD} values in the soil limited domain. For models in the slope limited domain, landslide erosion increases with slope number, whereas models in the soil limited domain show that variable slope number has little impact on landsliding. Instead, increasing the N_{SD} leads to an increase in landsliding.

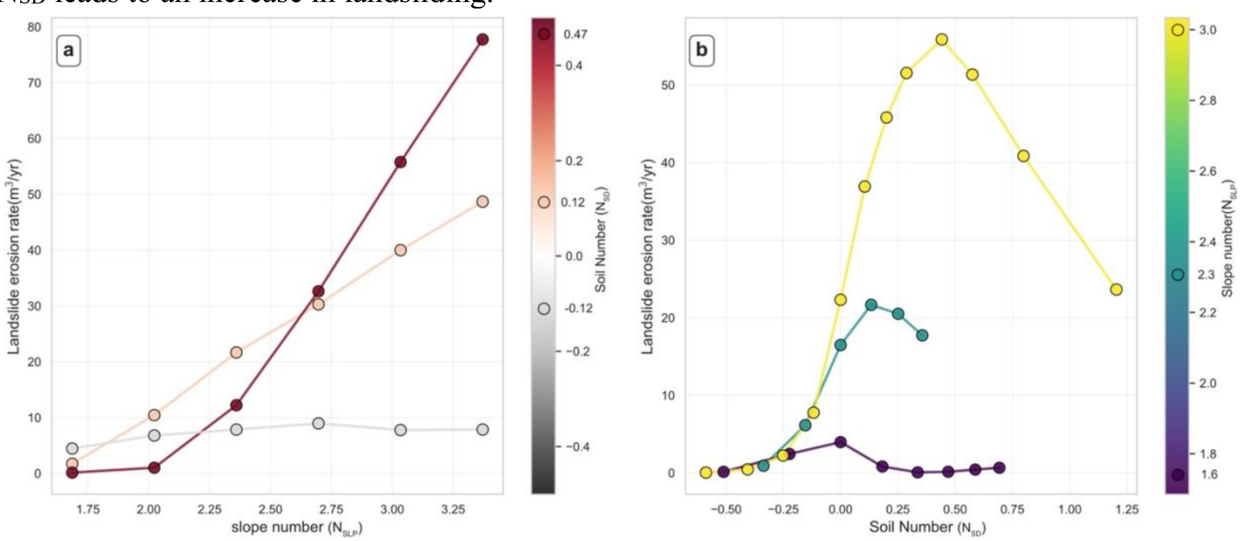

Figure 3.5: Phase 2 numerical experiments reveal the relationship between N_{SD}, N_{SLP}, and landslide erosion magnitude and domain position. (a) show experiments that vary N_{SLP} but keep the N_{SD} constant by covarying U and P_0. Landslide erosion increases with increasing N_{SLP} only for models with positive soil numbers. (b) shows experiments with varying N_{SD} but constant N_{SLP}, by keeping U constant and varying P_0. Landslide erosion is low for all models with negative N_{SD} values. At larger N_{SD} values more landslide erosion correlates with larger N_{SLP} values.

The peak landslide erosion values for a given slope number occur at soil numbers slightly above zero. As a result, N_{SD} sets the landslide domain position, and N_{SLP} sets the amplitude of the landslide erosion signal (Figure 3.5).

3.5 Discussion

Motivated by the counterintuitive observations of reduced soil landslide erosion on steep slopes (Prancevic et al., 2020), we generated many landscape evolution models to explore the limits of soil landslide erosion, and their underlying causes. Our model results match the field observations showing decreased soil landslide erosion at steep slopes, due to decreased soil depths.

A set of model runs in which only uplift is varied (Fig. 3.6), analogous to catchments within a mountain range with an uplift gradient, helps to illustrate the limits on soil landsliding. At low uplift rates (Fig. 3.6a circle) landscapes are characterized by shallow slopes, as predicted by the slope number (Eq. 3.7) (Fig. 3.6b). Such slopes are not steep enough to initiate landslide failures and hence landslide erosion is low. Landslide erosion and slopes increase as the uplift rate increases, up to a point (Fig. 3.6a triangle) because uplift rate is also inversely related to soil depth (Eq. 3.8). At soil depths around 0.5 m landslide erosion begins to decrease with increasing uplift, as both soil depths and landslide size decrease and hillslopes stabilize (Fig. 3.6c star). Landslide erosion decreases especially rapidly for models where the uplift rate is higher than the maximum weathering rate P_0 (Fig. 3.6a), which is the N_{SD} zero point (Fig. 3.6c). Soil landsliding is slope limited for landscapes where N_{SD} is positive, and soil-limited where N_{SD} is negative (Fig. 3.6).

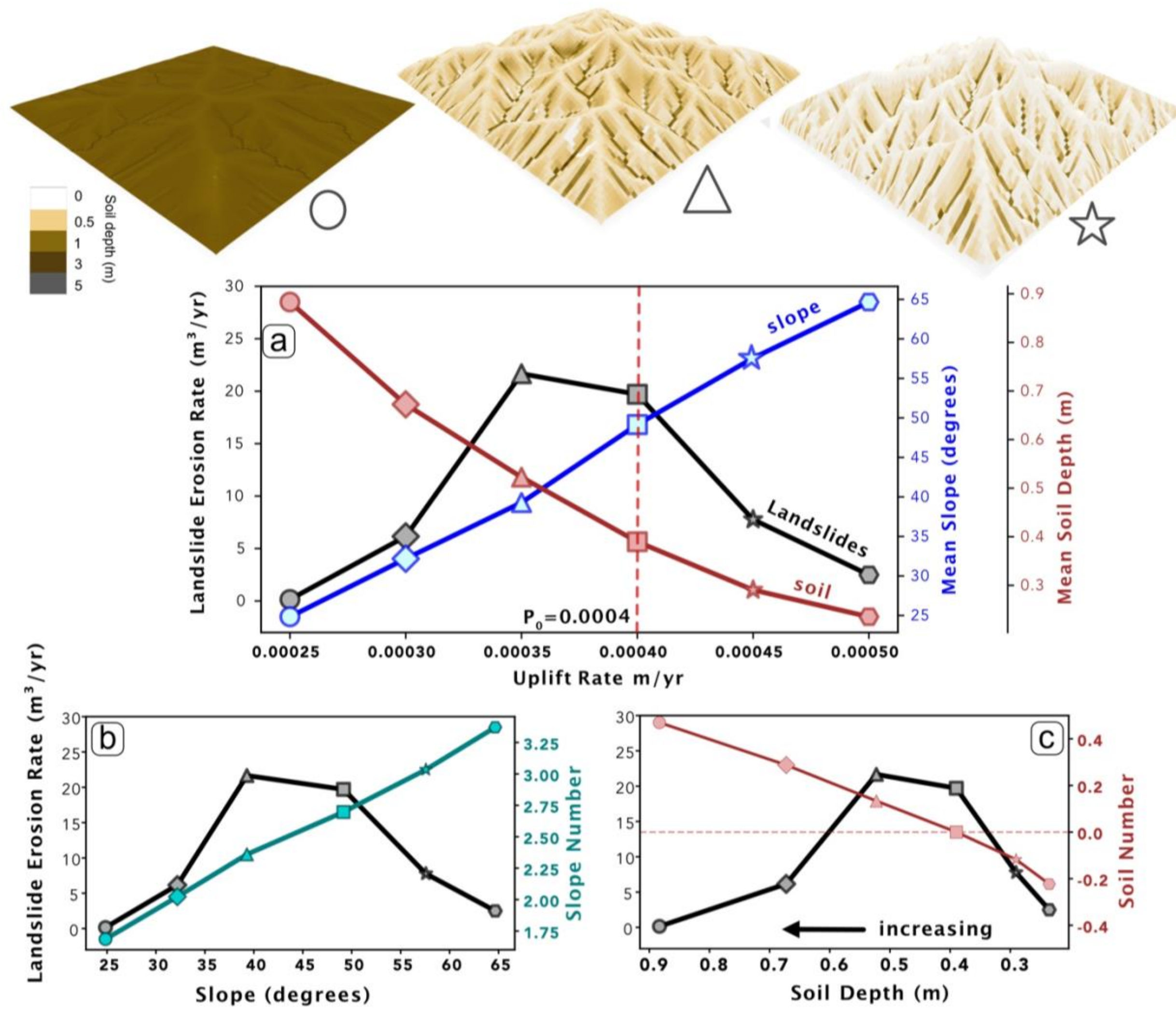

Figure 3.6: Results from a set of model runs in which uplift is the only parameter varied. Top landscapes are the final timestep landscapes with topography represented in three dimensions and soil depth represented with color. (a) shows how landslide erosion rate (black line, left y axis), mean slope (blue line, first right y axis), and mean soil depth (red line, second right axis) vary with uplift rate across the set of models. (b) and (c) show the same set of models but with different x axis. In (b) the x axis is the mean slope for all cells in the model grid, right y axis and teal line is the slope number N_{SLP} and left y axis and black line is landslide erosion, the same as a. In (c) the x axis is the mean soil depth for hillslope cells in the models, with higher depths on the left and lower depths on the right. The right y axis and red line are the soil number NSD, and the left y axis and black line are the same as in (a) and (b). Red dashed line shows the point where $U = P_0$, or the N_{SD} zero point.

The relationship between uplift rates and slope for steady state landscapes is clear in this model, and well documented for natural landscapes (Ouimet et al., 2009). Perhaps less well explored is the relationship between uplift and soil depth, that we observe acts as a limit to landsliding at steep slopes. We suggest that this relationship between soil depth, uplift, and the maximum weathering rate as described by Eq. 3.8 and represented by N_{SD}, is the causal determiner of mean soil depths across a landscape and, importantly, that soil depth acts as a universal modulator for soil mantled landscapes. In the next section (3.5.1) we discuss the implications of these depth-dependencies for simulated landscapes and then we compare these to real-world landscape observations (3.5.2).

3.5.1 Soil depth dependencies of soil-mantled transport functions

All the geomorphic transport functions we used to simulate a soil mantled landscapes depend on soil depth (Figure 3.7). As soil depth decreases, soil production rates increase (up to the P_0, Fig. 3.7a), soil creep decreases (Fig. 3.7b), and landslide stability increases (Fig. 3.7c).

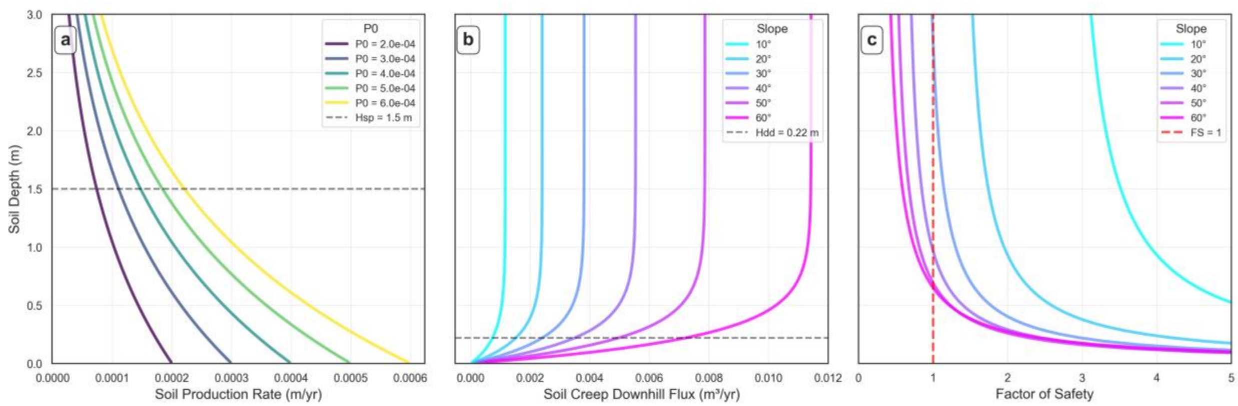

Figure 3.7: The depth-dependent geomorphic transport functions. (a) shows how soil production varies with soil depth and P0 following the exponential decay soil production function. (b) show how the downhill soil flux varies with soil depth at different slopes following the depth-dependent diffusion function, defined by linear diffusion and a soil creep decay depth of 0.22m. (c) shows how the factor of safety for shallow landsliding changes with soil depth at different slopes following the strength parameters we use in the models.

<u>The soil production function and soil depths</u>

Based on the linear relationship between the soil number and predicted and simulated soil depths, soil production appears to exert a primary control on hillslope soil depth for landscapes in a topographic steady state.

For a steady-state landscape, the amount of uplifted bedrock each timestep must balance the amount of that rock that is weathered each timestep (U=W), otherwise the topography will not remain steady. The rate of weathering is modulated by soil depth and P_0 according to the soil production function. For three landscapes with a constant uplift rate but variable P_0 values we expect different soil depths (Fig. 3.8). Note that this is analogous to three landscapes with different uplift values but a constant P_0 (such as in Fig. 3.6).

In our models, the mechanisms that adjust soil depth to balance weathering and uplift through soil depth must be feedbacks between slope and soil creep flux rates. For example, if a cell is weathering less bedrock than the uplift rate, its elevation should increase, altering the soil creep fluxes, and thus decreasing the soil depth in order to increase the weathering rate. The mechanisms of these feedbacks should be examined in further detail to identify where this relationship may be appropriate in natural landscapes.

Evaluating if this soil production defined soil depth persists across natural landscapes is challenging, as few landscapes have recorded soil production maximum rates, soil production decay depths, and erosion values that are considered equivalent to uplift. Variations in soil production rate likely alter the morphology of escarpment retreat in Madagascar (Wang et al., 2023), explain high topographic relief in carbonate landscapes in the Mediterranean (Godard et al., 2016), and may regulate hillslope length in Northern California (Pedrazas et al., 2021). Soil production rates play an integral part of geomorphic stability or instability from the scale of a single soil pit to full mountain ranges (Phillips, 2005)

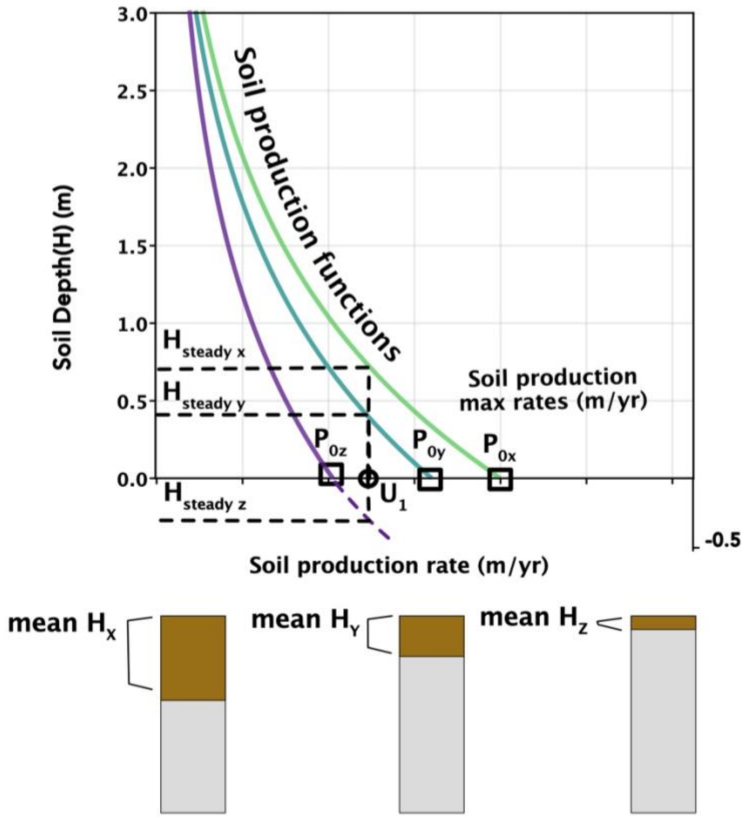

Figure 3.8: Demonstration of soil production defined soil depths for steady state landscapes. We use a plot of three soil production functions (x,y and z) defined by different P_0 values, representing the relationship between the weathering rate and the soil depth. For steady state landscapes U =W so the point where U lines up with the soil production function defines the steady state soil depth. Three landscapes defined by the same U (U_1) but different P_0 values, will have predicted and model simulated soil depths according to the diagram.

Depth-dependent diffusion and soil-depth-driven steepening

Diffusive soil creep through disturbance driven processes is likely depth-dependent. Several studies document observations consistent with depth-dependent sediment flux (Heimsath et al., 2005; Johnstone and Hilley, 2015; West et al., 2014). We model soil creep using a function that incorporates an exponential form to the diffusion rate profile simulating faster creep rates near the surface than at depth (Barnhart et al., 2019; Johnstone and Hilley, 2015). Key to our findings, the function integrates this creep rate across the total depth to get a flux. This allows for fluxes to remain relatively constant for a constant slope at high soil depths but limits the flux when the soil depth is low relative to the soil creep decay depth parameter (Fig. 3.7). Thus, at shallow soil depths, the total soil flux decreases and the effective diffusivity decreases.

As a thought experiment, we consider two hillslope cells that exist in the same hillslope position (distance from the ridge) for two models with identical uplift and diffusivity values, but with different soil depths (Figure 3.9). In steady state, both cells would have identical fluxes, as the soil flux out of a cell is proportional to the distance from the ridge and the uplift rate. However, the cell with shallower soil depth has an *effective* diffusivity lower than the cell with deep soil because the shallow soil cell adjusts to a steeper slope to maintain equivalent flux to the deep soil cell (demonstrated in Fig. 3.9 for three models). We term this feedback cycle, *soil-depth driven steepening*.

We suggest that soil-depth driven steepening is the primary driver of the correlation between simulated soil depths and mean slopes on the hillslopes in our models (Fig. 3.2). We also suggest that this feedback is why the slope number correlates with slopes, but only for models with high N_{SD} values, and that low N_{SD} values consistently correlate with the highest slopes (Fig. 3.3). Soil-depth driven steepening may also explain why there is a peak in the plots of landslide erosion with N_{SD} (Fig. 3.5b) even for models with low slope numbers, because regardless of the slope number, at low soil depth, soil-depth driven steepening generates slopes steep enough for landslide failures.

Our model results show a clear correlation of soil depth with hillslope angle. Johnstone and Hilley (2015) observed steepened hillslope sections within soil mantled slopes in California and attributed it to the same soil-depth driven steepening, as caused by different P_0 values across lithologic changes. Brosens et al., (2020) observed a similar relationship between slope and soil depth in their observations in Brazil. They observed an exponential decline in soil depth with increasing slope and attributed this to a soil-depth driven steepening feedback cycle. More research into the fitting parameters and the form of this exponential function may relate to the ratio of the decay depths for soil production and/or soil creep, diffusivity values or more aspects of the hillslope system that may be parameterized by similar measurements.

While soil-depth driven steepening is the natural progression of the geomorphic transport functions we use, in natural landscapes other processes not accounted for may take over at low soil depths or steep slopes where this effect is greatest. In one site where depth-dependent diffusion was observed via ^{10}Be based soil flux estimates for two populations of hillslopes, shallower soil depths actually occurred on less steep slopes (West et al., 2014). This was attributed to these slopes' much greater diffusivity value than the steeper slopes, due to their aspect. More studies are needed to investigate the limits of soil-depth-driven steepening in natural landscapes, and caution should be used when using a depth-dependent transport function for a landscape evolution model with low soil depths.

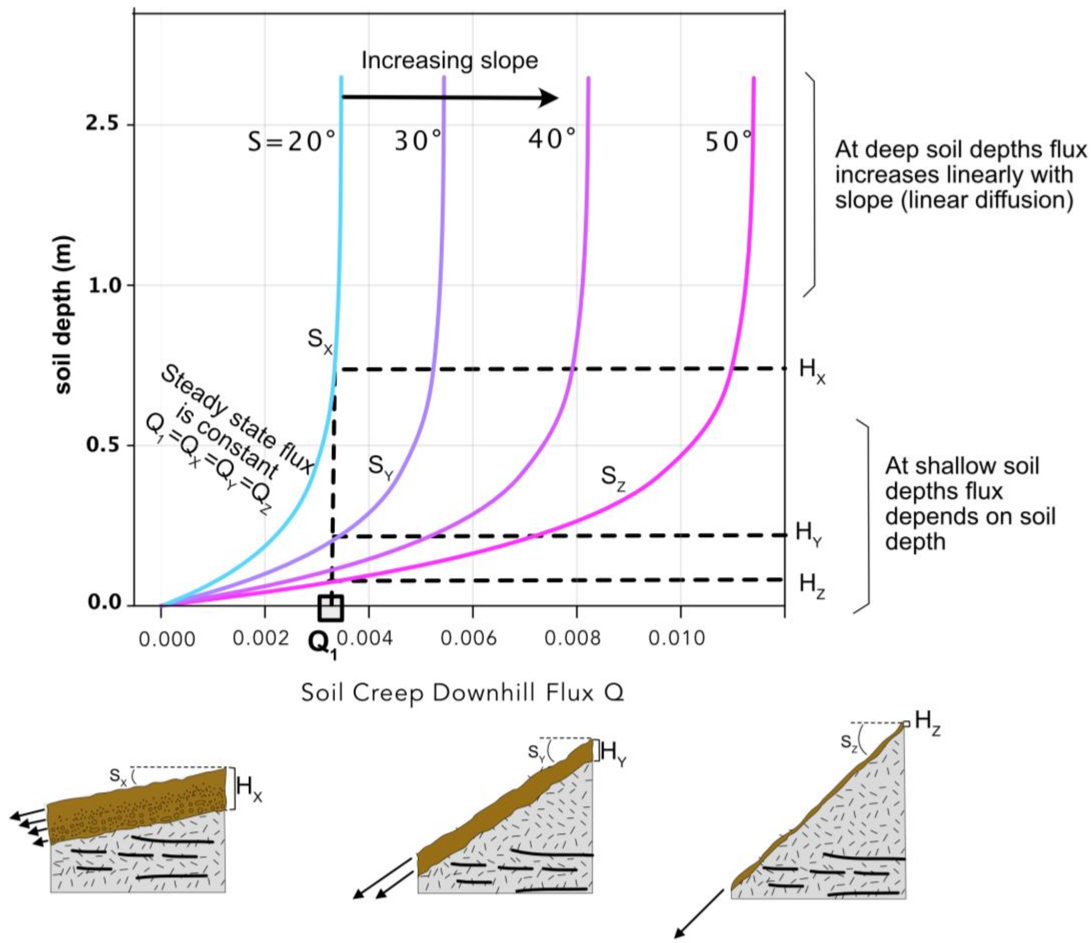

Figure 3.9: Demonstration of soil-depth-driven steepening. We plot the linear diffusion, depth-dependent soil creep function used in our model, demonstrating how total soil flux depends on soil depth and slope. For three models with constant uplift (U_1) and the same hillslope positions, we expect their fluxes to remain constant. However, if these models have different soil depths, perhaps as set by the P_0 values of fig. 3.8, each model requires a different slope to achieve equal fluxes. Models with shallower soil depths achieve the same flux as models with deep soils at steeper slopes.

Soil-Depth dependent landsliding

Within the soil-limited domain, decreasing soil depth correlates with decreasing landslide erosion. Following the infinite slope factor of safety equation (Eq. 3.1), decreasing soil depths increase the factor of safety and reduce slope failures (Fig. 3.7c). For the specific set of strength and hydrologic parameters we imposed for this numerical experiment, soil depths of less than 0.5 m are never unstable even at very steep slopes (Fig. 3.7c).

Thus, as the mean soil depth decreases, fewer cells have unstable FS values regardless of slope angle. This will limit the propagation of landslides, thus limiting landslide areas. If enough cells become stable, then the total number of landslides will also decrease. Increased stability for shallower soils (as predicted by model slopes) has been shown to match shallow landslide observations (Lee et al., 2025), though it may be offset by hydrological inputs not fully explored here.

We observe decreased area of landslides with decreasing soil depths (Fig. 3.3f, 3.7c), which is especially prominent when mean soil depths approach 0.5 m. Though this may in part relate to the drainage density, we posit that this is primarily due to decreased extent of unstable terrain due to low soil depth. Decreasing landslide size at low soil depths matches the observations made by Prancevic et al., (2020).

Landslides are commonly invoked as the primary mechanism that maintains threshold slopes in tectonically active landscapes with high uplift rates (Larsen et al., 2010; Larsen and Montgomery, 2012; Montgomery and Brandon, 2002; Ouimet et al., 2009). Such a mechanism is essential for steady-state landscapes with threshold slopes, where uplift outpaces the maximum weathering rate (below the N_{SD} zero point)(Schlunegger et al., 2013). Deep seated bedrock landsliding is usually invoked to explain the observed slopes in these uplifting landscapes (Heimsath et al., 2012; Ouimet et al., 2009), though, shallow landsliding has also been suggested as a mechanism for keeping rapidly uplifting landscapes at threshold slopes (Larsen et al., 2010). This study reveals that shallow landsliding may be able to keep slopes at constant angles in landscapes that lie in the sweet spot where slopes are high enough for landsliding to occur and soil depths are deep enough for landsliding. However, because soil-landslides are supply limited, they are unable to significantly impact landscapes where uplift outpaces weathering. Instead, bedrock landsliding, or other bedrock erosive processes are required to keep landscapes in steady state if N_{SD} is less than zero.

3.5.2 Comparison with observations in the San Gabriel Mountains

Perhaps the best studied mountain system with respect to measured local erosion and weathering rates is the San Gabriel Mountains (SGM) in Southern California (Dibiase et al., 2012; DiBiase et al., 2010, 2023; Dixon et al., 2012; Heimsath et al., 2012; Neely et al., 2019). Landslide coverage per SGM catchments was compiled by Dibiase et al. (2023) and integrates data from several geologic maps. This SGM landslide dataset is deep seated landslide deposits that likely involve the failure of bedrock rather than just the soil regolith layer. However, these landslides decreased in coverage with increasing exposed bedrock (i.e., low soil thickness), so they may be limited by similar processes that exist for the modeled soil landslides and warrant comparison with our modeled landslide erosion rates (Figure 3.10).

The peak in modeled soil landslide fraction roughly correlates with the slope at which peak landsliding is mapped in the SGM (Fig. 10a), with the onset of higher landslide amounts at ~ 25-30° for both datasets. SGM catchments also show a strong drop off in landslide observations around 40° where the transition to bedrock dominated landscapes is observed (DiBiase et al., 2023). For most model experiments this matches the start of decreased landsliding within the soil limited domain. We note though that many of our model runs have unrealistically steep mean slopes, beyond the strength of what natural landscapes can hold because they have no mechanism to erode unweathered bedrock other than stream power erosion, discussed more in the model limitations section below.

We also estimate N_{SD} values for the SGM catchments by assuming that the catchments are in steady state, so that uplift equals the ^{10}Be erosion rate data (DiBiase et al., 2023). This may be a valid assumption according to agreement between ^{10}Be erosion rates and thermochronologically derived uplift rates, as well as a lack of conspicuous knickpoints (DiBiase et al., 2010; Lavé & Burbank, 2004; Struble et al., 2023). We also assume that the larger P_0 recorded by (Heimsath et al., 2012) is valid for all catchments, though P_0 may vary across catchments.

The modeled peak landslide erosion rate for all Phase 1 models falls mostly in the range at or above the N_{SD}-zero point (Fig. 3.10b), similar to the phase 2 models (Fig. 3.5b). In comparison, the catchment with the greatest landslide coverage in the SGM dataset falls in a similar range, however there is more scatter in the measured data. The onset of landsliding from the slope-limited side (positive N_{SD} values) does roughly match the modeled onset of soil landsliding. Many of the SGM catchments with significant landsliding lie in the range where the ^{10}Be inferred erosion rate outpaces the max P_0 resulting in more negative N_{SD} values. Many of these catchments have mean slopes from 35-40° and are not necessarily exposed bedrock, implying that the SGM landslides are not soil limited, and that the bedrock landslides themselves may act to depress slopes and preserve soil in catchments where U outpaces P_0.

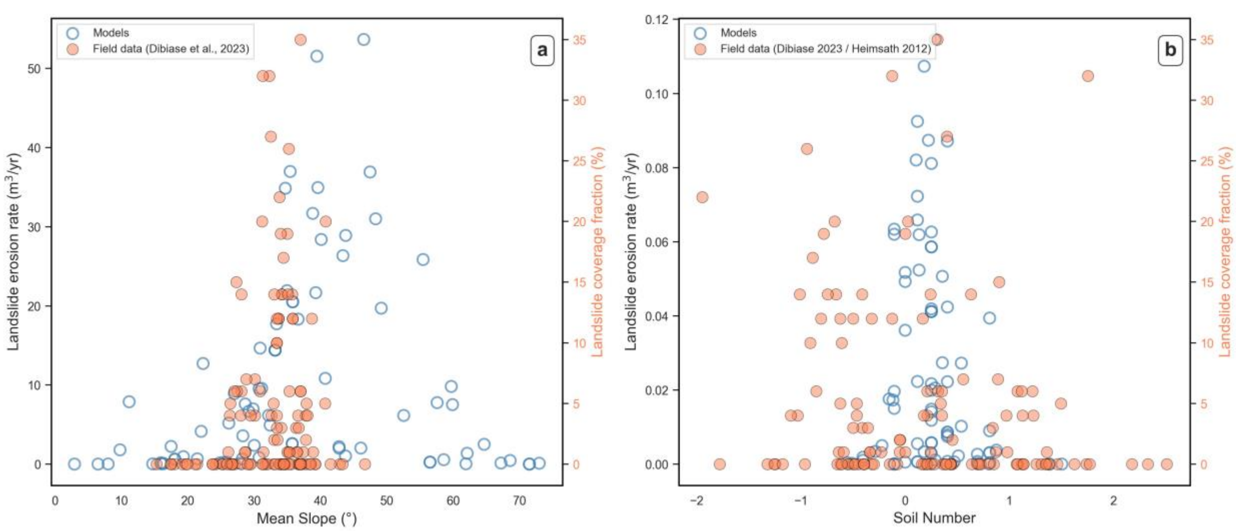

Figure 3.10: A comparison of model results with datasets from the San Gabriel Mountains. (a) shows the landslide erosion rate from the phase 1 models from this study in blue circles and left y axis, and the deep seated landslide coverage fraction for mapped catchments within the SGM, as orange circles and the right y axis. (b) has the same y axis and datasets, but the x axis is now the estimate soil number. SGM data are compiled from Dibiase et al., (2023) and Heimsath et al., (2012).

3.5.3 Model limitations

We built our model experiments to explore the relationships with hillslope processes, soil creep, soil production, and landscape form on soil landsliding, and thus simplified other aspects of the geomorphic system present in natural landscapes. Even within the hillslope geomorphic functions we used, there are several important parameters that were not explored systematically. For example, although we focused on soil depth, we did not vary any of the depth decay scale parameters (H_{DD} and H_{SP}). We suspect that the ratio between the soil creep depth decay scale

(H_{DD}) and the soil production depth decay scale (H_{SP}) may impact the relationship between soil depth and slopes and possibly be instrumental to defining the observed soil-depth slope steepening feedback.

We chose model parameters with hillslope evolution in mind and did not explore fluvial parameters fully. We set the fluvial advection and bedrock erosion parameters to minimize the impact of sediment on fluvial erosion, allowing sediment to be transported and eroded easily. Feedback mechanisms between slope, soil depth, and soil production directly impact the channels, especially by setting sediment cover and grain size. If we instead used a range of realistic parameters for sediment cover and transport, we expect that over-steepened slopes in our experiments might not reach steady state. We also suspect that the removal of weathered sediment allowed for bedrock erosion of very steep slopes even at very low drainage areas.

Steep headwater channels with drainage areas approaching the limits of our domain channels are often influenced by debris flow erosion, which likely dominates in the San Gabriel mountains (Struble et al., 2023) and many landscapes where soil landslides may be observed (Kobor and Roering, 2004). Soil landslides are often the impetus of debris flows which may act to erode landscapes (Keck et al., 2024), while the soil landslide runout process in our models is exclusively depositional. We did not model debris flow erosion in this study.

Perhaps most importantly, processes that may erode exposed bedrock on hillslopes are absent. The body of research on the San Gabriel Mountains details a transition between soil mantled landscapes and landscapes with exposed bedrock (DiBiase et al., 2023; Heimsath et al., 2012; Neely et al., 2019; Neely and DiBiase, 2020). Our models also suggest this transition, where soil depth decreases such that soil mantled processes of soil landsliding and soil creep can no longer be the primary drivers of hillslope erosion. Our experiments do not include functions to define the bedrock side of this transition. Bedrock was input into the model domain via uplift and was either weathered to soil and eroded via soil creep or soil landsliding or converted to sediment by fluvial bedrock incision. Rockfall, colluvial erosion, dry ravel processes, and bedrock landslides are absent. As is any description of bedrock fracturing, which was shown to exert a first order control on bedrock landscape slopes and sediment transport (Neely and DiBiase, 2020). This study highlights the need for future research, quantifying how bedrock landscapes erode.

To simulate bedrock landscapes it may be necessary for landscape evolution models to incorporate discrete transport event-based processes, like rockfall. Classically, hillslope evolution models have relied on continuum equations for long term sediment flux that are derived from landscape form (Tucker et al., 2018), though recent advances have started to form mechanistic connection between the event scale and long term flux scale (Campforts et al., 2020; Gabet and Mudd, 2010; Glade et al., 2017; Tucker et al., 2018) and references there in). In fact, our study demonstrates the power of combining simulations of discrete mechanistic events with continuum functions.

3.6 Conclusions

In this study we explore the relationship between soil landsliding, diffusivity, fluvial erosion, soil production, and uplift. We do this through three-dimensional landscape evolution models that reveal what sets soil landslide susceptibility and how different geomorphic processes contribute to steady state landscapes where soil landslide erosion is persistent over millions of years.

Our model results reveal two domains with different controls on soil landslide erosion: a slope-limited domain and a soil-limited domain. In the slope-limited domain, simulated landscapes are defined by relatively gentle slopes, and thick soil layers. The amount of landslide erosion is limited by the lack of steep slopes where landslides can initiate. In the soil-limited domain, landscapes are defined by steep slopes and minimal to no hillslope soil cover. These landscapes are steep enough to have landsliding failure, however they produce small landslide areas, and the low soil depth values also act to stabilize the slopes and limit soil supply which can be moved by landsliding.

We quantify these two domains via two dimensionless parameters: N_{SLP} which quantifies the relationship between uplift and erosion from both hillslope diffusion and fluvial erosion and does a generally good job at predicting the onset of landsliding at low slopes, and N_{SD} which is related to the prediction for steady state soil thickness derived from an exponential soil production function and is set by log of the ratio between uplift and erosion. When uplift equals the maximum weathering rate, $N_{SD}=0$, a soil depth inflection point is reached, defining the transition point between the slope-limited and soil-limited landsliding domains. In our models, the peak soil erosion rates occur where the maximum weathering rate is equal to or slightly exceeds the uplift rate ($N_{SD} >0$ but not $N_{SD}>>0$) and the amplitude of the soil landslide erosion is set by the N_{SLP} at the transition.

This study highlights the first-order importance of soil depth in governing the processes driving the evolution of soil mantled landscapes. Soil depth modulates our current best estimate geomorphic transport functions defining soil creep, soil production, and soil landsliding. Still, relatively few datasets define these functions, demonstrating a need for further studies quantifying these parameters, specifically: soil production maximum rates, soil production decay depths, depth-dependent diffusion decay depths, and the depth-dependent diffusive soil creep functional form.

We also find soil-depth-driven steepening, an important soil depth related feedback observed in the models. This phenomenon occurs where the diffusivity is effectively decreased at low soil depths, according to a depth-dependent diffusion function, resulting in increased slopes to maintain a steady flux and steady state landscape. This relationship is yet to be fully quantified for natural landscapes, though it may be an important feedback leading to increased bedrock exposures and steep cliffs where soil production rates are low.

The models also demonstrate the transition from soil mantled landscapes to bedrock landscapes as defined by the N_{SD}. We lament the non-existence of LEM functions to describe the full suite of processes operating on bedrock hillslopes, a poorly quantified gap in our understanding of landscape form and evolution.

Our models underscore the significant role that soil landsliding can play in the hillslope erosional budget, lowering slopes under some circumstances. However, we suggest that soil landsliding alone cannot maintain threshold hillslopes where soil production is outpaced by uplift. Similar to what has been discovered about diffusive soil creep, where uplift outpaces soil production, soil landslides are supply limited.

3.7 Supplementary tables for Chapter 3

Table S3.1 Phase 1 model parameters

Experiment	Run	Soil Transport Velocity	Soil Production Max Rate	K_br	Uplift Rate
77	1	0.03	0.0002	5.00E-06	0.00035
77	2	0.03	0.0004	5.00E-06	0.00035
77	3	0.03	0.00045	5.00E-06	0.00035
77	4	0.03	0.0005	5.00E-06	0.00035
77	5	0.03	0.0006	5.00E-06	0.00035
78	1	0.01	0.00045	5.00E-06	0.00035
78	2	0.02	0.00045	5.00E-06	0.00035
78	3	0.03	0.00045	5.00E-06	0.00035
78	4	0.05	0.00045	5.00E-06	0.00035
78	5	0.075	0.00045	5.00E-06	0.00035
79	1	0.03	0.00045	5.00E-07	0.00035
79	2	0.03	0.00045	1.00E-06	0.00035
79	3	0.03	0.00045	5.00E-06	0.00035
79	4	0.03	0.00045	1.00E-05	0.00035
79	5	0.03	0.00045	5.00E-05	0.00035
80	1	0.02	0.00045	1.00E-06	0.0001
80	2	0.02	0.00045	1.00E-06	0.0002
80	3	0.02	0.00045	1.00E-06	0.0003
80	4	0.02	0.00045	1.00E-06	0.0004
80	5	0.02	0.00045	1.00E-06	0.0005
83	1	0.02	0.00045	5.00E-06	0.0002
83	2	0.02	0.00045	5.00E-06	0.0003
83	3	0.02	0.00045	5.00E-06	0.00035
83	4	0.02	0.00045	5.00E-06	0.0004
83	5	0.02	0.00045	5.00E-06	0.0005
84	1	0.02	0.00045	5.00E-06	0.0002
84	2	0.02	0.00045	5.00E-06	0.0003
84	3	0.02	0.00045	5.00E-06	0.00035
84	4	0.02	0.00045	5.00E-06	0.0004
84	5	0.02	0.00045	5.00E-06	0.0005
85	1	0.075	0.00045	1.00E-05	0.0002
85	2	0.075	0.00045	1.00E-05	0.0003
85	3	0.075	0.00045	1.00E-05	0.00035
85	4	0.075	0.00045	1.00E-05	0.0004
85	5	0.075	0.00045	1.00E-05	0.0005
86	1	0.02	0.00045	1.00E-05	0.0002
86	2	0.02	0.00045	1.00E-05	0.0003
86	3	0.02	0.00045	1.00E-05	0.00035

86	4	0.02	0.00045	1.00E-05	0.0004
86	5	0.02	0.00045	1.00E-05	0.0005
87	1	0.02	0.00045	1.00E-06	0.0002
87	2	0.02	0.00045	1.00E-06	0.0003
87	3	0.02	0.00045	1.00E-06	0.00035
87	4	0.02	0.00045	1.00E-06	0.0004
87	5	0.02	0.00045	1.00E-06	0.0005
88	1	0.075	0.00045	1.00E-06	0.0002
88	2	0.075	0.00045	1.00E-06	0.0003
88	3	0.075	0.00045	1.00E-06	0.00035
88	4	0.075	0.00045	1.00E-06	0.0004
88	5	0.075	0.00045	1.00E-06	0.0005
89	1	0.03	0.0002	5.00E-06	5.00E-05
89	2	0.03	0.0002	5.00E-06	0.0001
89	3	0.03	0.0002	5.00E-06	0.00015
89	4	0.03	0.0002	5.00E-06	0.0002
89	5	0.03	0.0002	5.00E-06	0.0003
92	1	0.02	0.0003	5.00E-06	0.00025
92	2	0.02	0.0003	5.00E-06	0.0003
92	3	0.02	0.0003	5.00E-06	0.00035
92	4	0.02	0.0003	5.00E-06	0.0004
92	5	0.02	0.0003	5.00E-06	0.00045
92	6	0.02	0.0003	5.00E-06	0.0005
93	1	0.02	0.0004	5.00E-06	0.00025
93	2	0.02	0.0004	5.00E-06	0.0003
93	3	0.02	0.0004	5.00E-06	0.00035
93	4	0.02	0.0004	5.00E-06	0.0004
93	5	0.02	0.0004	5.00E-06	0.00045
93	6	0.02	0.0004	5.00E-06	0.0005
94	1	0.02	0.0005	5.00E-06	0.00025
94	2	0.02	0.0005	5.00E-06	0.0003
94	3	0.02	0.0005	5.00E-06	0.00035
94	4	0.02	0.0005	5.00E-06	0.0004
94	5	0.02	0.0005	5.00E-06	0.00045
94	6	0.02	0.0005	5.00E-06	0.0005
95	1	0.02	0.0006	5.00E-06	0.00025
95	2	0.02	0.0006	5.00E-06	0.0003
95	3	0.02	0.0006	5.00E-06	0.00035
95	4	0.02	0.0006	5.00E-06	0.0004
95	5	0.02	0.0006	5.00E-06	0.00045
95	6	0.02	0.0006	5.00E-06	0.0005

Table S3.2. Phase 2 model parameters

Experiment	Run	Soil Transport Velocity	Soil Production Max Rate	K_br	Uplift Rate
100	1	0.02	0.00025	5.00E-06	0.00035
100	2	0.02	0.0003	5.00E-06	0.00035
100	3	0.02	0.00035	5.00E-06	0.00035
100	4	0.02	0.0004	5.00E-06	0.00035
100	5	0.02	0.00045	5.00E-06	0.00035
100	6	0.02	0.0005	5.00E-06	0.00035
101	1	0.02	0.00025	5.00E-06	0.00025
101	2	0.02	0.0003	5.00E-06	0.00025
101	3	0.02	0.00035	5.00E-06	0.00025
101	4	0.02	0.0004	5.00E-06	0.00025
101	5	0.02	0.00045	5.00E-06	0.00025
101	6	0.02	0.0005	5.00E-06	0.00025
101	7	0.02	0.0002	5.00E-06	0.00025
101	8	0.02	0.00015	5.00E-06	0.00025
102	1	0.02	0.00025	5.00E-06	0.00045
102	2	0.02	0.0003	5.00E-06	0.00045
102	3	0.02	0.00035	5.00E-06	0.00045
102	4	0.02	0.0004	5.00E-06	0.00045
102	5	0.02	0.00045	5.00E-06	0.00045
102	6	0.02	0.0005	5.00E-06	0.00045
102	7	0.02	0.00055	5.00E-06	0.00045
102	8	0.02	0.0006	5.00E-06	0.00045
102	9	0.02	0.0007	5.00E-06	0.00045
102	10	0.02	0.0008	5.00E-06	0.00045
102	11	0.02	0.001	5.00E-06	0.00045
102	12	0.02	0.0015	5.00E-06	0.00045
97	1	0.02	0.0002857	5.00E-06	0.00025
97	2	0.02	0.0003429	5.00E-06	0.0003
97	3	0.02	0.0004	5.00E-06	0.00035
97	4	0.02	0.0004571	5.00E-06	0.0004
97	5	0.02	0.0005143	5.00E-06	0.00045
97	6	0.02	0.0005714	5.00E-06	0.0005
98	1	0.02	0.0004	5.00E-06	0.00025
98	2	0.02	0.00048	5.00E-06	0.0003
98	3	0.02	0.00056	5.00E-06	0.00035
98	4	0.02	0.00064	5.00E-06	0.0004
98	5	0.02	0.00072	5.00E-06	0.00045
98	6	0.02	0.0008	5.00E-06	0.0005
99	1	0.02	0.0002222	5.00E-06	0.00025
99	2	0.02	0.0002666	5.00E-06	0.0003
99	3	0.02	0.0003111	5.00E-06	0.00035

99	4	0.02	0.0003555	5.00E-06	0.0004
99	5	0.02	0.0004	5.00E-06	0.00045
99	6	0.02	0.0004444	5.00E-06	0.0005

3.8 References

Barnhart, K. R., Glade, R. C., Shobe, C. M., and Tucker, G. E.: Terrainbento 1.0: A Python package for multi-model analysis in long-term drainage basin evolution, Geosci. Model Dev., 12, 1267–1297, https://doi.org/10.5194/gmd-12-1267-2019, 2019.

Barnhart, K. R., Hutton, E. W. H., Tucker, G. E., M. Gasparini, N., Istanbulluoglu, E., E. J. Hobley, D., J. Lyons, N., Mouchene, M., Siddhartha Nudurupati, S., M. Adams, J., and Bandaragoda, C.: Short communication: Landlab v2.0: A software package for Earth surface dynamics, Earth Surf. Dyn., 8, 379–397, https://doi.org/10.5194/esurf-8-379-2020, 2020.

Bellugi, D., Milledge, D. G., Dietrich, W. E., Perron, J. T., and McKean, J.: Predicting shallow landslide size and location across a natural landscape: Application of a spectral clustering search algorithm, J. Geophys. Res. Earth Surf., 120, 2552–2585, https://doi.org/10.1002/2015JF003520, 2015.

Broeckx, J., Rossi, M., Lijnen, K., Campforts, B., Poesen, J., and Vanmaercke, M.: Landslide mobilization rates: A global analysis and model, Earth-Science Rev., 201, 102972, https://doi.org/10.1016/j.earscirev.2019.102972, 2020.

Brosens, L., Campforts, B., Robinet, J., and Vanacker, V.: Slope Gradient Controls Soil Thickness and Chemical Weathering in Subtropical Brazil : Understanding Rates and Timescales of Regional Soilscape Evolution Through a Combination of Field Data and Modeling Journal of Geophysical Research : Earth Surface, 1–26, https://doi.org/10.1029/2019JF005321, 2020.

Campforts, B., M. Shobe, C., Steer, P., Vanmaercke, M., Lague, D., and Braun, J.: HyLands 1.0: A hybrid landscape evolution model to simulate the impact of landslides and landslide-derived sediment on landscape evolution, Geosci. Model Dev., 13, 3863–3886, https://doi.org/10.5194/gmd-13-3863-2020, 2020.

Campforts, B., Shobe, C. M., Overeem, I., and Tucker, G. E.: The Art of Landslides: How Stochastic Mass Wasting Shapes Topography and Influences Landscape Dynamics, J. Geophys. Res. Earth Surf., 127, 1–22, https://doi.org/10.1029/2022jf006745, 2022.

Crozier, M. J.: Landslide geomorphology: An argument for recognition, with examples from New Zealand, Geomorphology, 120, 3–15, https://doi.org/10.1016/j.geomorph.2009.09.010, 2010.

Dibiase, R. A., Heimsath, A. M., and Whipple, K. X.: Hillslope response to tectonic forcing in threshold landscapes, Earth Surf. Process. Landforms, 37, 855–865, https://doi.org/10.1002/esp.3205, 2012.

DiBiase, R. A., Whipple, K. X., Heimsath, A. M., and Ouimet, W. B.: Landscape form and millennial erosion rates in the San Gabriel Mountains, CA, Earth Planet. Sci. Lett., 289, 134–144, https://doi.org/10.1016/j.epsl.2009.10.036, 2010.

DiBiase, R. A., Neely, A. B., Whipple, K. X., Heimsath, A. M., and Niemi, N. A.: Hillslope Morphology Drives Variability of Detrital 10Be Erosion Rates in Steep Landscapes, Geophys. Res. Lett., 50, 1–10, https://doi.org/10.1029/2023GL104392, 2023.
Dietrich, W. E., Bellugi, D. G., Sklar, L. S., Stock, J. D., and Roering, J. J.: Geomorphic Transport Laws for Predicting Landscape Form and Dynamics, 1–30, 2003.
Dixon, J. L., Hartshorn, A. S., Heimsath, A. M., DiBiase, R. A., and Whipple, K. X.: Chemical weathering response to tectonic forcing: A soils perspective from the San Gabriel Mountains, California, Earth Planet. Sci. Lett., 323–324, 40–49, https://doi.org/10.1016/j.epsl.2012.01.010, 2012.
Duvall, A. R. and Tucker, G. E.: Journal of Geophysical Research : Earth Surface Dynamic Ridges and Valleys in a Strike-Slip Environment, 2016–2026, https://doi.org/10.1002/2015JF003618.Received, 2016.
Emberson, R., Kirschbaum, D. B., Amatya, P., Tanyas, H., and Marc, O.: Insights from the topographic characteristics of a large global catalog of rainfall-induced landslide event inventories, 1129–1149, 2022.
Godard, V., Ollivier, V., Bellier, O., Miramont, C., Shabanian, E., Fleury, J., Benedetti, L., and Guillou, V.: Weathering-limited hillslope evolution in carbonate landscapes, Earth Planet. Sci. Lett., 446, 10–20, https://doi.org/10.1016/j.epsl.2016.04.017, 2016.
Heimsath, A. M., Dietrich, W. E., Nishiizumi, K., and Finkel, R. C.: Stochastic processes of soil production and transport: Erosion rates, topographic variation and cosmogenic nuclides in the Oregon coast range, Earth Surf. Process. Landforms, 26, 531–552, https://doi.org/10.1002/esp.209, 2001.
Heimsath, A. M., Furbish, D. J., and Dietrich, W. E.: The illusion of diffusion: Field evidence for depth-dependent sediment transport, Geology, 33, 949–952, https://doi.org/10.1130/G21868.1, 2005.
Heimsath, A. M., DiBiase, R. A., and Whipple, K. X.: Soil production limits and the transition to bedrock-dominated landscapes, Nat. Geosci., 5, 210–214, https://doi.org/10.1038/ngeo1380, 2012.
Hovius, N., Stark, C. P., and Allen, P. A.: Sediment flux from a mountain belt derived by landslide mapping, Geology, 25, 231–234, https://doi.org/10.1130/0091-7613(1997)025<0231:SFFAMB>2.3.CO;2, 1997.
Johnstone, S. A. and Hilley, G. E.: Lithologic control on the form of soil-mantled hillslopes, Geology, 43, 83–86, https://doi.org/10.1130/G36052.1, 2015.
Keck, J., Istanbulluoglu, E., Campforts, B., Tucker, G., and Horner-devine, A.: A landslide runout model for sediment transport , landscape evolution , and hazard assessment applications, 1165–1191, https://doi.org/10.5194/esurf-12-1165-2024, 2024.
Larsen, I. J. and Montgomery, D. R.: Landslide erosion coupled to tectonics and river incision, Nat. Geosci., 5, 468–473, https://doi.org/10.1038/ngeo1479, 2012.
Larsen, I. J., Montgomery, D. R., and Korup, O.: Landslide erosion controlled by hillslope material, Nat. Geosci., 3, 247–251, https://doi.org/10.1038/ngeo776, 2010.
Lee, S., Kang, T., Kim, M., Ko, H., and An, H.: Progress in Disaster Science Evaluation of spatiotemporal effects of soil depth on shallow landslides and debris flows via coupled numerical analysis, Prog. Disaster Sci., 28, 100470, https://doi.org/10.1016/j.pdisas.2025.100470, 2025.
Litwin, D. G., Malatesta, L. C., and Sklar, L. S.: Hillslope diffusion and channel steepness in landscape evolution models, Earth Surf. Dyn., 13, 277–293, https://doi.org/10.5194/esurf-13-277-2025, 2025.
Neely, A. B. and DiBiase, R. A.: Drainage Area, Bedrock Fracture Spacing, and Weathering Controls on Landscape-Scale Patterns in Surface Sediment Grain Size, J. Geophys. Res. Earth Surf., 125, 1–22, https://doi.org/10.1029/2020JF005560, 2020.
Neely, A. B., DiBiase, R. A., Corbett, L. B., Bierman, P. R., and Caffee, M. W.: Bedrock fracture density controls on hillslope erodibility in steep, rocky landscapes with patchy soil cover, southern California, USA, Earth Planet. Sci. Lett., 522, 186–197, https://doi.org/10.1016/j.epsl.2019.06.011, 2019.
Patton, N. R., Lohse, K. A., Godsey, S. E., Crosby, B. T., and Seyfried, M. S.: Predicting soil thickness on soil mantled hillslopes, Nat. Commun., 9, https://doi.org/10.1038/s41467-018-05743-y, 2018.
Pedrazas, M. A., Hahm, W. J., Huang, M. H., Dralle, D., Nelson, M. D., Breunig, R. E., Fauria, K. E., Bryk, A. B., Dietrich, W. E., and Rempe, D. M.: The Relationship Between Topography, Bedrock Weathering, and Water Storage Across a Sequence of Ridges and Valleys, J. Geophys. Res. Earth Surf., 126, 1–25, https://doi.org/10.1029/2020JF005848, 2021.

Perron, J. T., Dietrich, W. E., and Kirchner, J. W.: Controls on the spacing of first-order valleys, 113, 1–21, https://doi.org/10.1029/2007JF000977, 2008.
Phillips, J. D.: Weathering instability and landscape evolution, Geomorphology, 67, 255–272, https://doi.org/10.1016/j.geomorph.2004.06.012, 2005.
Prancevic, J. P., Lamb, M. P., McArdell, B. W., Rickli, C., and Kirchner, J. W.: Decreasing Landslide Erosion on Steeper Slopes in Soil-Mantled Landscapes, Geophys. Res. Lett., 47, 1–9, https://doi.org/10.1029/2020GL087505, 2020.
Roering, J. J., Kirchner, J. W., and Dietrich, W. E.: Evidence for nonlinear, diffusive sediment transport on hillslopes and implications for landscape morphology, Water Resour. Res., 35, 853–870, https://doi.org/10.1029/1998WR900090, 1999.
De Rose, R. C.: Slope control on the frequency distribution of shallow landslides and associated soil properties , North Island , New Zealand, 371, 356–371, https://doi.org/10.1002/esp.3283, 2013.
Schlunegger, F., Norton, K., and Caduff, R.: Hillslope Processes in Temperate Environments, Treatise Geomorphol., Volume 7, 337–354, https://doi.org/10.1016/B978-0-12-374739-6.00183-4, 2013.
Schuster, R. L. and Highland, L. M.: Socioeconomic and Environmental Impacts of Landslides in the Western Hemisphere, 2001.
Shobe, C. M., Tucker, G. E., and Barnhart, K. R.: The SPACE 1.0 model: A Landlab component for 2-D calculation of sediment transport, bedrock erosion, and landscape evolution, Geosci. Model Dev., 10, 4577–4604, https://doi.org/10.5194/gmd-10-4577-2017, 2017.
Theodoratos, N., Seybold, H., and Kirchner, J. W.: Scaling and similarity of a stream-power incision and linear diffusion landscape evolution model, 779–808, 2018.
Tucker, G. E. and Hancock, G. R.: Modelling landscape evolution, Earth Surf. Process. Landforms, 35, 28–50, https://doi.org/10.1002/esp.1952, 2010.
Tucker, G. E., Mccoy, S. W., and Hobley, D. E. J.: A lattice grain model of hillslope evolution, 563–582, 2018.
Wang, Y., Willett, S. D., and Wu, D.: The Role of Weathering on Morphology and Rates of Escarpment Retreat of the Rift Margin of Madagascar Journal of Geophysical Research : Earth Surface, 1–17, https://doi.org/10.1029/2022JF007001, 2023.
West, N., Kirby, E., Bierman, P., and Clarke, B. A.: Aspect-dependent variations in regolith creep revealed by meteoric 10 Be, 1–4, https://doi.org/10.1130/G35357.1, 2014.

4. CONCLUSIONS

In this dissertation, I investigated landslide legacies through two distinct research domains. I developed a hazard assessment for landslide dam formation by bringing together landscape analysis, landslide inventories, and statistical relationships to identify rivers prone to landslide dam formation. I also developed a simplified but physically based model for shallow landslides and implemented it within landscape evolution simulations lasting millions of years. By mapping a smaller subset of damming landslides, analyzing the statistics of a large (>19,000) dataset of mapped landslides, and writing the code to simulate millions of landslides, I have developed a holistic understanding of their nature and impacts. In this conclusion, I'll go over the next steps that I think should be taken in both research domains, highlight the tools I developed during my PhD, and finish with some unifying takeaway lessons.

4.1 Future work

4.1.1 Landslide dam hazards

As this study introduced a new method, the damability function, there remains plenty of work to do to expand and refine landslide dam susceptibility analysis. I think that the damability function framework can be used to expand landslide dam susceptibility analysis nationwide, and perhaps even globally, but this would require future studies.

The first aspect to test is the applicability of the damability function form to other landslide dam datasets. Researchers should answer if this functional form and framework can work in other landscapes and attempt to answer how damability function fits vary from region to region. Regional variations in valley morphology, rock types, and landslide triggers may impact how landslides runout across rivers and change the form of the damability function.

To expand the damability analysis globally, one would need to update both the valley width and landslide volume estimations to work in data-poor locations. The valley width measuring algorithm works well with high resolution DEMs down to resolutions as coarse as 10 m, however this prevents future applications from areas where high resolution DEMs are not available. Also, large landslide inventories are uncommon. I devoted significant effort to the development of proxy relationships for landslide volume within the Oregon Coast Range, using the SLIDO landslide inventory as an empirical base. These multi-regressions were unsuccessful, illustrating that one cannot predict size of a future landslide on a hillslope in the OCR given only measurable landscape attributes. But I believe that there remains a useful proxy for landslide sizes relevant to landslide dams. Such a proxy would be required for a damability analysis in a location without a large landslide inventory.

Future researchers should consider what is needed to turn the damability function from a research paper to a usable product. The first step should be to define what a usable product looks like with the help of the eventual end users who could be state geologic agencies, state hazard managers, state transportation agencies, county emergency managers, or any of the other people involved in hazard mitigation preparation and response. Natural applications include: widespread damability maps and event response damability map generation, but the stakeholder community knows best what information they need and should be consulted in the development of any future products or maps.

Our hazard susceptibility maps do not include the actual primary hazard: the outburst flood. Results within the OCR clarified significantly when I added in an analysis of possible dammed lake volumes and compared these volumes to historic events. I believe that further studies should combine analysis of possible dam locations (identified with the damability model), with the possible extent of outburst floods from those locations. This may require developing a simplified relationship between floodwater heights and distances from landslide dams that can then be integrated across a damability map.

Lastly, I think this study reveals the limitations of a hazard analysis project that does not venture into risk analysis and the "human" aspect. I identified several rivers within the Oregon Coast Range where large landslide dammed lakes could form, but without a sense of population or infrastructure exposure to possible outburst floods, it is difficult to assess where preparation related to this hazard is most important. I'm convinced that the most useful hazard map related to landslide dam hazards must include some representation of the infrastructure and riverfront populations downstream of possible dams.

4.1.2 Landslides in landscape evolution models

With the introduction of the SoilLandslider component to the modular Landlab open-source landscape evolution modelling community, I'm excited to see how various researchers will engage with it. Natural research directions to explore with a soil landsliding module include: the influence of climate change on landsliding, the impact of landsliding on channel evolution, and the interplay between fire regimes, shallow landslides and disparate recovery timescales. One future direction I am already exploring is the impact of earthquake-triggered landslides on landscapes.

Within the model domain, I think further exploration is warranted to clarify the feedback between landslide sediment and fluvial sediment cover, and to explore the importance of each depth-dependent decay scale characteristic depth.

I identified two important relationships between soil depth and landscape processes that should be further explored in natural landscapes. Specific study locales should be selected as natural experiments to test: 1. the relationship between the soil production function and soil depths, and 2. soil-depth-driven steepening.

My dissertation revealed the importance of the transition between supply-limited soil mantled hillslope and transport-limited bedrock hillslope regimes. I established that soil landslides are limited to soil-mantled hillslopes. Currently, the only Landlab component for hillslope evolution that is applicable to bedrock hillslopes is BedrockLandslider (Campforts et al., 2020), which simulates Cullman wedge landsliding. While bedrock landsliding may be the primary erosive agent on these slopes, it also neglects other processes like rockfall and colluvium transport. While easier said than done, I identify a need for a mechanistic understanding, and/or geomorphic transport function to represent the set of processes that erode hillslopes in bedrock landscapes.

4.2 Tools developed

Over the course of my PhD, I developed multiple tools which can continue to assist the geomorphology and natural hazard scientific communities. Below, I highlight three of those tools.

1. The damability function workflow is an improvement on earlier research (Tacconi Stefanelli et al., 2020), but is built on a probabilistic framework that makes it especially adaptable to new datasets developed by future researchers. As landslide dam hazard researchers continue to investigate this hazard, I think the damability function workflow will continue to evolve and support susceptibility estimates.

2. I developed an algorithm for measuring valley widths. Existing techniques were either too difficult to access, unreliable, or not repeatable within coding environments. I created the ElevationThresholdValleyWidth algorithm within the topotoolbox analytical ecosystem. This code has the right balance of simplicity, complexity, and interpretability to be chosen by researchers who want to measure valley width. This code has already been applied across the world by other researchers, from deep sea submarine channels to Himalayan rivers.

3. The SoilLandslider module is already the subject of Chapter 2, so it needs little further mention here, other than to reiterate that it is built for the open-source modular Landlab ecosystem. In Chapter 2, I also systematically highlighted how the modules of this ecosystem work together in order to support future users as they set up their own landscape evolution models.

4.3 Final lessons

- Landslide dams pose a rare but serious threat to lives and infrastructure, but in the past, most serious hazards have been mitigated by coordinated responses by government agencies, and there's no reason to believe that won't be the case in the future. This hope is especially warranted if the natural hazard community continues pre-event assessment and preparations.

- For landslide dams, the hazard is widespread, so the key factor is risk. Our results reveal that almost any mountain river could be dammed by a landslide, but few are large enough to create serious floods and it remains unclear how many people this hazard impacts.

Future research should focus on assessing where people are living close enough downstream from large and dammable rivers to be in harm's way.

- Not all landslides are created equal; shallow landslides are fundamentally different from deep seated landslides. I suspect that the inclusion of both landslide types is our training dataset is one reason we were unable to predict landslide sizes within the OCR. When it comes to landscape evolution, our models reveal that shallow soil landslides are analogous to fast hillslope diffusion and are limited by soil production supply (just like soil creep). In contrast, bedrock landslides fail bedrock or soil and are not limited by soil production, and capable of setting landscape form where soil landslides are not. Landslide inventories and analysis should clearly demarcate what type of landslide they have observed (fortunately, many already do).

- Soil depth is as important as slope for soil-mantled landscape evolution. Any study of hillslope processes in soil mantled landscapes should pay close attention to the soil depth, and what processes are governing it.

- Landslide recurrence time matters, and at a long enough timescale, all landslides are supply limited. In general, continuous processes can transport landslide sediment over decadal to centennial timescales, while landslide recurrence is on the order of thousands to tens of thousands of years for soil and bedrock landslides (Campforts et al., 2022). Thus, the recurrence timescale is the rate limiting factor, which is likely greater than the recurrence interval of the trigger. So, if one is considering landslides in the context of landscape evolution they should not only consider the lifespan of the eroded sediment and the frequency of the trigger, but also how long it will take for the source location to re-steepen or infill enough soil to fail in a landslide again.

5. ACKNOWLEDGEMENTS

Modern science is not a solitary activity and this research was only accomplished thanks to the support of a fantastic group of people.

First and foremost, I'd like to thank my advisor, Alison Duvall. She always made the time to discuss science, push me towards a more comprehensive understanding of our study landscapes, and to support me as a scientist and a person. Her enthusiasm and curiosity are infectious and only surpassed by the care she shows for the students she mentors. Alison also acquired significant funding for this position.

I would like to thank my full committee, Juliet Crider, Dave Montgomery, and alex grant for their guidance and scientific contributions, with special acknowledgment to the reading committee for reviewing this work. Dave Montgomery contributed significantly to the development of a more realistic soil landslide model. alex grant provided especially useful comments for the whole draft, and significantly contributed to Chapter 1.

Research accomplished with the financial support of: The National Science Foundation Graduate Research Fellowship to P.M.M. under Grant No. DGE-1650441, The National Science Foundation's Cascadia Coastlines and Peoples (CoPes) research hub (grant no. ICER-2103713) to Duvall, The Cowan Field Fund, and the OpenEarthscape, CSDMS (Community Surface Dynamics Modeling System) Summer visiting scholar program.

I am thankful for the two research communities I was able to be a part of outside of my university. The Copes Hub helped me understand natural hazards in a much more comprehensive way beyond my research area. CSDMS, and the researchers that are a part of it, taught me that great research emerges when the research community is prioritized.

I'm grateful for the vibrant Earth and Space Sciences department at UW. The greater "Supergroup" community who showed by example how to foster a friendly and rigorous scientific discussion. I'm thankful for our Geoscapes research group, which has always discussed geomorphology loud and at length! I'd like to specifically acknowledge my lab-mate Tamara Aranguiz-Rago who coached my presentations and contributed scientifically to the research. Lastly, graduate school is a social endevor and I'm grateful to have been a member of the UW ESS super cohort of 2020 & 2021 grad student admits, and the best office ever JHN 423 ("The Bike Shop").

I will be eternally grateful to my wife, Paula Bürgi, who supported me through this process. She also showed me how it's done by getting a PhD first, and greatly contributed to every aspect of this research, from brainstorming, to critiquing, to proofreading, and listening to me practice any presentation.